

**PRINTED ANTENNA ELEMENTS
WITH ATTESTED
ULTRA WIDE BAND ARRAY APPLICABILITY**

**PRINTED ANTENNA ELEMENTS
WITH ATTESTED
ULTRA WIDE BAND ARRAY APPLICABILITY**

PROEFSCHRIFT

ter verkrijging van de graad van doctor
aan de Technische Universiteit Delft,
op gezag van de Rector Magnificus Prof. ir. K. C. A. M. Luyben,
voorzitter van het College voor Promoties,
in het openbaar te verdedigen op 01 februari 2009 om 10.00 uur

door

Fatma Müge TANYER-TİĞREK

Electrical and Electronics Engineer (Master of Science) in
Middle East Technical University, Ankara, Turkey
geboren te Konya, Turkije

Dit proefschrift is goedgekeurd door de promotor:
Prof.dr.ir. L.P. Ligthart

copromotor:
Dr. ing. I.E. Lager

Samenstelling promotiecommissie:

Rector Magnificus,	voorzitter
Prof. dr. ir. L. P. Ligthart,	Technische Universiteit Delft, promotor
Dr. ing. I. E. Lager,	Technische Universiteit Delft, copromotor
Prof. ir. P. van Genderen,	Technische Universiteit Delft
Prof. dr. A. Hızal,	Middle East Technical University
Prof. dr. C. Craeye,	Université Catholique de Louvain
Prof. F. Le Chevalier,	Technische Universiteit Delft
Dr ir. G. H. C. van Werkhoven,	Thales Nederland BV
Prof. dr. J. R. Long,	Technische Universiteit Delft, reserve lid

Printed Antenna Elements with Attested UWB Array Applicability
Fatma Müge Tanyer-Tiğrek.

Thesis Delft University of Technology.
With references and with summary in Dutch.

ISBN 978-90-9024664-2

Subject headings: ultra wide-band antenna, printed antenna, linear arrays,
antenna array mutual coupling, antenna measurements.

Printed in The Netherlands

Copyright © 2009 by F. M. Tanyer-Tiğrek

All rights reserved. No part of the material protected by this copyright notice may be reproduced or utilized in any form or by any means, electronic or mechanical, including photocopying, recording or by any information storage and retrieval system, without permission from the copyright owner.

The work presented in this thesis was financially supported by the Netherlands Technology Foundation (STW) and (semi-) governmental and industrial organizations in the Netherlands.

To My Family

Contents

1	Introduction	1
1.1	Problem definition and limitations in the research	3
1.2	Objectives and main research question	4
1.3	Proposed methodology	5
1.4	Novelties and main results	5
1.5	Outline of the thesis	6
1.6	General conventions employed throughout the thesis	8
2	Fundamentals of antennas and arrays	9
2.1	Antenna history and short literature survey	9
2.2	Antenna elements and arrays	11
2.2.1	Array bandwidth	12
2.2.2	Requirements for UWB antennas	13
2.2.3	Approaches to achieve antennas/arrays operating over a wide bandwidth	14
2.2.4	Limitations in achieving wide-band antennas	15
3	Design of UWB elements with no ground plane	19
3.1	Choice for type of radiator	19
3.2	“Eared” antenna	20
3.2.1	Design procedure	21

3.2.2	Determination of the basic dimensions of the original antenna	22
3.2.3	Optimization of the antenna	26
3.2.4	Validation of the optimization process	29
3.2.5	Further optimization of the antenna	37
3.2.6	Validation of the final optimization	38
3.3	Operating principles and investigation of UWB characteristics	39
3.3.1	Summary of the antenna operating principles	42
3.3.2	Traveling wave characteristic and their impact on the UWB performance	42
3.4	“Tulip” loop antenna	46
3.4.1	Antenna design	47
3.4.2	Modified loop antenna	50
3.5	Conclusions	59
4	Design of an Artificial Magnetic Conductor	61
4.1	High impedance electromagnetic surfaces– standard approach	61
4.1.1	Theoretical background	63
4.1.2	Design procedure	65
4.1.3	Integration of the “Tulip” loop antenna and standard AMC structures	67
4.2	Non-standard, a-periodic AMC structure	70
4.2.1	Integration of the “Tulip” loop antenna and non-standard AMC structures	70
4.2.2	The effect of extending the size of a-periodic AMC structures	72
4.3	Conclusions	74
5	Integration of the designed radiators in UWB array environments	77
5.1	Linear array consisting of “Tulip” loop elements	78
5.1.1	Array architecture optimization	78

5.1.2	Array performance assessment	85
5.2	Linear arrays consisting of “Eared” elements	90
5.2.1	Analysis of the linear array containing 7 elements . . .	92
5.2.2	Analysis of the linear array containing 15 elements . .	99
5.3	Conclusions	112
6	Suitability of antenna elements to Impulse Radio applica- tions	115
6.1	Readily available solutions to full IR UWB band coverage . .	115
6.2	IR UWB antenna design	116
6.2.1	Design philosophy	116
6.2.2	Determination of the antenna dimensions	119
6.3	Frequency domain validation	123
6.3.1	Scattering parameter measurements	123
6.3.2	Radiation pattern measurements	123
6.4	Time-domain validation	130
6.4.1	System setup	130
6.4.2	Investigation of the group delay	130
6.4.3	Investigation of the fidelity factor	131
6.5	Conclusions	134
7	Conclusions	137
7.1	General conclusions and discussions	137
7.2	Elements of novelty	140
7.3	Future research	141
A	Work embedding in IRCTR antenna research	145
B	(Quasi-) magnetic antennas	147
C	Time-domain de-embedding techniques	149

D	Array reflection coefficient synthesis	151
E	Coplanar waveguide structures	155
E.1	Conventional coplanar waveguides	155
E.2	Coplanar waveguides on a finite thickness dielectric substrate	158
	Bibliography	161
	List of Abbreviations	171
	Summary	173
	Samenvatting	175
	Acknowledgments	177
	About the author	179
	Author's Publications	181

List of Figures

3.1	Configuration of the proposed CPW-fed, quasi-magnetic antenna.	21
3.2	Fabricated “Eared” antenna – initial variant, with and without the pertaining SMA connector.	24
3.3	Simulation and measurement results concerning the original antenna.	24
3.4	Effect of soldering (a) “Eared” antenna, with a SMA connector with long pin and short pin; (b) Simulation and measurement results concerning the original antenna.	25
3.5	Current distribution on the surface of the “Eared” antenna at 9 GHz.	27
3.6	Frequency dependence of the return loss for different values of the transition length L_T	28
3.7	Optimized “Eared” antenna, with and without the pertaining SMA connector.	29
3.8	Optimized “Eared” antenna with longer feed section, with and without the pertaining SMA connector.	29
3.9	Simulation and measurement results concerning the optimized “Eared” antenna.	30
3.10	Antenna under test while measuring the $\phi = 90^\circ$ plane.	31
3.11	Measured radiation patterns at $\phi = 0^\circ$ cut(a) 5.6 GHz; (b) 10.5 GHz; (c) 15 GHz: thick line – co-polar component; thin line – cross-polar component.	32

3.12	Measured radiation patterns at $\phi = 90^\circ$ cut(a) 5.6 GHz; (b) 10.5 GHz; (c) 15 GHz: thick line – co-polar component; thin line – cross-polar component.	33
3.13	Measured radiation patterns at $\theta = 85^\circ$ cut(a) 5.6 GHz; (b) 10.5 GHz; (c) 15 GHz: thick line – co-polar component; thin line – cross-polar component.	34
3.14	Antenna with/without absorber on its feed section	35
3.15	Comparison between the normalized radiation patterns (in decibels) corresponding to the $\{\phi = 0^\circ; \phi = 180^\circ\}$ cut, (a) 5.6 GHz; (b) 10.5 GHz; (c) 15 GHz: thick line – co-polar component, without the absorber shield; thin line – co-polar component, with the absorber shield.	36
3.16	Frequency dependence of the return loss for different values of W_T , the upper tapering length of the transition region.	37
3.17	Frequency dependence of the return loss for different values of L_{R2} , the resonator length of the radiating region.	38
3.18	Final version of the optimized “Eared” antenna, with and without the pertaining SMA connector.	39
3.19	Final-optimized “Eared” antenna with longer feed section, with and without the pertaining SMA connector.	39
3.20	Simulation and measurement results concerning the final optimized “Eared” antenna. Measurements were clipped at 31 GHz which is taken as the upper limit for the bandwidth of the employed SMA connector.	40
3.21	Normalized measured radiation patterns (in decibels) at 11 GHz: thick line – co-polar component; thin line – cross polar component. (a) $\{\phi = 0^\circ; \phi = 180^\circ\}$ cut; (b) $\{\phi = 90^\circ; \phi = 270^\circ\}$ cut; (c) $\theta = 85^\circ$ cut.	41
3.22	Current distribution in the CPW-fed, quasi magnetic antenna at 37.3 GHz, with sections of the antenna labeled.	43
3.23	H-field distribution (at different phases) at 9.5 GHz.	44
3.24	H-field distribution (at different phases) at 20.8 GHz.	44
3.25	H-field distribution (at different phases) at 29 GHz.	45
3.26	H-field distribution (at different phases) at 37.3 GHz.	45
3.27	“Tulip” loop antenna.	47

3.28	Return loss variation with respect to (a) Length of the tuning stub (l); (b) Length of the gap (w_c).	49
3.29	Surface current distribution of the loop antenna at 8.5 GHz.	50
3.30	Fabricated loop antenna. Left- the photo- etched microwave laminate; right- antenna with the attached SMA connector.	51
3.31	Simulated and measured return loss concerning the “Tulip” loop antenna.	51
3.32	Fabricated modified loop antenna.	52
3.33	Simulated and measured return loss concerning the modified loop antenna.	52
3.34	Modified “Tulip” loop antenna under test (a) Exposed; (b) Covered with absorbers.	54
3.35	Normalized measured radiation patterns (in decibels) at 8.5 GHz: thick line – co-polar component; thin line – cross polar component. (a) $\{\phi = 0^\circ; \phi = 180^\circ\}$ cut; (b) $\{\phi = 90^\circ; \phi = 270^\circ\}$ cut; (c) $\theta = 85^\circ$ cut.	55
3.36	Normalized measured radiation patterns (in decibels) at 12 GHz: thick line – co-polar component; thin line – cross polar component. (a) $\{\phi = 0^\circ; \phi = 180^\circ\}$ cut; (b) $\{\phi = 90^\circ; \phi = 270^\circ\}$ cut; (c) $\theta = 85^\circ$ cut.	56
3.37	Comparison between the normalized radiation patterns (in decibels) at 8 GHz corresponding to the (a) $\{\phi = 0^\circ; \phi = 180^\circ\}$ cut; (b) $\{\phi = 90^\circ; \phi = 270^\circ\}$ cut; (c) $\theta = 85^\circ$ cuts, for 8 GHz: thick line – co-polar component, without the absorber shield; thin line – co-polar component, with the absorber shield.	58
4.1	High impedance surface. (a) Side view; (b) top view [81].	64
4.2	4 by 4 Artificial Magnetic Conductor.	66
4.3	The phase of the reflected field from the AMC surface depicted in Fig. 4.2.	66
4.4	The “Tulip” loop antenna on a 4×4 AMC structure.	67
4.5	Simulated return loss concerning the “Tulip” loop antenna and AMC plane.	68

4.6	Radiation patterns for the “Tulip” loop antenna plus the AMC structure at the $\phi = 90^\circ$ cut at (a) 8 GHz, (b) 10 GHz: thick line – co-polar component; thin line – cross polar component.	69
4.7	Radiation patterns at the $\phi = 0^\circ$ cut at (a) 8 GHz, (b) 10 GHz: thick line – co-polar component; thin line – cross polar component.	69
4.8	Configuration of the antenna together with the a-periodic AMC structure and coordinate system.	70
4.9	Simulated return loss concerning the antenna and the a-periodic AMC plane.	71
4.10	Modified normalized radiation patterns at the $\phi = 90^\circ$ cut at (a)8 GHz, (b)10 GHz: (for a-periodic AMC surface): thick line – co-polar component; thin line – cross polar component.	72
4.11	Modified normalized radiation patterns at the $\phi = 0^\circ$ cut at (a)8 GHz, (b)10 GHz: thick line – co-polar component; thin line – cross polar component.	72
4.12	Simulated return loss concerning the “Tulip” loop antenna and AMC plane on a large ground plane.	73
4.13	Modified normalized radiation patterns on a larger ground plane at the $\phi = 0^\circ$ cut at (a) 8 GHz, (b) 10 GHz: thick line – co-polar component; thin line – cross polar component.	73
4.14	Final normalized radiation patterns on a larger ground plane at the $\phi = 90^\circ$ cut at (a)8 GHz, (b)10 GHz: (for a-periodic AMC surface): thick line – co-polar component; thin line – cross polar component.	74
5.1	Linear array of four “Tulip” loop antennas with coordinate system.	78
5.2	Return loss of the “Tulip” array, depicted in Fig. 5.1, from the first and second ports of the array with all other elements are loaded with matched loads.	79
5.3	The coupling levels for the “Tulip” array.	80
5.4	Linear array of slotted “Tulip” antenna.	81
5.5	Return loss of the slotted “Tulip” array antenna.	81
5.6	The coupling levels of the slotted “Tulip” array antenna.	82

5.7	Return loss from the first port of the array depicted in Fig. 5.4, while the other ports are matched, versus slot length dependence.	82
5.8	Return loss from the second port of the array depicted in Fig. 5.4, while the other ports are matched, versus slot length dependence.	83
5.9	“Tulip” loop antenna, geometry, parameters and coordinate system.	83
5.10	Fabricated linear array of CPW fed, printed, loop antennas and coordinate system.	84
5.11	Simulated and measured return loss concerning the loop array antenna of Fig. 5.10 (a) $S_{11}(= S_{44})$; (b) $S_{22}(= S_{33})$	86
5.12	Frequency and scanning angle dependence of the array return loss for the simulated scattering matrix. Note that $ S_{11} $ stands in these plots for the array return loss.	87
5.13	Frequency and scanning angle dependence of the array return loss for the measured scattering matrix. Note that $ S_{11} $ stands in these plots for the array return loss.	87
5.14	Frequency dependence of the array return loss for the power divider fed array. Comparison with the synthesized data concerning the simulated and measured scattering matrix.	89
5.15	Normalized simulated and measured radiation patterns at (a) 8.5 GHz; (b) 12 GHz.	91
5.16	Normalized radiation patterns corresponding to the $\{\phi = 0^\circ; \phi = 180^\circ\}$ cut, at 9 GHz. Thick line – measurement with power divider feeding; thin line – separate measurement of each antenna and MATLAB summing up.	92
5.17	Configuration of the linear array consisting of 7 “Eared” antennas and the coordinate system.	93
5.18	Photo of the linear array consisting of 7 “Eared” antennas.	93
5.19	Simulated reflection coefficient magnitude for the linear array of Fig. 5.17: (a) magnitude; (b) phase.	95
5.20	Magnitude and phase difference of S_{35} and S_{46} concerning the linear array of Fig. 5.17.	96

5.21	Active reflection coefficients, for $\vartheta_0 = 30^\circ$, concerning the linear array of Fig. 5.17: (a) S_{11} and S_{22} ; (b) S_{33} and S_{44}	97
5.22	Frequency dependence of the reflection coefficient magnitude for different values of scanning angles; as derived from the measured data for the linear array of Fig. 5.18. Note that $ S_{11} $ stands in these plots for the array return loss.	98
5.23	Simulated and calculated array return loss concerning the “Eared” antenna array of Figs. 5.17 and 5.18.	99
5.24	Normalized simulated and measured radiation patterns of the linear array composed of 7 elements (Figs. 5.17 and 5.18) at (a) 8 GHz; (b) 10 GHz.	100
5.25	Photo of linear array of 15 CPW fed “Eared” antennas.	101
5.26	Calculated active reflection coefficients concerning the linear array of Fig. 5.25.	102
5.27	Reflection coefficient measurement set-up of the linear array of 15 CPW fed “Eared” antennas.	102
5.28	Frequency dependence of the reflection coefficient magnitude for different values of scanning angles; (a) assembled from the approximated data; (b) assembled from the measured data. Note that $ S_{11} $ stands in these plots for the array return loss.	104
5.29	Radiation pattern measurement of the linear array of 15 CPW fed “Eared” antennas.	105
5.30	Radiation pattern measurement of the linear array of 15 CPW fed “Eared” antennas.	106
5.31	Normalized radiation patterns (in decibels) corresponding to the $\{\phi = 0^\circ; \phi = 180^\circ\}$ cut, for 3 characteristic frequencies ((a) at 8 GHz (b) at 10 GHz and (c) at 12 GHz) : thick line – co-polar component; thin line – cross polar component.	107
5.32	Measured element radiation patterns at the $\phi = 0^\circ$ cut and 12 GHz frequency for: (a) first array element; (b) second array element; (c) seventh array element.	110
5.33	Measured radiation patterns at $\phi = 0^\circ$ cut and 12 GHz frequency for: (a) $\vartheta_0 = 30^\circ$; (b) $\vartheta_0 = 51.8^\circ$; (c) $\vartheta_0 = 65^\circ$	111
5.34	Scan loss curve of the array at 12 GHz.	112

6.1	Configuration of the proposed CPW-fed, quasi-magnetic antenna.	117
6.2	Frequency dependence of the return loss for “antenna 1” and “antenna 2”.	117
6.3	Frequency dependence of the return loss for different values of the transition length L_T	120
6.4	Frequency dependence of the return loss for different values of W_T , the upper tapering length of the transition region. . .	120
6.5	Frequency dependence of the return loss for different values of L_{R2} , the resonator length of the radiating region.	121
6.6	Frequency dependence of the return loss for “antenna 3” and “antenna 4”.	122
6.7	The IR UWB “Eared” antenna, with and without the pertaining SMA connector.	123
6.8	Simulation and measurement results concerning the final optimized IR UWB “Eared” antenna.	125
6.9	Measured radiation patterns concerning the final optimized IR UWB “Eared” antenna at the $\phi = 0^\circ$ cut(a) 3.5 GHz; (b) 6 GHz; (c) 9.5 GHz: thick line – co-polar component; thin line – cross-polar component.	126
6.10	Measured radiation patterns concerning the final optimized IR UWB “Eared” antenna at the $\phi = 90^\circ$ cut(a) 3.5 GHz; (b) 6 GHz; (c) 9.5 GHz: thick line – co-polar component; thin line – cross-polar component.	127
6.11	Measured radiation patterns concerning the final optimized IR UWB “Eared” antenna at the $\theta = 85^\circ$ cut(a) 3.5 GHz; (b) 6 GHz; (c) 9.5 GHz: thick line – co-polar component; thin line – cross-polar component.	128
6.12	Measured radiation patterns concerning the final optimized IR UWB “Eared” antenna at 15 GHz for the (a) $\phi = 0^\circ$ cut; (b) $\phi = 90^\circ$ cut; (c) $\theta = 85^\circ$ cut: thick line – co-polar component; thin line – cross-polar component.	129
6.13	Measured phase concerning the transfer function of the UWB “Eared” antenna.	131
6.14	Measured group delay concerning the UWB “Eared” antenna.	132

6.15	Antenna input signal, $s_t(t)$ in (a) time domain; (b) frequency domain.	133
6.16	Antenna output signal, $s_r(t)$ in time domain.	134
B.1	Top view of (a) a (quasi-) magnetic antenna ; (b) an electric antenna	148
D.1	Illustrative for the evaluation of the array reflection coefficient.	152
E.1	Front view of a CPW, sandwiched between two dielectric substrates, with top and bottom shielding	156
E.2	Front view of a CPW on a finite thickness dielectric substrate	158

List of Tables

3.1	Geometric parameters of the proposed “Eared” antenna. . . .	23
3.2	Geometric parameters of the “Tulip” loop antenna.	48
6.1	Initial geometric parameters of the IR UWB “Eared” antenna.	118
6.2	Geometric parameters of the IR UWB “Eared” antenna. . . .	124

LIST OF TABLES

Chapter 1

Introduction

Ultra wide-band (UWB) technology has experienced many significant developments in recent years. In 2002, the Federal Communications Commission (FCC) of the United States adopted the First Report and Order that permitted the commercial operation of UWB technology [31] and also allocated a bandwidth of 7.5 GHz, i.e. from 3.1GHz to 10.6 GHz for UWB applications. The FCC also protects existing users operating within this spectrum by limiting the UWB signal transmitting power. UWB devices' power spectral density levels should be limited to -41.3 dBm/MHz or 75nW/MHz. Since then, UWB technology has been regarded as one of the most promising high data rate technologies. However, there are still challenges in making this technology live up to its full potential. One particular challenge concerns the research on and development of UWB antennas which have become a topic of continued investigations in the fields of wireless communications and radar applications due to such attractive features as transmitting and/or receiving electromagnetic energy in shorter duration and avoiding both frequency and space dispersion.

The short duration pulses used in UWB technology offer several advantages. First of all, the power restriction in the UWB band enables UWB to coexist with current radio services with minimal interference as the UWB systems reside below the noise floor of a typical narrow-band receiver. The second advantage is the improved channel capacity. The maximum data rate or capacity for the ideal band limited, additive white Gaussian noise channel is related to the bandwidth and signal-to-noise ratio (SNR) by Shannon-Nyquist criterion through the following equation [74]:

$$C = B \log_2(1 + SNR) \quad (1.1)$$

where C denotes the maximum transmit rate and B is the channel bandwidth.

Equation (1.1) shows that the channel capacity can be increased either by increasing SNR and/or B . The maximum data rate can be enhanced more rapidly by increasing the occupied bandwidth than by increasing the SNR. Since UWB pulses have large bandwidth, the maximum data that can be transmitted per second over a communication channel can be high. However, due to the current power limitation of FCC on UWB transmissions, such data rate is available for only short ranges. This makes UWB systems perfect candidates for short-range, high data rate wireless applications such as wireless personal area networks (WPANs)[71]. A further advantage of UWB communication systems is their inherent immunity for detection and interception due to their low average transmission power. Besides, UWB technology for positioning enhances the range resolutions when utilizing the extremely large bandwidths. Finally, UWB systems based on impulse radio (IR) feature low cost and low complexity because some components such as local oscillators, mixers, filters and band-limited amplifiers are not needed.

Impulse Radio is the way of transmitting Ultra Wide Band (UWB) signals without a carrier. The concept of impulse radio initially originated by Marconi in the beginning of the 1900's when the spark gap transmitters induced pulsed signals having very wide bandwidths [84]. Very narrow time-domain pulses were used with duration in the order of nanoseconds. These short pulses are radiated by an impulse generator and antenna. If the UWB transmission is carrierless, meaning that the data is not modulated on a continuous waveform with a specific carrier frequency, such carrierless transmission requires fewer RF components than carrier-based transmission [71]. This makes the transceiver architecture simpler compared to the narrow-band transceivers, meaning that they can be manufactured in small sizes at a lower cost than narrow-band systems.

Antennas used in IR-UWB applications should satisfy certain specifications. First of all, as discussed above, they should transmit short pulses. The antenna should cover a typically large bandwidth in order to keep the ringing effects on the transmitted pulse on an acceptable level. Secondly, the input impedance of the antennas should be well matched to the transmitter and receiver in order to radiate and receive the power efficiently. Ideally, the radiation pattern and the impedance matching should be stable across the entire band. Finally, in order to ensure the usefulness of the antenna for time-domain applications, its time-domain responses should be appropriate. It should be preferably non-dispersive, and the antenna should have a fixed phase center. The antenna should have constant and small group delays

(typically on the order of nanoseconds) in order to transmit the signal (information) with less distortion. If the antenna has a linear phase curve, its group delay is constant and low.

As discussed, using UWB technologies has many advantages and there exists a wide variety of applications in military, civilian and commercial sectors. Thus there are application-specific requirements that the antennas should satisfy, apart from the general UWB requirements. For example, base station functionalities can be considered in UWB communications. The main service for base stations is voice communication and data transfer. Since there can be users all around the base station, bi-directional antennas can be applied into the base station as transmit antennas. Base stations are required which follow the users, thus a scanning capability of the antenna is also required. All these properties require the design of UWB antenna elements that have omnidirectional radiation patterns. As it is also a necessity to have low-cost and reproducible antennas, printed and low-profile designs are recommendable for this specific application. Since, as in the “base station example”, scanning performance of the array is important, it is also needed to embed the antenna elements in array configurations and to provide a certain scanning capability to the array without generating any grating lobes in the visible space.

Small and inexpensive UWB transceivers are good candidates for wireless sensor network applications. UWB systems can thus also be used in inventory control and asset management. In these applications, the wider the antenna bandwidth, the higher the resolution. The omnidirectional, low profile antennas carrying low powers can therefore also be used in applications as asset management.

In this thesis, low-profile UWB antennas that can be used in the applications above will be investigated. The results reported in this thesis have been achieved within the frame of the Wide Band Sparse Element Array Antennas (WiSE) project (See Appendix A).

1.1 Problem definition and limitations in the research

Currently, there is a manifest trend towards developing low-profile, low-cost and small sized antennas which are suitable for wide-band scanning array applications. Understandably, the development of small-sized antenna elements which cover large spectra are strategic points of interest. The combination of the wide-band requirement and the desire to ensure a small

size for the relevant antennas result in an extremely challenging problem. The performances of such UWB radiators in array environments are also an important and demanding issue. Most of the time, as will be explained in detail in Chapter 2, the antenna element bandwidth drops dramatically when it is embedded in an array environment, as the array bandwidth is primarily determined by element size rather than by element bandwidth. A wide-band element is often physically larger than the wavelength at the highest frequency, meaning that the full bandwidth of the element can not be used because of scan angle limitations at the high end of the frequency band of the isolated element. In the design of wide-band arrays the space between the array elements is an inherent problem. It is desirable to have a small inter-element spacing but this spacing is limited by the antenna element size. Furthermore, in the array environment the mutual coupling between the elements should be limited, as explained in Chapter 5, as it affects detrimentally the antenna performances in terms of scan blindness, side lobe levels, etc. Thus, apart from the size of the element, mutual coupling also determines how closely two adjacent elements should be placed.

Since this research has been effectuated within the frame of the WISE project (Appendix A), the initial design focuses on X-band, covering the frequency range from 8 GHz to 12 GHz. After having some satisfactory results in this band the design is scaled to the UWB band ranging from 3.1 to 10.6 GHz. In this way the design can be used for applications discussed in the first part of the Introduction.

1.2 Objectives and main research question

After having defined the general problem, the main research objectives can now be formulated explicitly:

- fundamental investigation of a number of elementary radiators that are amenable to be used in array environments, such as the ones employed in UWB communication systems, the emphasis being with low profile UWB antennas that have broadside radiation;
- set-up of a novel antenna approach to designing, manufacturing and testing UWB elementary radiators, at this point it is stressed that, in view of ensuring an easy and accurately replicable manufacturing, the research will be confined to antennas that are fabricated in printed, lithographic technology;

- investigation of the performance of single radiators in linear array environments, both theoretically and practically;
- mitigation of mutual coupling in linear array environments;
- feasibility of adding a ground plane to be used in conjunction with investigated elementary radiators.

These objectives are summarized in the main research question:

How can we design optimal UWB elements for array environments?

1.3 Proposed methodology

In this dissertation, the problem which was defined in Section 1.1 is solved by introducing a (quasi-) magnetic type of antennas (See Appendix B for the relevant definitions). Coplanar Waveguide (CPW) lines are used for feeding the antennas allowing for wider impedance bandwidths in excess of 180%. Once the (quasi-) magnetic antennas have been developed, their radiation patterns and reflection characteristics are measured in order to verify their performance. After having satisfactory elementary results, the next step is the investigation of the antennas' performance in a linear array environment. The mitigation of the mutual coupling is achieved (inherently) at element level by having the principal electric field lines in a relatively confined area for the first developed antenna (the "Eared" Antenna). However, for the second antenna (the "Tulip" antenna), this mitigation has been achieved by changing the topology of this antenna and by inserting slots on the antenna surface.

1.4 Novelties and main results

The principal novelties presented in this thesis are listed as follows:

- A systematic way of designing an UWB antenna resulting into a relative bandwidth of more than 180% is discussed. To the author's knowledge this antenna has the widest impedance bandwidth compared to other printed and low-profile antennas discussed in the literature (Chapter 3).

This new antenna, called “Eared” antenna, has inherently low mutual coupling interactions with the neighboring elements in the array environments due to the integrated feeding line design and the confined electric field lines around the transition region of the antenna.

- A systematic way of designing a printed loop antenna, called “Tulip” loop antenna, which has an impedance bandwidth of 68% is presented. To the author’s knowledge this antenna has the smallest electrical size for the mentioned impedance bandwidth compared to the other printed and low-profile radiators described in literature (Chapter 3).
- An artificial ground plane for the novel “Tulip” antenna is successfully developed and the radiation pattern of the antenna is modified into a uni-directional one (Chapter 4).
- The UWB “Eared” antenna is successfully integrated in linear array environments; it is proven that these elements are adequate for being used in linear array (Chapter 5).

A method is developed in order to predict the performance of large arrays from simulations and measurements of smaller arrays. It is shown that the performance is well predicted without doing lengthy simulations.

- The UWB “Tulip” loop antenna is successfully integrated in a linear array environment and the elements are successfully modified such that low mutual coupling with the neighboring elements could be obtained (Chapter 5).
- The “Eared” antenna is re-designed such that it covers at least the UWB frequency band stretching from 3.1 GHz to 10.6 GHz. The antenna demonstrates a total impedance bandwidth of 180% (Chapter 6).

1.5 Outline of the thesis

The thesis is organized as follows:

Chapter 1 gives an introduction to the thesis. The problem definition, the research objectives, the proposed methodology in the thesis and the novelties, together with the main results, are stated.

In Chapter 2, the quick literature survey, fundamental background information on antennas, arrays and concepts related to bandwidth and quality factor are summarized.

Subsequently, Chapter 3 is devoted to the design of UWB elements without ground plane. Firstly the “Eared” antenna is introduced. All systematic ways of designing the antenna, related simulations, experiments, measurements and their evaluation are discussed. The operation principles of the developed antennas are addressed, based on the investigation of the antenna performance and characteristics. Then the “Tulip” loop antenna is investigated in a similar manner.

Chapter 4 deals with the design of an artificial magnetic conductor (AMC) for the single UWB element (Tulip loop antenna). The aim of this chapter is to convert the omnidirectional radiation pattern of a single element into a uni-directional one. All design aspects, simulations and measurements related to this AMC are presented in this chapter.

Afterwards, the integration of the elementary radiators in linear array environments is investigated in Chapter 5. Both the “Eared” antenna and the “Tulip” loop antenna are included in a linear array environment and their array performances are explored.

Chapter 6 discusses the suitability of X-band radiators for Impulse Radio applications. Afterwards the “Eared” antenna will be redesigned such that it covers the UWB frequency range extending from 3.1 GHz to 10.6 GHz.

Chapter 7 is devoted to the conclusions of the research that has been carried out in this thesis and supplemented with recommendations for future research.

The material in this thesis is complemented with information that is instrumental for understanding the presented topics. In order to increase the readability of the account, this information was functionally collected in appendixes, as hereafter enumerated. Firstly, the work embedding in IRCTR antenna research is presented in Appendix A. Subsequently, the electric and magnetic antenna concepts are defined in Appendix B. Then, in Appendix C the time-domain de-embedding techniques which are used in the reflection coefficient measurement of the antennas will be discussed very briefly. A new method for calculating the array reflection coefficient is presented in Appendix D. Finally, the feeding structures which have been used in the antennas within the scope of this thesis are discussed in Appendix E.

1.6 General conventions employed throughout the thesis

All examined configurations in this thesis are considered with respect to a Cartesian reference frame $Oxyz$, the plane xOy coinciding with the antenna surface. The unit vectors $\{\mathbf{i}_x, \mathbf{i}_y, \mathbf{i}_z\}$, in this order, constitute a right-handed system.

A polar reference frame $Or\theta\phi$ is employed for accounting for the electromagnetic field quantities in the far-field region. Following the usual conventions [6], the angle θ measures the tilting with respect to the Oz axis and ϕ measures the rotation around the Oz -axis (with the Ox -axis being taken as reference). The triplet $\{\mathbf{i}_\phi, \mathbf{i}_\theta, \mathbf{i}_r\}$ forms a right-handed system.

Chapter 2

Fundamentals of antennas and arrays

In recent years wide-band antenna research focuses on the design of UWB antennas and antenna arrays. The strongly increased use of radio waves for telecommunications and radar has lead to new requirements on antenna systems: a large bandwidth in conjunction with a small size of antenna elements. The wireless wide-band communications need wide-band antennas to support more users and to provide more information with higher data rates. A major objective of this dissertation is the fundamental investigation of a range of wide-band elementary radiators that are amenable to be included in array environments and that can be used in UWB communication systems. This chapter will provide a brief survey on antenna history, together with a short summary related to topics in this thesis, supplemented with fundamental information about antennas and arrays, such as the bandwidth and the quality factor of an antenna.

2.1 Antenna history and short literature survey

According to the IEEE (Institute of Electrical and Electronics Engineers) standard an antenna is defined as “the part of a transmitting or receiving system which is designed to radiate or to receive the electromagnetic waves” [5]. This means the antenna is an electromagnetic transducer which is used to convert the free space waves to guided waves in the receiving mode and conversely to convert the guided waves to free space waves in the transmitting mode.

The antennas have acquired a large significance starting in the 19th century. James Clerk Maxwell and Heinrich Rudolph Hertz are the ones who defined the electromagnetic field theory and showed the first electromagnetic systems. Historically, wire antennas are the ones which were first developed. In the beginning of the 20th century, Guglielmo Marconi studied such antennas. The antenna studies began therefore with a concentration on this antenna type.

The working principles of wire antennas such as dipoles can be found extensively in literature ([6, Chapter 4], [28], [55, Chapter 6],[100]). Dipole antennas are simple antennas for use in a wide variety of practical applications. Finding the electric and the magnetic fields radiated by the wire antennas is the ultimate technique to analyse them. The radiated field of the dipole antenna can be calculated by using the electric currents flowing on the wire. These kind of electric antennas tend to have relatively large near-fields that are prone to undesired coupling with nearby objects. However many commercial applications need antennas that are less prone to near-field coupling [79]. Magnetic loop antennas can be considered as ideal candidates for these applications and can be considered from a duality perspective when compared to the electric dipole antenna. It means that there exists an E and H duality between the electric dipole element and the magnetic loop antenna. Three general types of magnetic antennas, namely large current radiators, monoloops and slot antennas are discussed in [79].

Subsequently, aperture antennas like waveguide apertures, reflectors, lenses and horns received extra attention after the 1st World War because of the increasing demand for more complex antennas and the utilization of high frequencies. Aperture antennas have been used in communications, radar and remote sensing applications for many years. Extensive information about reflector antennas can be found in [6, Chapter 12], [15], [29, Chapter 2], [40], [55, Chapter 10]. Reflector antenna analysis and synthesis hinges around the evaluation of the integral for the field radiated by a surface distribution of sources [77]. Horn antennas can be considered as flared-out waveguides which are investigated in detail in [6, Chapter 13], [9], [55, Chapter 9].

Array antennas and printed antennas have become important after the World War 2. For the last 40 to 50 years, the focus has been on the development of printed antennas. Microstrip printed antennas received an extensive attention due to advantages such as low profile, light weight, low cost and small size. However, conventional microstrip antennas are narrow-band and measures for substantially increasing their operational bandwidth were needed; examples of antennas with increased bandwidth are the stacked

structures and those with parasitic patches. Detailed information about arrays and printed antennas can be found in [7], [33], [38], [56] and [70].

After the adoption of the First Report and Order by the Federal Communication Commission, that permitted the commercial operation of UWB technology, UWB research and development has evolved very fast from theoretical study to engineering design as well as from general concepts to specific prototypes [13]. Looking through the history of UWB antennas, it can be noticed that before 1990's all proposed UWB antennas were based on general volumetric structures, such as Schelkunoff's spheroidal antenna (1941), Lodge's & Carter's biconical antenna (1898, 1939), Lindenblad's coaxial horn element (1941), Brillouin's omnidirectional and directional coaxial horn antenna (1948), King's conical horn antenna (1942), Katzin's rectangular horn antenna (1946), Stohr's ellipsoidal monopole and dipole antenna (1968) and Harmuth's large current radiator (1985). As explained previously, from 1992 onwards, several microstrip, slot and planar monopole antennas with simple structures such as circular, elliptical or trapezoidal shapes have been proposed. Today the state of the art of UWB antennas focuses on these microstrip, slot and planar monopole antennas with different matching techniques [72]. In this dissertation, the research is directed towards planar UWB antennas that are also suitable for array environments. In the following section the basic concepts concerning the antenna elements will be reviewed.

2.2 Antenna elements and arrays

An antenna element that is to be used in array environments should have various properties such as small size and broad patterns. From these properties, the physical size of the element is most important since the scanning performance of an array is generally determined by the element spacing which, in turn, is limited by the element size. The performance of wide-band arrays degrades towards the high end of the frequency band where the distance between the antenna elements becomes electrically large. If wide scan angles are required, the inter-element spacing of the antenna elements should be small, which automatically puts a limitation on the size of the element. Ideally, if large scanning angles are desired, the element spacing should be smaller than $\lambda/2$ at the upper end of the frequency spectrum, where λ is the free space wavelength. Otherwise the inter-element spacing can be electrically too large to scan the full volume ($\pm 90^\circ$) towards the upper end of the frequency band due to the onset of the grating lobes. Thus the same large bandwidth of the single elementary radiator may not be preserved when it

is embedded into array environments.

An illustrative example is given in [10] where the array performance of the Archimedean spiral antennas is compared to that of the Sinuous antenna. Although the Archimedean spiral ($\approx 10 : 1$) has a wider element bandwidth compared to Sinuous antenna ($\approx 9 : 1$), their array bandwidths are $\approx 1.2 : 1$ and $\approx 1.5 : 1$ respectively under 45° scanning condition. This is just due to the bigger size of the spiral antenna, $0.5\lambda/2$, compared to the sinuous antenna, $0.4\lambda/2$. The factors affecting the array bandwidth are discussed in Section 2.2.1 in more detail.

2.2.1 Array bandwidth

According to [5], the bandwidth of an antenna is defined as “the range of frequencies within which the performance of the antenna, with respect to some characteristic, conforms to a specified standard”. In this dissertation the impedance bandwidth is defined for a $VSWR \leq 2$. Two formulations of bandwidth can be presented:

- Bandwidth B_{p-ant} as a percentage. It can be defined as

$$B_{p-ant} = \frac{f_U - f_L}{f_C} 100 \quad [\%] \quad (2.1)$$

where:

- f_U is the upper end of the spectrum;
- f_L is the lower end of the spectrum;
- f_C is the central frequency of the band.

- Bandwidth B_{r-ant} as a ratio. It can be defined as:

$$B_{r-ant} = \frac{f_U}{f_L}. \quad (2.2)$$

In this thesis the percentage bandwidth is going to be used. Moving from element bandwidth to array bandwidth, we assume in a first approximation that we deal with a uniform array which is composed of antenna elements with size dim_2 , and spacing between adjacent elements dim_1 . If ϑ_{max} is the maximum scan angle of the array, on the one hand dim_1 can be related to the ϑ_{max} through the following equation:

$$dim_1 = \frac{\lambda_U}{1 + \sin(\vartheta_{max})} \quad (2.3)$$

where λ_U is the wavelength in free space at the highest frequency of the antenna band. On the other hand, the element size (i.e. dim_2) is proportional to the lowest wavelength of the operation in the plane of a rectangular grid:

$$dim_2 = q\lambda_L \quad (2.4)$$

where λ_L is the wavelength in free space at the lowest frequency of the band.

Selecting the element size as large as possible without overlapping with the adjacent elements, the array bandwidth can be defined by using Eqs. (2.2), (2.3) and (2.4):

$$B_{r\text{-array}} = \frac{1}{q[1 + \sin(\vartheta_{\max})]}. \quad (2.5)$$

Equation (2.5) shows that smaller maximum scan angles, ϑ_{\max} , correspond to larger array bandwidths. From Eq. (2.3), it can be inferred that requiring smaller ϑ_{\max} allows the inter-element distance to become larger. With reference to Eq. (2.5), it shows that the array bandwidth is likely to be determined by the element size rather than the element bandwidth because the element size determines how close the elements can be placed, which is actually important to prevent the grating lobes from occurring. Besides this, a very wide-band element is often physically large and the full bandwidth of the element can not be used because of scan angle limitations. To conclude, in the array design, small inter-element spacing is required to scan the full volume, but minimum spacing is determined by the element size and the mutual coupling between the array elements.

2.2.2 Requirements for UWB antennas

According to the FCC definition [31], a UWB antenna has a fractional bandwidth of 20%, while it has 25% fractional bandwidth in radar domain [44]. Hence, first of all an antenna should have more than a certain value of fractional bandwidth to be called an UWB antenna. Secondly the performance, both the reflection and radiation characteristic of the antenna, should be stable over the entire operational bandwidth of the antenna. Another requirement of the UWB antenna comes from the size of it which should be small enough to be compatible with the UWB unit. Mechanically, they should be low-profile, embeddable and easily integrated for portable devices. For example, the antennas that are required to have omnidirectional radiation patterns and to be used in mobile devices should be small enough to fit in

the mobile terminal. Finally the robustness and the low cost are also key requirements.

After these general requirements, some antenna design parameters are strongly dependent on the modulation schemes that are used by the UWB systems. The Multi-band Orthogonal Frequency Division Multiplexing (MB-OFDM) based wireless communication systems require antenna systems with extremely wide bandwidth covering all operating sub-bands. Similarly pulse-based systems, referred to as Direct Sequence UWB (DS-UWB), require wide impedance bandwidth covering that part of the spectrum where the major pulse energy falls in. A linear phase response of the antenna is also an important parameter in the pulsed-based systems [2].

2.2.3 Approaches to achieve antennas/arrays operating over a wide bandwidth

There are various techniques described in the literature to increase the bandwidth of an array. Using the shared aperture array concept can be such a method. In [12] a frequency independent antenna, the star spiral, is used with variable element sizes to increase the array bandwidth. In [23], a shared aperture technique was used to design an array consisting of two sub-arrays operating at adjacent frequency ranges. These sub-arrays cover a fractional band of more than 10% within the X-band. The first sub-array covers the frequency band of 7.9–8.4GHz and the second sub-array the band of 8.6 – 9.3 GHz. The elementary radiators in the array were cavity-backed, stacked-patch antennas, fed by means of a coaxial probe. The antennas in the array were manufactured in a printed and stratified technology [24]. Although with the shared aperture technique the bandwidth of the array can be increased, this technique has disadvantages, such as the gain of the array being reduced because of sharing the aperture. There will be a less effective antenna area, thus fewer elements, for one frequency band in the aperture since the total area has to be shared with element(s) radiating at other bands. Besides, the array configuration and the feeding structure become more complicated.

Another technique consists of using parasitic patches in microstrip type arrays. In [10], the so-called Four-square antenna was introduced for the first time. This antenna consists of four patches, two of which radiate at low frequencies and are attached to the feed points and the rest radiate as parasitic elements at high frequencies. This antenna was extensively studied in [86] and the bandwidth was further enhanced by modifying the shapes of the patches and using tuning plates under the supporting substrate. One of the

main disadvantages of these antennas is their feeding structure. Although these low-profile antennas have wide bandwidth, feeding them may not be an easy task, especially when an array consisting of a large number of these antennas is under consideration. The antennas are fed by wide-band commercially available hybrids; however, large space is needed for the feeding part in an array environment since every element needs its own hybrid and related cables and the cost of the array therefore increases.

Un-equal array spacings and non-rectangular array geometries can be used instead of traditional uniform spaced arrays. Work on un-equal array spacing started as early as the 1960s [45, 52, 78, 96]. A linear array with arbitrarily distributed elements was studied by Unz [96]. He found that the additional degree of freedom created by the random distribution of elements allowed him to achieve the same performance as with an equally spaced array but with fewer elements. The effects of various un-equal spacing schemes, such as logarithmic spacing, non-monotonically increasing spacing, and elimination of multiple spacing were investigated by King [52]. He found that compared to an equally spaced array fewer elements were required for a desired bandwidth and grating lobes were replaced by sidelobes [12].

The Vivaldi antenna can also be considered as an option to achieve arrays operating over a wide bandwidth, this topic being extensively studied in the literature [35, 41, 54, 94, 99]. This antenna is a kind of slot-line radiator having an endfire-type of radiation. While the Vivaldi antenna itself is planar, they have to be aligned such that the endfire patterns add up to compose the directive array pattern. In other words the individual antennas stick out from the surface where the antennas are embedded. Nevertheless, this topology conflicts with the assumption made in Section 1.2 referring to this thesis focusing on *low* profile UWB antennas. Consequently, this topic will not be presented in this account.

2.2.4 Limitations in achieving wide-band antennas

As discussed before, the operating bandwidth is one of the most important parameters of an antenna, therefore it is crucial to examine the fundamental limits and parameter trade-offs involved in the antenna bandwidth and in the antenna size reduction.

Resonant antennas, such as microstrip antennas, operate at a single resonance mode and the operating bandwidth is related to the antenna quality factor and radiation efficiency. The quality factor Q is a parameter that describes energy transfer in oscillating systems and may be defined as follows:

$$Q = \frac{2\omega W_E}{P_{\text{rad}}}, \quad \text{for } W_E \geq W_M \quad (2.6)$$

$$Q = \frac{2\omega W_M}{P_{\text{rad}}}, \quad \text{for } W_E < W_M \quad (2.7)$$

where:

- W_E and W_M are the time averaged electric and magnetic energy densities in the evanescent field;
- P_{rad} is the radiated power;
- ω is the angular frequency.

Antenna volume or “size” can be related to the Q factor of the antenna, based on the so-called Chu-Harrington Limit where Q is generally accepted to be a measure of antenna bandwidth. The size versus bandwidth capability of an antenna was firstly introduced by Harold Wheeler and L. J. Chu, and later by R. Harrington. Wheeler investigated the radiation characteristics of electrically small antennas [102]; later Chu derived an approximate expression for the minimum radiation Q of a small antenna [19]. Harrington extended the theory of Chu to include circular polarized antennas [39]. After these investigations R.E. Collin, S. Rothchild [22] and R.L. Fante [30] derived exact expressions for the radiation Q based on evanescent energy stored around an antenna. After some further investigations, an exact expression for the antenna Q was formulated as follows [11]:

$$Q = \frac{1}{(ka)^3} + \frac{1}{ka} \quad (2.8)$$

where a is the radius of the sphere enclosing the antenna and $k = 2\pi/\lambda$, λ being the wavelength in free space.

For narrow-band antennas the relation between bandwidth and quality factor can be defined as

$$\frac{1}{BW} = \frac{f}{\Delta f} \cong Q. \quad (2.9)$$

where:

- f is the resonant frequency;

- $\Delta f (= f_H - f_L)$ is the nominal bandwidth where f_L and f_H show the lower and the higher frequency ends of the antenna respectively.

For the wide-band case, describing a precise relationship is difficult but the trend still exists. Experience shows that [11]:

$$Q \cong \frac{[f_L f_H]^{1/2}}{\Delta f}, \quad \text{for } Q \geq 2 \quad (2.10)$$

Comparing Eqs. (2.7), (2.8) and (2.9), it is noted that for substantial radiation from the antenna and large antenna size (i.e., the quality factor of the antenna is small), the bandwidth of the antenna becomes large. According to the Chu limit, the bandwidth of an antenna can be increased by decreasing the antenna efficiency, thereby reducing the gain. In other words, less antenna efficiency provides greater bandwidth for a given size or provides a smaller antenna for a given bandwidth. To summarize, there is a trade-off between antenna size, bandwidth and efficiency, although the antenna efficiency is usually not considered for such trade-offs. A well-designed antenna should be optimised in terms of these parameters according to its application.

In the next chapter new, small, low profile UWB elements, namely the “*Eared*” antenna and the “*Tulip*” loop antenna, will be investigated in detail.

Chapter 3

Design of UWB elements with no ground plane

After our antenna review given in Chapter 2, this chapter discusses the design of two new antennas without any ground plane. The goal of this chapter is introducing new low profile electrically small in size antenna elements having wide impedance bandwidths. The first one is called the “Eared” antenna and the second one has received the name of “Tulip” loop antenna. All aspects of systematic designing the antennas will be discussed. The simulated performance of the antennas will be confirmed via measurements. The operating principles of the UWB characteristics will be investigated by considering one of these antennas (the “Eared” one) as an example. This chapter will be finalized by drawing some conclusions and presenting the novelties related to it.

3.1 Choice for type of radiator

Currently, there is a manifest trend towards developing low-profile, low-cost and small-sized antennas which are suitable for array applications. One of the popular answers to this set of demands is provided by the class of electric type radiators (e.g. microstrip patch antennas) and the other is provided by the class of magnetic type of antennas which can be considered as dual to the microstrip antennas in terms of its distribution of field lines. The microstrip patch antennas do not seem suited for achieving an ultra wide bandwidth. In order to increase the bandwidth in microstrip patch antennas, one method is using stacked patch configurations [70], which increases the complexity and the cost of the structure. An other method can be the

use of parasitic patches which increases the dimension of the single element and may cause grating lobe problems in array environments. Other than the grating lobe, problems can come from surface waves which may have detrimental effects on the antenna performance when the antennas are embedded in array environments. One adequate solution to the suppression of the surface waves is enclosing the radiators with metallic cavities [59] which decreases not only the surface waves but also the mutual coupling between the array elements[23]. However, this method increases the complexity and thus the cost of the antennas. A radical alternative to microstrip antennas consists of moving the feeding section and the ground in the same plane with the radiator. In this manner, beneficial effects can be obtained:

- there is less surface wave coupling between the radiators when they are embedded into array environments;
- the electric field lines are more concentrated in a smaller region so that the coupling effects will decrease.

One should note that the fact that the antenna and the feed network share the same surface induces a certain topology when the radiators are integrated in arrays. This topology is hard to reconcile with a planar array architecture. In view of this observation, the research reported in this dissertation focused on the performance of antennas only in *linear* array environments.

3.2 “Eared” antenna

In this section a CPW-fed printed antenna, which will be hereafter referred to as “Eared” antenna, is going to be described. The antenna is fed by a CPW line (See Appendix E for the details of this feeding method). Similarly structured antennas can be found in [43, 46, 47, 53, 64, 65, 66, 83, 95, 104]. The novelty in the design, except for the very good electrical characteristics, is the possibility to optimize the antenna performance by tuning the dimensions of each antenna section systematically. Since the antenna consists of separate and well-identified sections, effects of modifying the dimensions for individual sections on antenna characteristics can be analyzed. In [43, 64, 65, 66, 95] the radiating section and transition regions are merged into each other, which prevents the occurrence of some resonances, that, in turn reduces the bandwidth. In [46, 47, 66, 83, 104] both the inner parts of the feed sections and the outer parts of the radiating sections are not

rounded; this causes less bandwidth due to diffraction and ripples on the patterns due to edge diffraction respectively. In the “Eared” antenna, which will be explained in the next section, all these points which cause weak performance of earlier designs are taken into account and corrected in order to get sufficient and better performance of the new antenna. Important parameters which affect the antenna performances are investigated both numerically and experimentally to obtain some quantitative guidelines for designing these type of antennas.

3.2.1 Design procedure

The geometry of the antenna is depicted in Fig. 3.1. The antenna is designed on the commercially available Duroid RT 5870 high frequency laminate with a relative permittivity $\epsilon_r = 2.33$. The substrate height is $h = 0.787$ mm, the cladding thickness is $t = 17 \mu\text{m}$ and the loss tangent amounts to $\tan(\delta) = 0.0027$ at an operating frequency of $f_0 = 9$ GHz.

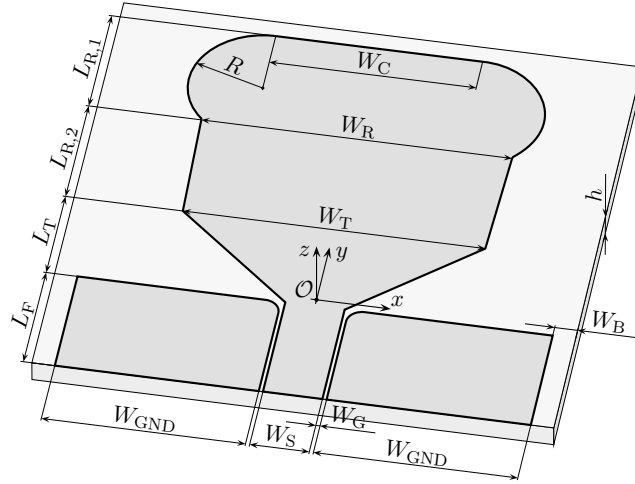


Figure 3.1: Configuration of the proposed CPW-fed, quasi-magnetic antenna.

This quasi-magnetic radiator (See Appendix B for the details of this concept) fed by a CPW (a quasi-TEM type of feeding) consists of three main sections, namely the feed, the transition and the radiation part. All conducting components are etched on the top layer of the laminate; the center part constitutes the signal path while the two adjacent patches act as grounds (GND). The antenna was first optimized by means of a grid-search strategy using a “method of moment” - based, planar software as computational

engine (Advanced Design System) [1]. All the rest of the simulations in this dissertations were performed by means of the finite-integration, time-domain package CST Microwave Studio [26].

3.2.2 Determination of the basic dimensions of the original antenna

Feed section

The CPW's impedance mainly depends on the ratio of the signal-gap-width (see Eq (E.17), explained in Appendix E). This feature provides flexibility for designing the width of the signal line which is chosen "wide enough" to conduct the current flowing on the signal line. Theoretically, the length of the feed section can be chosen arbitrarily since this section introduces only an additional phase shift. However, for practical reasons of retaining small-size, avoiding unnecessary loss, having enough length for soldering the SMA connector and providing enough conversion distance for the TEM to quasi-TEM field-discontinuity between the coax and the CPW, the practical length of the feeding section is often chosen as $1/8$ of the guided wavelength (λ_g). Intentionally, we chose a distance a bit longer than $\lambda_g/8$, namely $L_F = 4.25$ mm. Here λ_g is defined as $\lambda/\sqrt{\epsilon_{eff}}$ where λ is the free space wave length and ϵ_{eff} is some effective permittivity that applies to the domain occupied by the radiator.

The width of the GND is chosen such that the width of the antenna ($2W_{GND} + 2W_G + W_S$) is half of the free-space wave length at 9 GHz. The inner corners of the GNDs at the neck of the transition region is rounded to produce a smoother impedance transformation from the feed section to the transition section.

Transition region

The tapering length L_T is often chosen between $\lambda_g/8$ and $\lambda_g/4$. The start value is chosen as the shortest one, $L_T = 3.37$ mm, however the grid search optimization found a longer value as local optimum; i.e $L_{T,opt} = 3.64$ mm.

Radiation region

The start value of the length of the resonator length is often chosen as $3/8\lambda_g = L_R = 10.1$ mm. The computer optimized value converged to 8.68 mm. The initial value of the width of the radiation section is

$W_T = \lambda_g/2 = 13.4$ mm [6, p. 732], however the optimized value converged to 10.2 mm. To mitigate the edge diffraction, two edges of the radiating part are replaced by two arcs in order to avoid the antenna having sharp corners. This choice is also expected to lower the mutual coupling between neighboring elements, when such radiators are included in an array. All geometric parameters of the antenna are summarized in Table 3.1.

Table 3.1: Geometric parameters of the proposed “Eared” antenna.

Parameter	Dimension [mm]	Description (see Fig. 3.1)
L_F	4.25	Length of the feed section
W_{GND}	6.86	Width of the ground
W_S	2	Width of the signal line
W_G	0.14	Width of the CPW’s gap
L_T	3.64	Tapering length in transition region
W_T	10.2	Upper tapering length in transition region
$L_R =$ $L_{R1} +$ L_{R2}	8.68	Resonator length in radiating region
W_R	10.5	Resonator width in radiating region
W_C	7	Circle’s separation width
R	2.5	Radius of top circular areas

The optimized structure has then been fabricated; and the antenna is depicted in Fig. 3.2. The comparison of the simulated and measured return losses is presented in Fig. 3.3. It can be concluded that the simulations indicated a VSWR ≤ 2 impedance bandwidth of 86.7%, stretching between 5.76 and 14.6 GHz. The measured bandwidth exceeded the simulation predictions and it covered the range from 4.36 to 14.48 GHz, translating into a relative bandwidth of 107.4%. In Fig. 3.3, the dissimilarity between simulation and measurement around 5 GHz, is caused by the soldering effect and the connector of the antenna as CPW, which is a quasi-TEM type of feeding is connected to an SMA connector (TEM type of feeding). Because

the two structures support different propagation modes, they are not suitable to be used together. However, for the purpose of testing and evaluating the design, an SMA connector has been soldered to the CPW, thus significant reflection can be expected at the SMA-CPW junction.

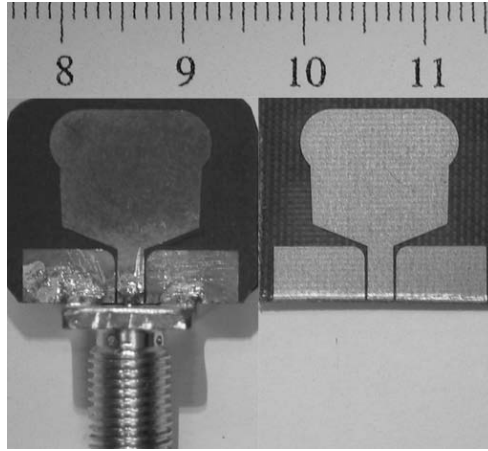


Figure 3.2: Fabricated “Eared” antenna – initial variant, with and without the pertaining SMA connector.

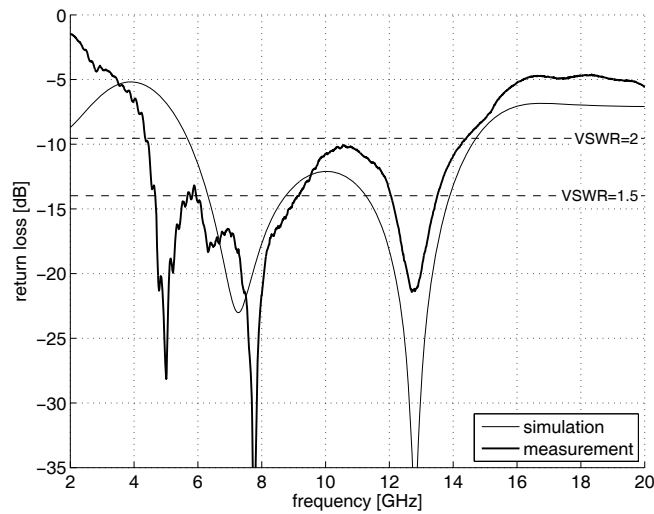
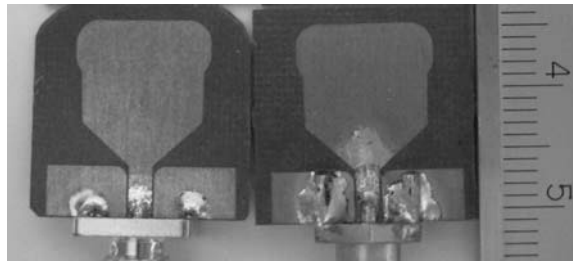


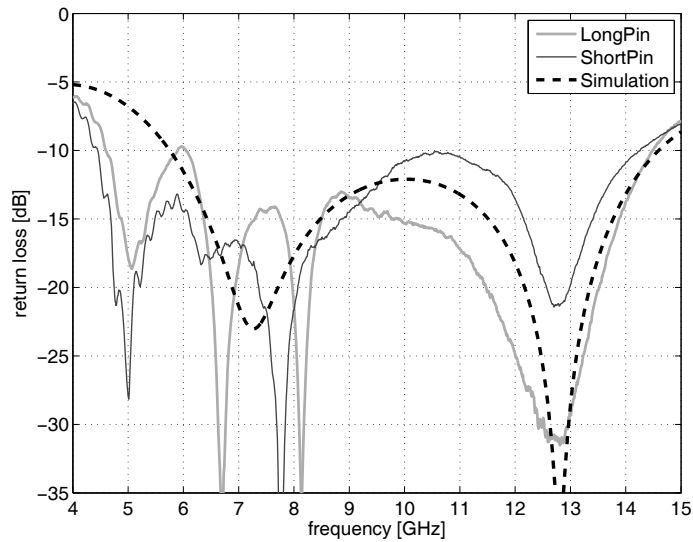
Figure 3.3: Simulation and measurement results concerning the original antenna.

Effect of soldering:

As just stated, a reflection is expected at the SMA-CPW connection which is also due to the effect of the soldering. The exact geometry of the soldering entails a random component which is very difficult to control. In Fig. 3.4 (a), the same antenna with SMA connectors can be seen, the right antenna being soldered without cutting the inner pin and the outer “stubs” of the connector, while the inner pin and the outer “stubs” of the connector of the left antenna are cut and the antenna is soldered more neatly.



a



b

Figure 3.4: Effect of soldering (a) “Eared” antenna, with a SMA connector with long pin and short pin; (b) Simulation and measurement results concerning the original antenna.

The measurement results of the antennas are depicted in Fig. 3.4 (b).

As can be seen from the figure, there is an extra resonance in the measurement of the antenna that have SMA connectors with long inner pin and longer outer “stubs”. When the antenna is soldered in this way, the cladding of the CPW section is increased more than 100 times. As stated before, the cladding of the antenna should be 0.017 mm. However, by soldering (as visualized in Fig. 3.4 (a) (right)), the thickness of the CPW is increased which alters the impedance. Thus, an unexpected extra resonance occurs. To be able to have a measurement which can be comparable with the simulations, the CPW should be disturbed as little as possible by the soldering.

3.2.3 Optimization of the antenna

In order to improve the performance of the configuration depicted in Fig. 3.1, all physical antenna parameters affecting the operational features had to be thoroughly examined.

Obviously, each of the geometrical parameters introduced in Fig. 3.1 has its effect on the overall performance of the antenna and, in particular, on the impedance bandwidth. Nevertheless, the investigation of all parameters in view of obtaining a global optimum is at least a very time consuming task. Alternatively, resorting to stochastic optimization methods may result in (often, marginal) performance enhancements, but does certainly not guarantee the convergence of the process.

The effectiveness of the design strategy can be greatly improved by closely observing the physics of the examined antenna. The following steps have been undertaken:

- separate and understand the role of each section;
- identify the sections that predominantly influence the impedance matching;
- select the most important geometrical parameter associated to each section;
- isolate the effect of that parameter so that an optimization on that parameter, only, can be taken place without affecting too much the effect of the other sections.

This strategy was followed step-by-step, by firstly studying the current distribution of the original antenna. The relevant results, depicted in Fig. 3.5, give evidence of a high current concentration along the edges of the

transition. This shows the important role of this section for connecting the non-radiating CPW feeding to the radiating part. Based on this, we conjectured that the transition’s flare, measured by the angle between the ground plane and its edge, is the geometric parameter that influences mostly the matching of the two sections. For ensuring more flexibility of the optimization process, we intentionally split this single parameter into two separate parameters, namely L_T and W_T . In view of our design philosophy based on sectioning the global configuration into functional components, we used L_T for optimization of the transition, while reserving the complementary parameter W_T for the design of the radiation section.

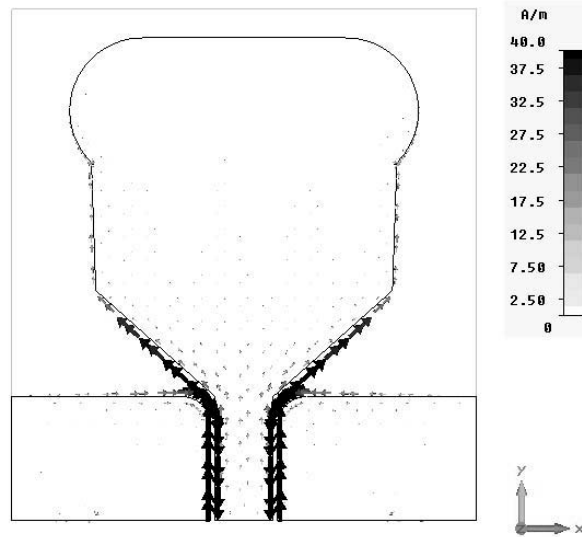


Figure 3.5: Current distribution on the surface of the “Eared” antenna at 9 GHz.

Preliminary investigations have demonstrated that, by modifying the transition length L_T , the antenna resonances can be varied, de-coupled or shifted in order to obtain a wider impedance bandwidth. Consequently, it was decided to use L_T as main parameter for re-optimization of the antenna.

It was observed that there were local, quite deep, resonances (see Fig. 3.3). Nonetheless, by better balancing these resonances, it was expected that a wider bandwidth could be obtained, possibly at the cost of trading-off the very low return loss at the relevant resonant frequencies. This conclusion was confirmed by the parameter study reported in Fig. 3.6. In the figure $L_{T,0}$ designates the value of the L_T parameter that was stated in Table 3.1, namely $L_{T,0} = 3.64\text{mm}$. From the plot it can be easily derived that an

extension in the transition length results in two resonances being increasingly clearly separated, which is not desirable. On the contrary, decreasing the L_T length has beneficial results. For example, decreasing this length by 1 mm yields a very deep resonance at about 12.6 GHz. By further decreasing the length to $L_{T,0} - 2$ mm, the two resonances are, virtually, joined and a maximum bandwidth can be obtained. Upon decreasing L_T further, the bandwidth deteriorates rapidly and, practically vanishes at approximately $L_T = L_{T,0} - 3$ mm.

This parameter study yields now the conclusion that the optimum value of the transition's length is 1.64 mm, instead of the original 3.64 mm value.

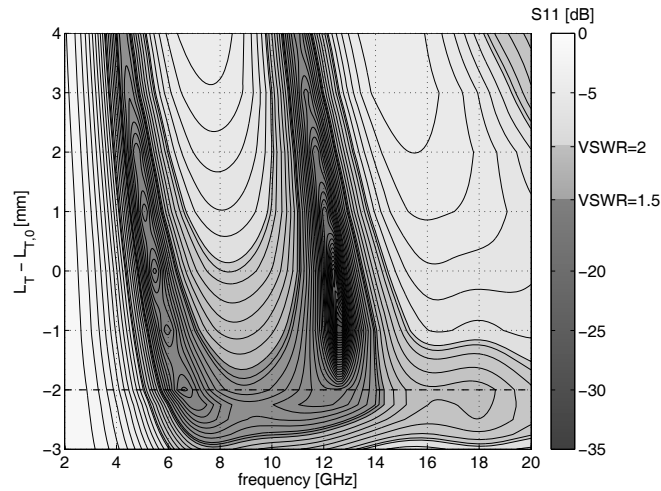


Figure 3.6: Frequency dependence of the return loss for different values of the transition length L_T .

The value of the transition length L_T derived in the section above was employed as a basis for re-designing the CPW-fed quasi-magnetic printed antenna. The designed configuration was then fabricated; the device with and without the SMA connector soldered is illustrated in Fig. 3.7.

Since the far-field radiation patterns of the antenna shown in Fig. 3.7 are intended to be measured, the feed section of the antenna connector should then be modified. In the current configuration, the flange of the connector has a great effect on the radiation performance, so it is not feasible to measure the radiation patterns of the antenna having such short feed. The antenna is modified for pattern measurements in such a way that $L_F = 4.25 + 40 = 44.25$ mm as depicted in Fig. 3.8.

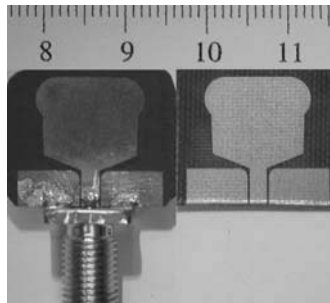


Figure 3.7: Optimized “Eared” antenna, with and without the pertaining SMA connector.

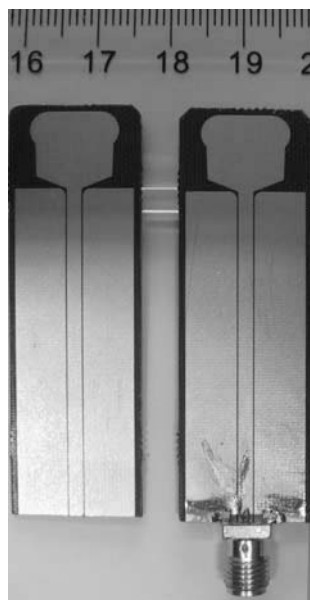


Figure 3.8: Optimized “Eared” antenna with longer feed section, with and without the pertaining SMA connector.

3.2.4 Validation of the optimization process

S parameter measurements

The simulated and measured results corresponding to this new design are depicted in Fig. 3.9. In the measurement of the antenna, the time-domain de-embedding technique (See Appendix C) was used in order to eliminate the soldering and the connector effect. The simulated data indicates an operational impedance bandwidth for a $VSWR \leq 2$ of 113.6%, stretching

over the frequency range $5.51 \div 20$ GHz. The measured S_{11} yields an operational bandwidth from 5.11 GHz up to in excess of 20 GHz (where the explored frequency band ends). Upon taking these values as a reference, the corresponding relative bandwidth amounts to 118.6%.

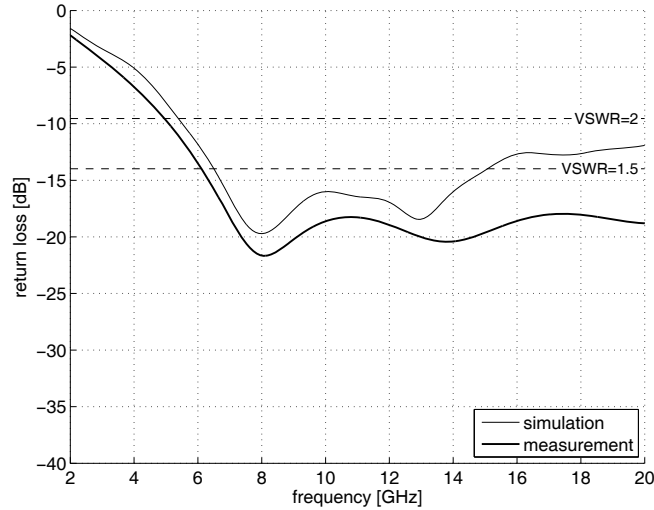


Figure 3.9: Simulation and measurement results concerning the optimized “Eared” antenna.

Radiation pattern measurements

To examine the antenna-radiation performance, experimental measurements were carried out in DUCAT (Delft Unechoic Chamber for Antenna Tests). Although the radiation patterns were measured between 5 – 18 GHz, the patterns at 5.6, 10.5 and 15 GHz are presented in this section only. The radiation characteristics are investigated in three different principal planes (See Section 1.6 for the definition of the employed reference frame).

xOz – plane ($\phi = 0^\circ$ cut) radiation patterns

As depicted in Fig. 3.1, the antenna is laying on xOy – plane. The measured co-polarization and cross-polarization patterns corresponding to the $\phi = 0^\circ$ cut are shown in Fig. 3.11. From the patterns, this antenna exhibits very good omnidirectional patterns in the xOz – plane. At all frequencies, i.e. at 5.6 GHz, 10.5 GHz and 15 GHz, the co- to cross-polar ratio is good. It can be observed that in the worst case, that is at the highest frequency, this ratio

is more than 8 dB. Around the design frequency, i.e. at 10.5 GHz, a best co-to cross-polar ratio is observed which is more than 25 dB.

yOz – plane ($\phi = 90^\circ$ cut) radiation patterns

Due to the mounting of the antenna (shown in Fig. 3.10), it was not possible to measure the back side of the antenna, thus only half of the radiation patterns are provided in Fig. 3.12. In the symmetry plane of the antenna, yOz – plane, theoretically no cross polar components are expected as all cross polar components on the yOz – plane cancel each other. In a real case scenario, some cross polar components are observed, their level being, nonetheless, extremely low.

xOy – plane (θ cut) radiation patterns

Due to the same reasoning given for the yOz – plane radiation patterns, only half of the radiation patterns are provided. The measured co-polarization and cross-polarization patterns can be seen in Fig. 3.13. The co-polar radiation pattern displays a deep notch for $\phi = 90^\circ$, i.e. along the symmetry axis of the antenna. The co- to cross-polar ratio is better than in the case of the xOz – plane.

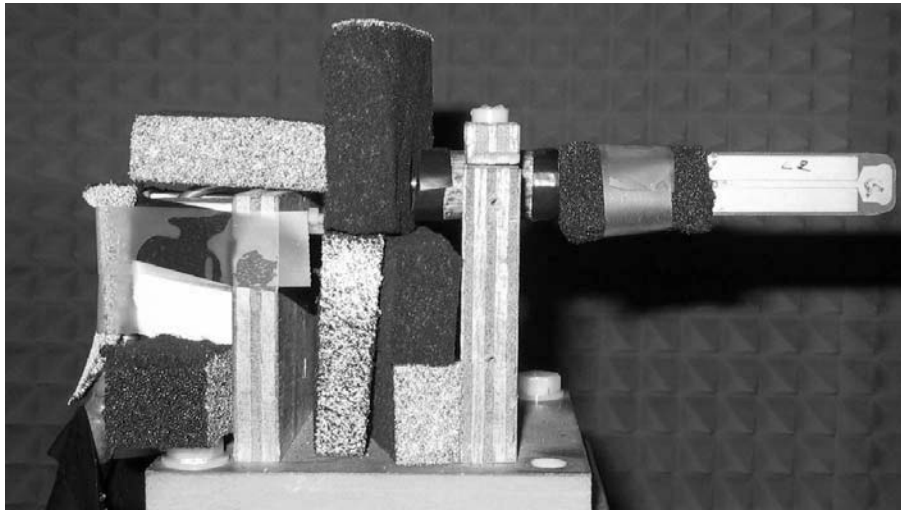


Figure 3.10: Antenna under test while measuring the $\phi = 90^\circ$ plane.

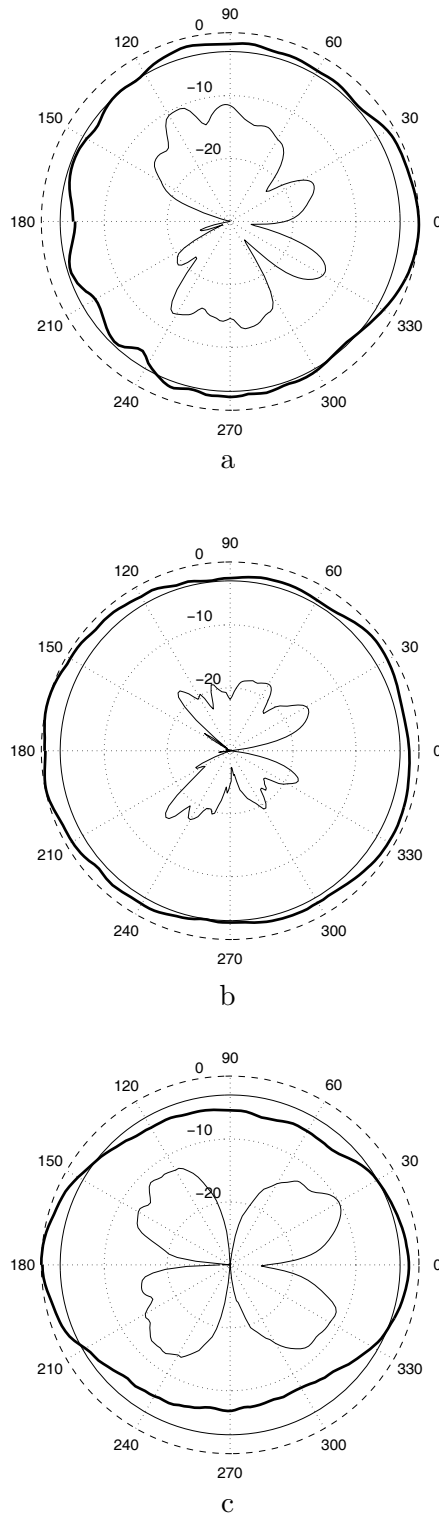


Figure 3.11: Measured radiation patterns at $\phi = 0^\circ$ cut (a) 5.6 GHz; (b) 10.5 GHz; (c) 15 GHz: thick line – co-polar component; thin line – cross-polar component.

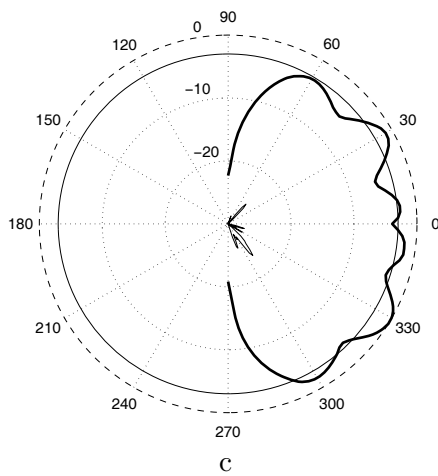
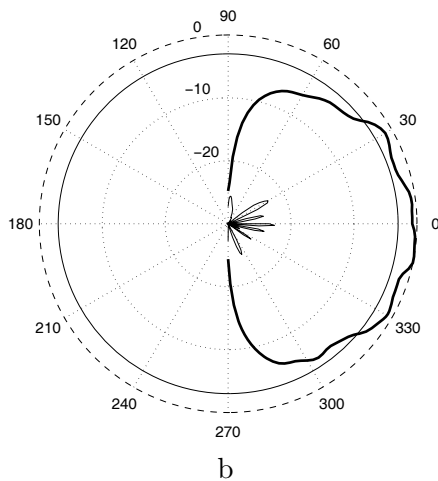
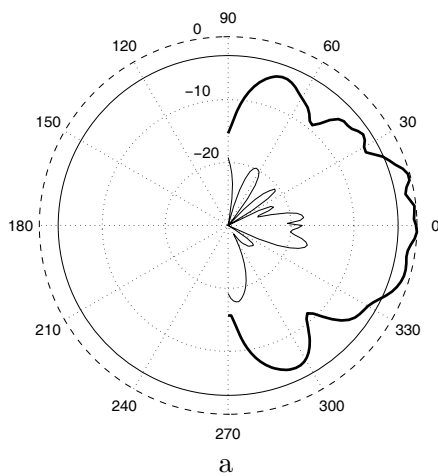


Figure 3.12: Measured radiation patterns at $\phi = 90^\circ$ cut (a) 5.6 GHz; (b) 10.5 GHz; (c) 15 GHz: thick line – co-polar component; thin line – cross-polar component.

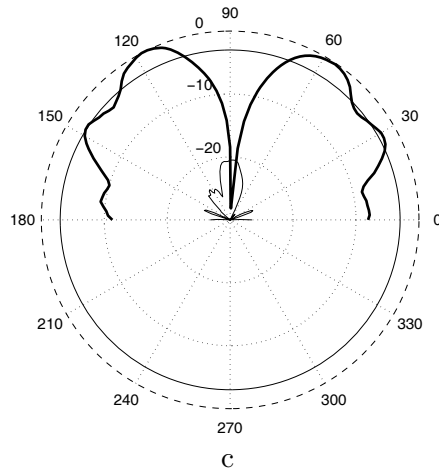
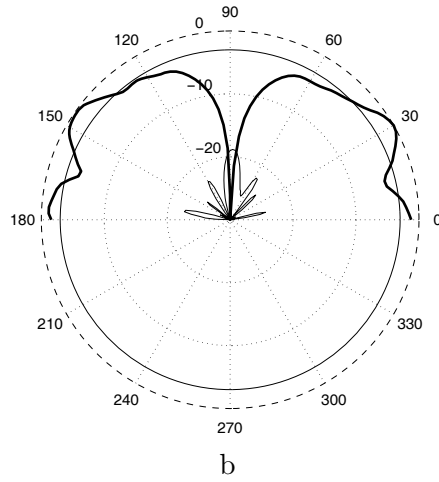
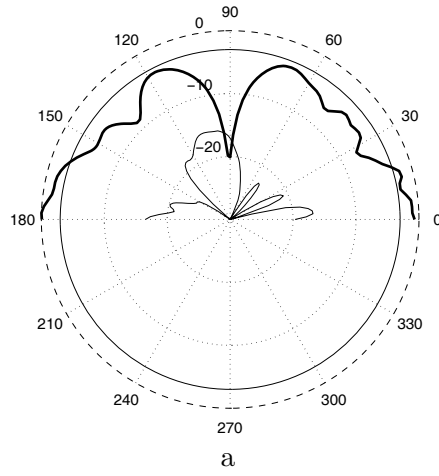


Figure 3.13: Measured radiation patterns at $\theta = 85^\circ$ cut (a) 5.6 GHz; (b) 10.5 GHz; (c) 15 GHz: thick line – co-polar component; thin line – cross-polar component.

Effect of the feed section of the antenna on the radiation characteristics

In Paragraph 3.2.3, it was motivated that radiation pattern measurements require a long feed length $L_F = 4.25 + 40 = 44.25$ mm. In this case, it is noticed that the feed section of the antenna is extremely long compared to the antenna itself. Thus, it is needed to investigate the effect of the feed section on the antenna performance.

Actually, little loss in the feeding structure of the antenna was expected, knowing that CPW feed lines reduce the loss in feeding networks (especially compared to the microstrip lines) [16], [25]. This has to be proven through measurements. The antenna was therefore measured without absorber and with absorber on the feed section (see Fig. 3.14). Since the investigated antenna has a bi-directional beam, it is necessary to investigate the effect of the feed section in the complete hemisphere. Thus the radiation patterns with/without the absorbing shield in the xOz – cut is depicted in Fig. 3.15 at three frequencies. In Fig. 3.15, it can be noticed that the difference between the radiation patterns are well under 0.5 dB, a value that can be attributed to doing the measurements at different times. Since there is no significant difference between the two plots, it can be concluded that there is no radiation effect caused by the feeding section of the antenna. (This material has been published as a journal paper [92].)

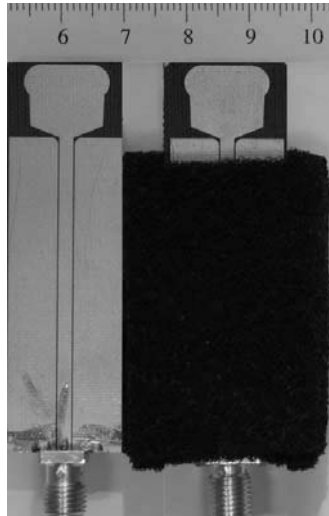


Figure 3.14: Antenna with/without absorber on its feed section

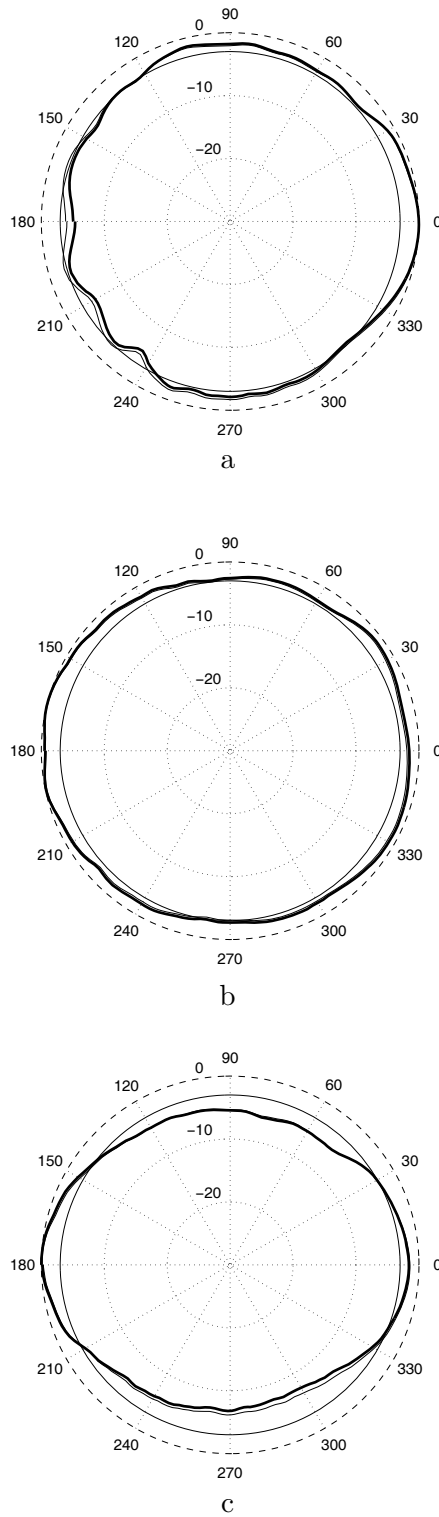


Figure 3.15: Comparison between the normalized radiation patterns (in decibels) corresponding to the $\{\phi = 0^\circ; \phi = 180^\circ\}$ cut, (a) 5.6 GHz; (b) 10.5 GHz; (c) 15 GHz: thick line – co-polar component, without the absorber shield; thin line – co-polar component, with the absorber shield.

3.2.5 Further optimization of the antenna

The analysis in Section 3.2.3 has focused on optimization of the L_T dimension, based on the observation that the currents are mainly concentrated in the tapering section. In this manner, an operational impedance bandwidth of 118.6% has been achieved. In this section, other parameters which have an effect on increasing the impedance bandwidth of the antenna are investigated. Firstly the effect of W_T is explored as W_T is located in a very critical place and controls the width of the transition region between the feeding and the radiation sections. The effect of this parameter is depicted in Fig. 3.16.

In this figure, $W_{T,0}$ designates the value of the W_T parameter as given in Table 3.1, namely $W_{T,0} = 10.2$ mm. From the plot, it can be derived that decreasing this dimension by 1 mm results in a better impedance matching. This can be considered as an optimum value since decreasing it further results in a poorer performance in terms of reflection coefficient.

After fixing W_T to 9.2 mm, the effect of L_{R2} is then investigated. The result of this study is depicted in Fig. 3.17. Here, again, $L_{R2,0}$ shows the value of the L_{R2} in Table 3.1. From Fig. 3.17, it can be understood that decreasing $L_{R2,0}$ results in a better impedance matching. In this figure, we note that, $L_{R2} - L_{R2,0} = -2.5$ mm gives globally the most *balanced* impedance bandwidth.

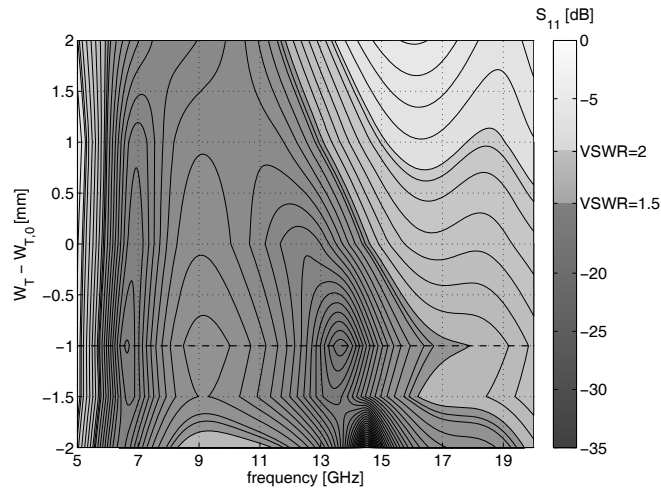


Figure 3.16: Frequency dependence of the return loss for different values of W_T , the upper tapering length of the transition region.

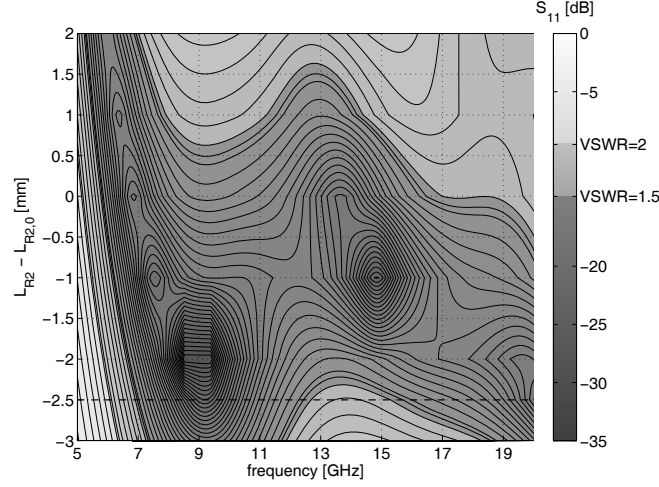


Figure 3.17: Frequency dependence of the return loss for different values of L_{R2} , the resonator length of the radiating region.

3.2.6 Validation of the final optimization

S parameter measurements

It should be noted that all optimization experiments were conducted between 5 to 20 GHz, only, for maintaining computational feasibility. For the same reason, the length of the feeding section, i.e. L_F in Fig. 3.1, was deliberately kept short (4.25 mm). Once the optimization was completed, the feeding section was extended by 40 mm, again for the same reasoning as given in Paragraph 3.2.3. The final optimized radiator is depicted in Fig. 3.18 and Fig. 3.19.

The optimized radiator, together with the extended feeding line, was finally simulated over the frequency band 5 to 45 GHz; the simulation and measurement results are depicted in Fig. 3.20. In the measurement of the antenna, the time-domain de-embedding technique (See Appendix C) was used in order to eliminate the soldering and connector effect.

Radiation pattern measurements

The radiation patterns are measured in the principal planes of the antenna. The measured results at 11 GHz are depicted in Fig. 3.21. In Fig. 3.21 (a), the antenna shows, as explained before, omnidirectional radiation patterns with 10dB co- to cross pol ratio in the worst case. Due to the mounting of

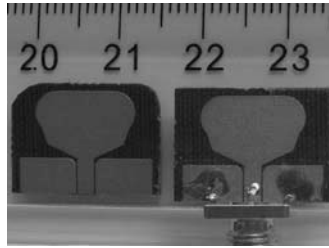


Figure 3.18: Final version of the optimized “Eared” antenna, with and without the pertaining SMA connector.

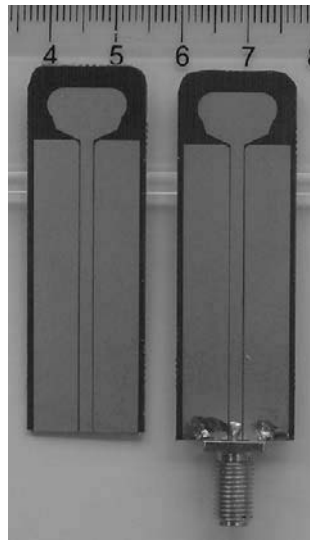


Figure 3.19: Final-optimized “Eared” antenna with longer feed section, with and without the pertaining SMA connector.

the antenna which is explained in Paragraph 3.2.4, only half of the radiation patterns are provided for the yOz - and xOy - planes. Along the symmetry axis of the antenna the radiation pattern for the yOz - plane displays a deep notch for $\phi = 90^\circ$ (see Fig. 3.21 (b)).

3.3 Operating principles and investigation of UWB characteristics

At present there are numerous demands for wireless Ultra Wide-band (UWB) systems. These concern new RF components such as antennas, filters etc. In

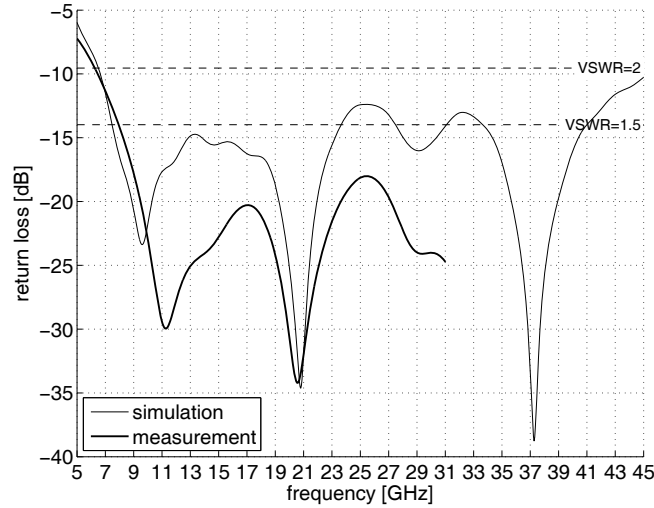


Figure 3.20: Simulation and measurement results concerning the final optimized “Eared” antenna. Measurements were clipped at 31 GHz which is taken as the upper limit for the bandwidth of the employed SMA connector.

the antenna field, a hot topic concerns the developing of UWB antennas that are important especially for high data rate communication. Many examples of UWB antennas are readily available in literature, such as those discussed in [37, 61, 62, 63, 66, 93, 97]. In [37], [66], [93] and [97] the design rules are summarized and, then, results of reflection and radiation characteristics are presented. It is, nevertheless, noteworthy that the working principles of these UWB antennas are seldom touched upon. Only a brief mention of current distributions for a circular disk monopole antenna is given in [62], which is later followed by few conclusions about the working principles of UWB antennas in [61, 63].

This section fills this gap by investigating in depth these operating principles. It focuses on the magnetic (H -)field distribution, (and, implicitly, on the relevant current distribution) on the contour of the antenna, since this is a particular feature of UWB antennas [17]. Starting from a concrete example of UWB antenna, namely the CPW-fed, quasi-magnetic printed “Eared” antenna depicted in Fig. 3.19, this novel approach relates the traveling wave characteristics to the ultra wide bandwidth performance

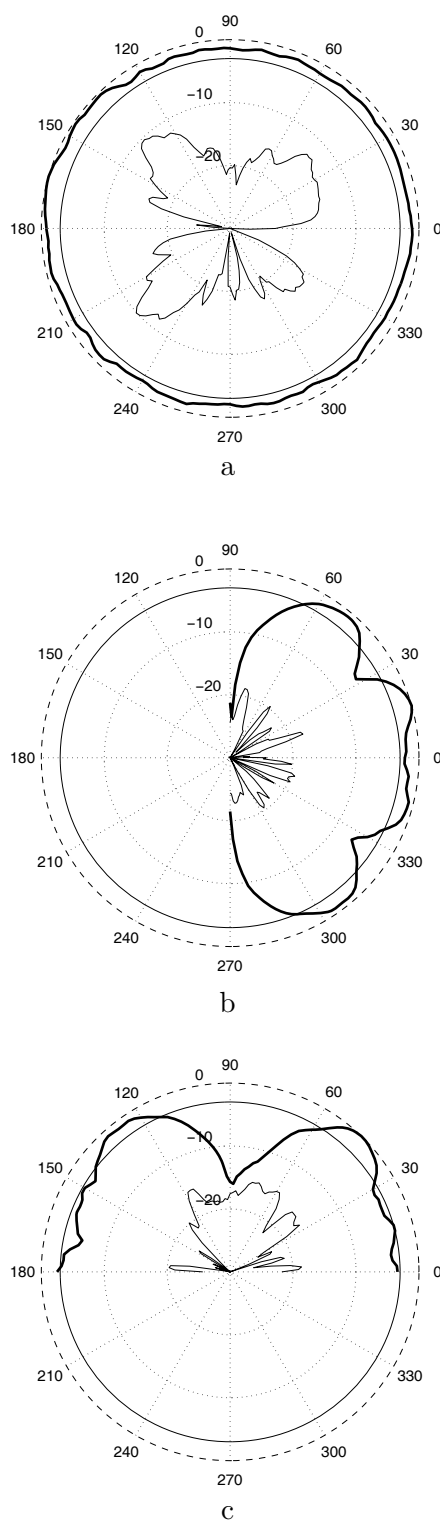


Figure 3.21: Normalized measured radiation patterns (in decibels) at 11 GHz: thick line – co-polar component; thin line – cross polar component. (a) $\{\phi = 0^\circ; \phi = 180^\circ\}$ cut; (b) $\{\phi = 90^\circ; \phi = 270^\circ\}$ cut; (c) $\theta = 85^\circ$ cut.

via the H -field distributions for the low-profile, planar antennas. The behavior of the H -fields are a good indication for the antenna supporting the traveling wave characteristics.

3.3.1 Summary of the antenna operating principles

The analysis of the behavior of the CPW-fed (so-called quasi-magnetic) antenna outlined previously allows the derivation of some more general UWB principles. In this respect, the simulated results in Fig. 3.20 show that this antenna is capable of supporting multiple resonances, the resonance being defined as the frequency where a return loss curve dip is located. The current distributions at the resonant frequencies, namely at 9.5 GHz, 20.8 GHz, 29 GHz and 37.3 GHz are going to be investigated. The first resonant frequency is primarily determined by the length of the antenna, i.e. $L_{\text{ant}} = L_{\text{R1}} + L_{\text{R2}} + L_{\text{T}}$. Note that at this frequency $L_{\text{ant}}/4$ equals approximately $\lambda_{\text{g}}/4$, with $\lambda_{\text{g}} = \lambda/\sqrt{\epsilon_{\text{eff}}}$ denoting the guided wavelength; here λ is the free space wavelength and ϵ_{eff} is some effective permittivity that applies for the domain occupied by the radiator.

The antenna can be considered as being composed of different sections. The first resonance is determined by the length of the whole antenna, as explained previously. Higher resonant frequencies are determined by different combinations of antenna sections. It can be seen from Fig. 3.20 that the resonant frequencies are not widely separated. Since they are closely spaced, or even overlapping, their collective effect is the UWB behavior of the antenna.

3.3.2 Traveling wave characteristic and their impact on the UWB performance

One effective way of analyzing the antenna behavior is by checking the current distributions. These current distributions are calculated by means of the (commercially available) CST Microwave Studio software [26] at all resonant frequencies.

The first observation that is derived from the current plots is that the currents are primarily distributed along the edges of the antenna at all investigated frequencies. Furthermore, they are, practically, confined to the transition part of the antenna, a phenomenon that is increasingly pronounced at higher frequencies, as demonstrated by the current distribution in Fig. 3.22. It appears that the amplitude of the current distributions decreases when going far away from the transition region of the antenna.

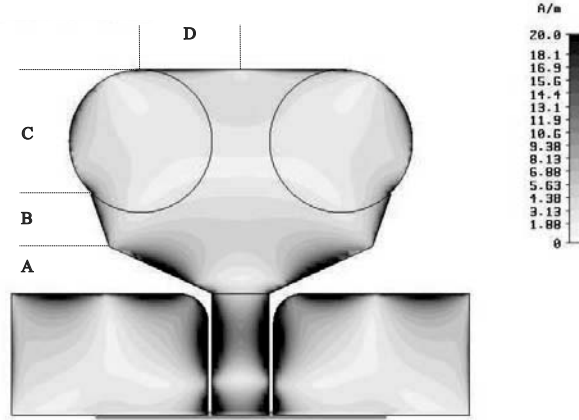


Figure 3.22: Current distribution in the CPW-fed, quasi magnetic antenna at 37.3 GHz, with sections of the antenna labeled.

From the figure, it can be observed that at the highest resonant frequency (i.e. at 37.3 GHz) there are 4 $\lambda/2$ cycles on the half contour¹ of the antenna, that allows for interpreting the antenna behavior as that at a 4th order harmonic.

The current distributions at different phases (time instants) are investigated in order to understand the complete functioning of the antenna. The absolute values of the real parts of the H -fields at different phases of the current at the CPW input are going to be studied. The H -field values at the edge of the antenna, divided into the 4 sub-contours labeled as **A**, **B**, **C**, **D** in Fig. 3.22, are obtained via CST and combined in MATLAB in order to have the complete field distribution on half of the antenna circumference. The vertical dashed lines in Figs. 3.23–3.26 correspond to the boundaries between the sub-contours defined in Fig. 3.22.

The H -field distributions at 9.5 GHz, 20.8 GHz, 29 GHz and 37.3 GHz are depicted in Figs. 3.23–3.26 for 3 different phase values (time instants) of the current at the CPW input. All figures show that the power has an exponentially decaying profile, being representative for a *lossy traveling wave*. Thus, it can be inferred that the antenna shown in Fig. 3.19 supports traveling wave characteristics.

From Fig. 3.23, it can be seen that the current has traveling wave characteristics without any ripples. When the frequency increases, the behavior

¹The half contour consists of the **A**, **B**, **C**, **D** sections of the antenna in Fig. 3.22.

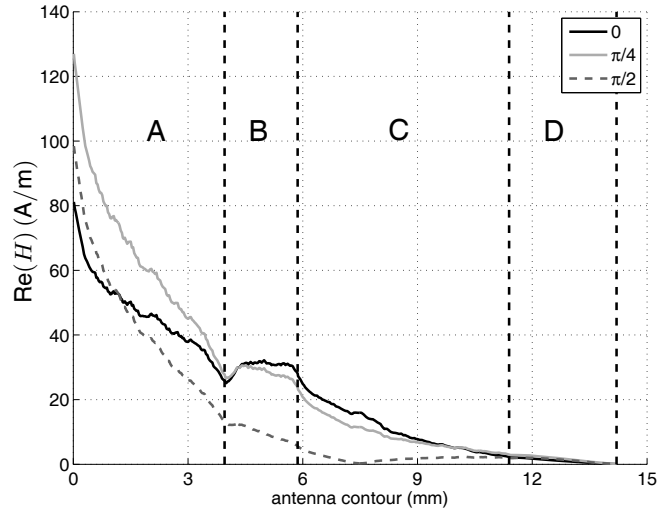


Figure 3.23: H-field distribution (at different phases) at 9.5 GHz.

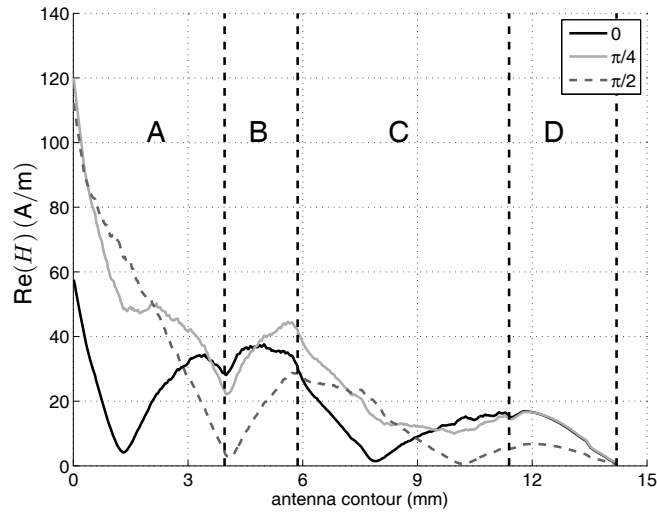


Figure 3.24: H-field distribution (at different phases) at 20.8 GHz.

of the current becomes more complicated and, thus, difficult to analyze. Upon increasing the frequency, the current seems to be *traveling* along the edge of the antenna with modulations on the H -field curves which are due to the reflections from the different parts of the antenna. It can be observed that these modulations change for different phases of the CPW input

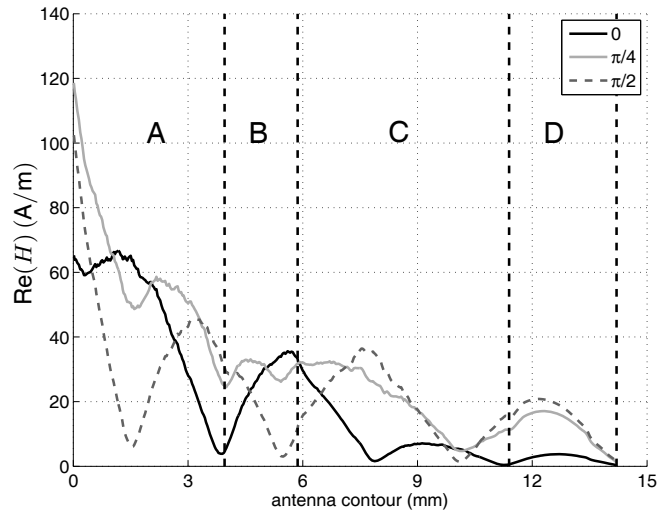


Figure 3.25: H-field distribution (at different phases) at 29 GHz.

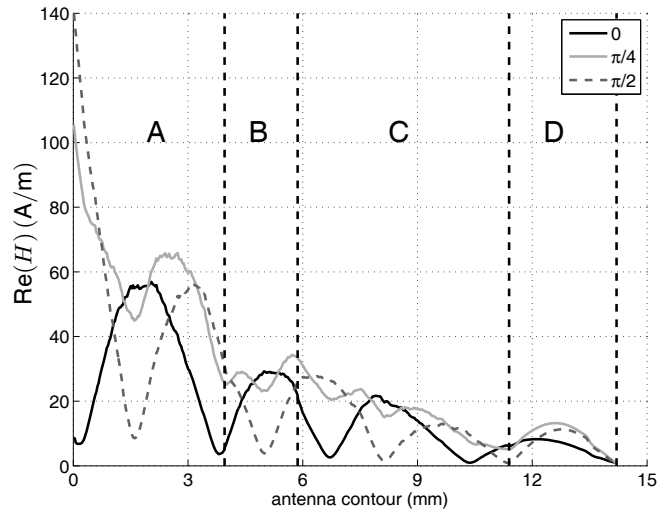


Figure 3.26: H-field distribution (at different phases) at 37.3 GHz.

current. Apart from the dominant traveling wave characteristics of the currents, there are also multiple resonances and multiple reflections which cause the deep resonances in the return loss curve depicted in Fig. 3.20; however these effects do not disturb the traveling wave characteristics of the antenna. This means that between two consecutive resonant frequencies, the antenna

can still radiate ($S_{11} \leq -10$ dB). Another observation that can be inferred from these H -field graphs is that the transition part of the antenna is the most effective part in the radiation mechanism of the antenna since the current decreases rapidly in the transition region, as can be observed from the first part of the plots depicted in Figs. 3.23–3.26.

In Figs. 3.23 to 3.26, the H -fields on the contour of the antenna are presented for different phases of the input current in order to monitor the zeros of the current traveling along the antenna contour, as a function of time. This can be seen more clearly at higher frequencies, i.e. in Fig. 3.26, due to the large electrical size of the antenna. As discussed in [98] ultra wideband is achieved (as a rule) by traveling wave antennas and this is also demonstrated in the case of the antenna under study that, indeed, supports traveling waves. The presented principles can be extended to a more general class of UWB, low profile antennas. (This material will be published as a journal paper [88].)

3.4 “Tulip” loop antenna

In Section 3.2, the “Eared” antenna was studied in detail. The design parameters, experimental results together with the working principles were comprehensively discussed. In this section another type of antenna, namely the “Tulip” loop antenna is investigated. Due to the various advantages of the CPW feeding method this type of feeding is going to be used also in the design of the “Tulip” loop antenna. Because of the advantages of this type of feeding, it is possible to find various CPW-fed loop antennas in literature [18], [27], [60], [87], [106]. Upon focusing on CPW-fed loop type radiators with matching stubs, their common drawback is their big size, so it is not convenient to use them in linear array environments. In [18], a wide bandwidth of 60% is achieved by a CPW-fed loop antenna having four metallic strips protruding from the four slot corners into the slot center. However, the size of the antenna is 40 mm (0.6λ at the highest end of the frequency band). In [60], there is the same problem, the size of the antenna being of approximately 1.8λ at 12 GHz. Although [87] claims to have proposed a *small* antenna (25 mm by 14 mm), the relevant device is still not smaller than 0.9λ at the highest end of the frequency band. Moreover, for reducing the dimensions of the antenna, a staircase shape of the antenna is used, which makes the structure complicated. Finally, in [106], besides the large size of the antenna, the structure of the stub is complex, so it is difficult to control the effects on the bandwidth due to the shape of the stub.

Hereafter, a wide bandwidth and electrically small loop antenna having

a simple shape will be introduced. Design parameters, related experiments and related comments will be given.

3.4.1 Antenna design

The designed “Tulip” loop antenna is depicted in Fig. 3.27. It consists of a loop which is responsible for the radiation, and a tuning stub inserted in the loop, to control the impedance matching. Investigations show that the impedance matching for the proposed antenna strongly depends on the location and on the size of the tuning stub. The impedance bandwidth is mainly determined by the length of the stub (l) and the gap (w_c) between the stub and the ground plane. The antenna is designed on the commercially available Duroid RO 4003 high frequency laminate with a relative permittivity $\epsilon_r = 3.55$. The substrate height is $h = 0.812$ mm, the cladding thickness is $t = 17 \mu\text{m}$. The characteristic impedance of the feeding CPW transmission line is 50Ω . The loop is designed to have a dimension approximately $\lambda_g/2$ at the operating center frequency $f_0 = 10$ GHz. Here λ_g is defined as $\lambda/\sqrt{\epsilon_{eff}}$. Hence, the maximum dimension of the antenna in the x direction is 11 mm, including the metallic walls enclosing the loop itself (W dimension in Fig. 3.27).

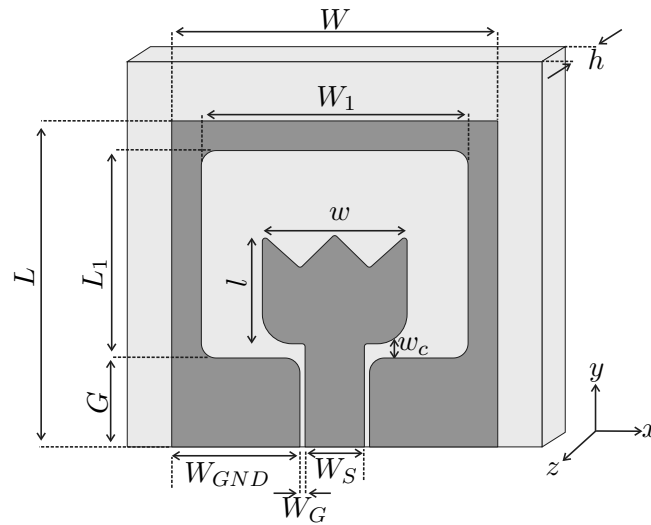


Figure 3.27: “Tulip” loop antenna.

After fixing this dimension, the next step is determining the dimensions of the stub, for obtaining wide bandwidth. In this respect, experience demonstrated that the stub length l and the gap w_c influence the impedance

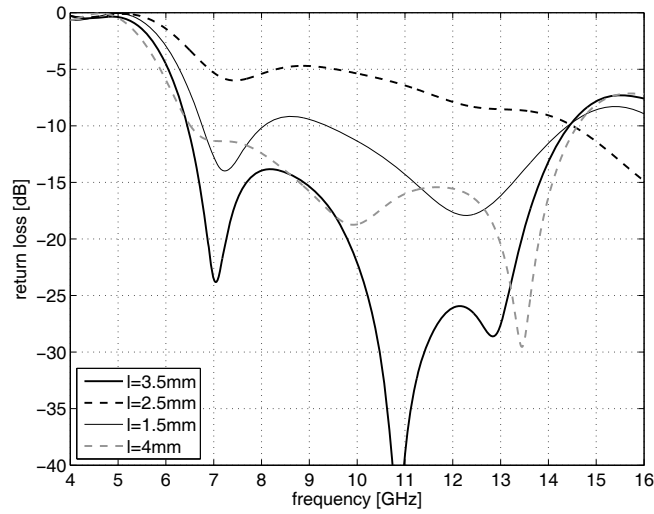
in both the lower and the higher segments of the frequency band, knowing that the length l being related to the added antenna inductivity while w_c being related to its capacitance. The effect of these parameters on the return loss is depicted in Fig. 3.28². Investigating these curves in detail yielded a combination $l = 3.5$ mm and $w_c = 0.5$ mm for providing the best performance in terms of return loss. Additionally, it was observed that selecting a ratio $L_1/l = 2.6$ results in an optimal matching of the antenna. The remaining antenna dimensions are indicated in Table 3.2.

Table 3.2: Geometric parameters of the ‘‘Tulip’’ loop antenna.

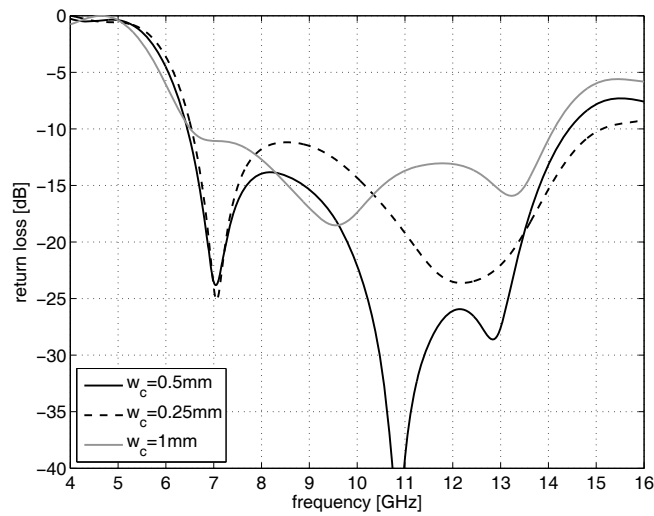
Parameter	Dimension[mm]	Description (see Fig. 3.27)
L	11	Length of the antenna
L_1	7	Length of the loop
w	4.9	Width of the tuning stub
l	3.5	Length of the tuning stub
w_c	0.5	Length of the gap
W	11	Outer width of the loop
W_1	9	Width of the loop
W_S	2	Width of the signal line
W_G	0.175	Width of the CPW’s gap
W_{GND}	4.325	Width of the ground
G	4	Length of the ground
h	0.812	Height of the substrate

The surface current distribution on the antenna at 8.5 GHz is depicted in Fig. 3.29. These currents are partly distributed around the neck of the tuning stub and partly along the loop section of the antenna. The magnitude of the currents decrease when going to the top of the loop and they become zero at the mid point of the upper part of the loop, in a manner that is

²The studies are conducted using the finite-integration, time-domain package CST Microwave Studio [26].



a



b

Figure 3.28: Return loss variation with respect to (a) Length of the tuning stub (l); (b) Length of the gap (w_c).

similar to the case discussed in Section 3.2.3. The vertical components of this current are the main contributors to the radiation while the horizontal components contribute to the cross polarization. As explained in Section 3.3, UWB, CPW fed printed antennas, like the “Tulip” loop antenna, support traveling wave characteristics. There are also multiple resonances in the return loss curve of the antenna the collective effect of which results in the UWB behaviour of the device.

The fabricated antenna is illustrated in Fig. 3.30. A semi-rigid cable

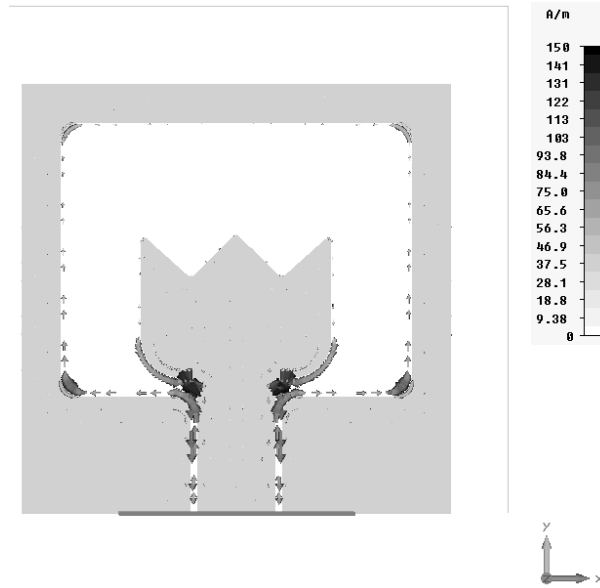


Figure 3.29: Surface current distribution of the loop antenna at 8.5 GHz.

is connected to the antenna in order to solder the connector away from the antenna itself. The simulated and measured magnitudes of the reflection coefficient of this antenna are presented in Fig. 3.31. The measured result indicates an operational bandwidth for a $VSWR \leq 2$ of 68%, stretching between 6.9 GHz and 14.1 GHz. The discrepancy between the simulated and the measured results is due to the close proximity of the soldering part to the feeding section of the antenna.

3.4.2 Modified loop antenna

In order to keep the soldering part away from the feeding section, the feed section of the antenna was extended by 30 mm. The fabricated, modified antenna is depicted in Fig. 3.32. Note that a similar engineering artifice, i.e. extending the feed section, was also used in Paragraph 3.2.3. In that case, since the radiation originates primarily from the transition region of the antenna, the feeding line extension had no significant impact on the impedance matching and radiation characteristics. Nevertheless the antenna depicted in Fig. 3.27 radiates primarily from the loop enclosing the tuning stub and, thus, extending the CPW line, and implicitly the effective length of this loop, does change the radiating impedance and, of course, its matching to the feeding part. Consequently, the l dimension was modified from 3.5 mm

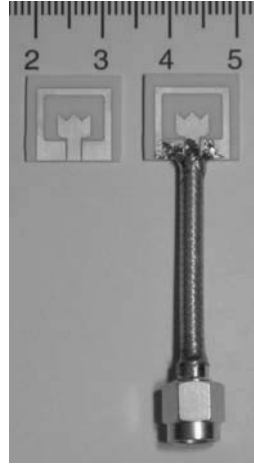


Figure 3.30: Fabricated loop antenna. Left- the photo- etched microwave laminate; right- antenna with the attached SMA connector.

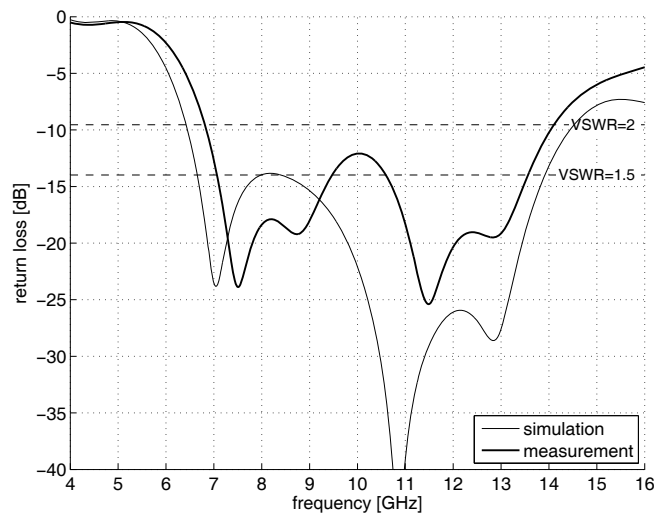


Figure 3.31: Simulated and measured return loss concerning the “Tulip” loop antenna.

to 2.5 mm and the protrusions of the tuning stub were removed. The magnitude of the reflection coefficient of this antenna is presented in Fig. 3.33. The measured result indicates an operational bandwidth for a $VSWR \leq 2$ of 70% stretching between 7.26 GHz and 15.04 GHz. The reflection coefficient, depicted in Fig. 3.33, was measured via a time-domain de-embedding technique for suppressing the extraneous effects of the SMA to CPW waveguide

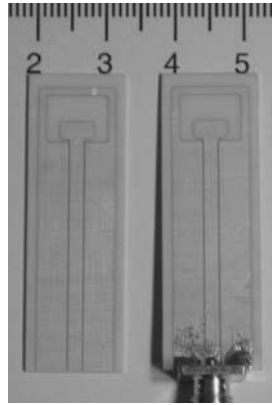


Figure 3.32: Fabricated modified loop antenna.

transition and of the soldering. Figure 3.33 shows a better agreement between the measured and simulated results. Although there is a relatively better agreement, the first resonance, which is around 8.5 GHz in the simulation, does not match very well the measured one. This is due to the TEM mode supported by the coaxial connector, which needs some time (i.e. some distance) for being converted into the quasi-TEM mode supported by the CPW line. Thus, as the frequency increases, a better match of the resonant frequency is observed.

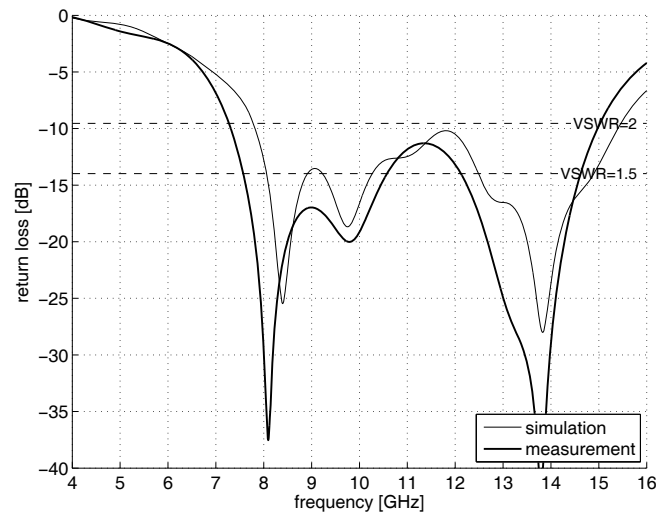
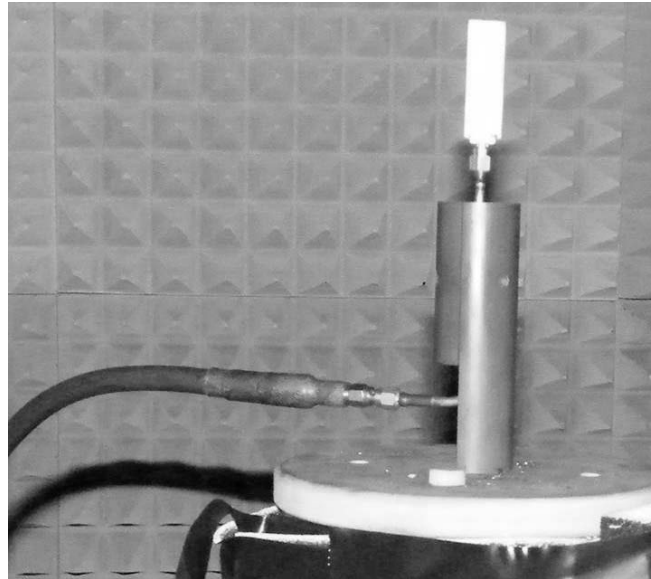


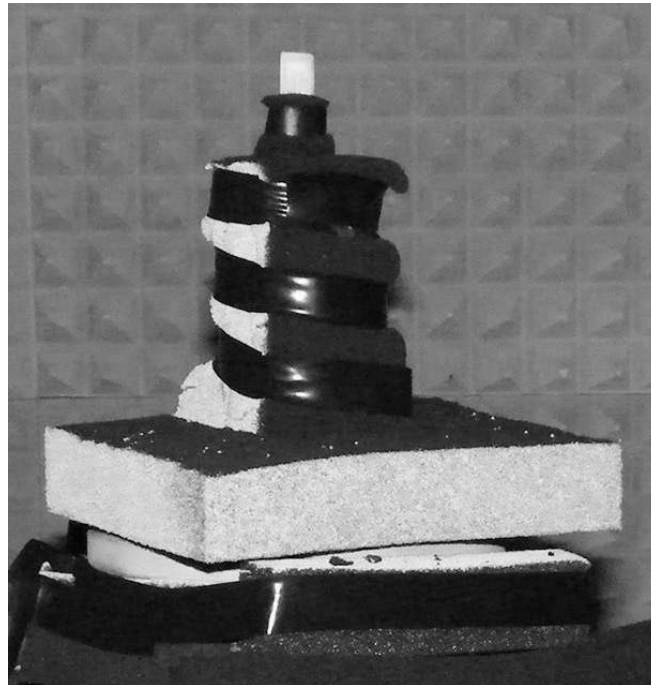
Figure 3.33: Simulated and measured return loss concerning the modified loop antenna.

Radiation pattern investigations

In this paragraph the radiation patterns for the following cuts are investigated: $\phi = 0^\circ$ (the xOz – plane in Fig. 3.27), $\phi = 90^\circ$ (the yOz – plane) and $\theta = 85^\circ$ (very close to the xOy – plane). With reference to Fig. 3.27, the elevation angle θ measures the tilting with respect to the Oz – axis while the azimuth angle ϕ measures the trigonometric rotation with respect to the Ox – axis. Just as in Paragraph 3.2.3, in order to prevent the spurious radiation from the extended CPW feeding line and the SMA connectors, these sections were covered with the Emerson & Cuming Microwave Products, Eccosorb HR absorber as shown in Fig. 3.34(b). The radiation patterns at three different cuts and at two different frequencies (i.e. 8.5 GHz and 12 GHz) are depicted in Fig. 3.35 and Fig. 3.36 respectively.



a



b

Figure 3.34: Modified "Tulip" loop antenna under test (a) Exposed; (b) Covered with absorbers.

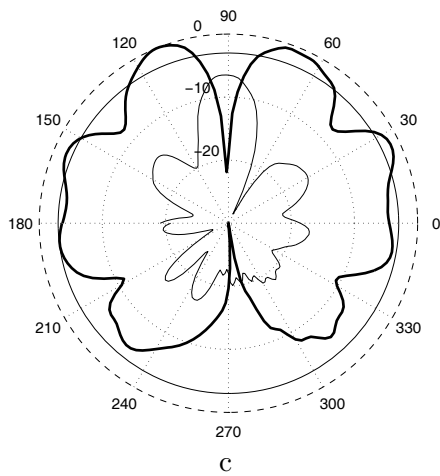
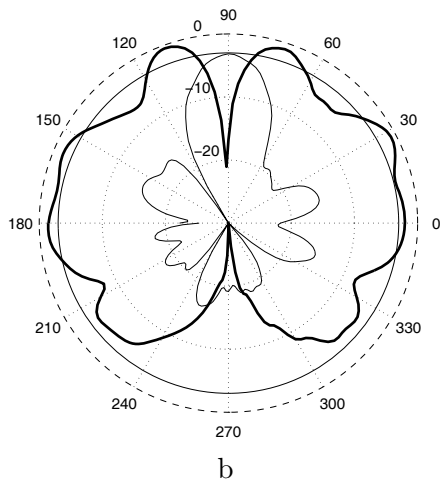
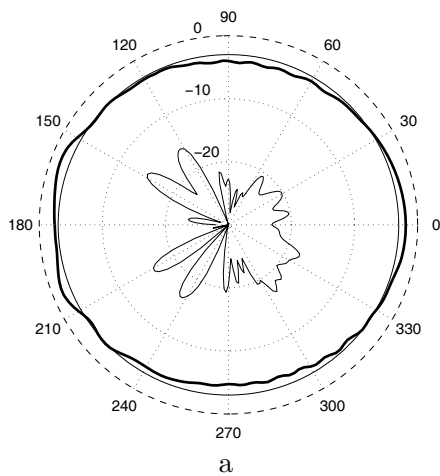


Figure 3.35: Normalized measured radiation patterns (in decibels) at 8.5 GHz: thick line – co-polar component; thin line – cross polar component. (a) $\{\phi = 0^\circ; \phi = 180^\circ\}$ cut; (b) $\{\phi = 90^\circ; \phi = 270^\circ\}$ cut; (c) $\theta = 85^\circ$ cut.

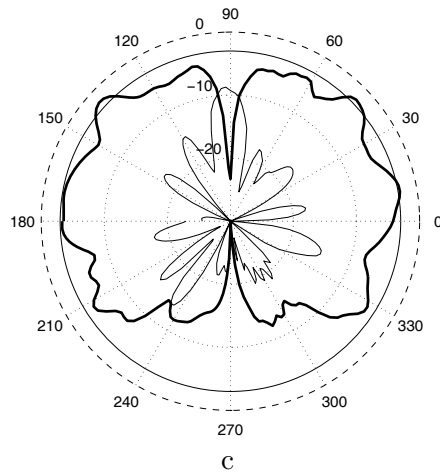
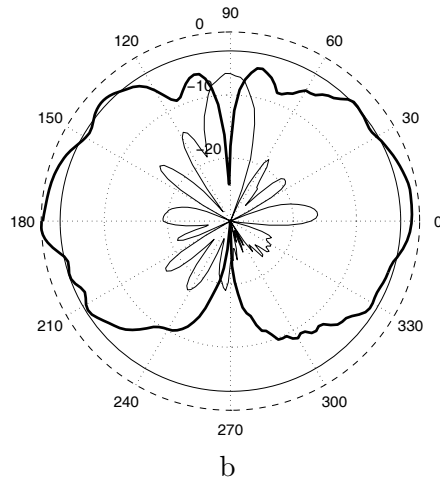
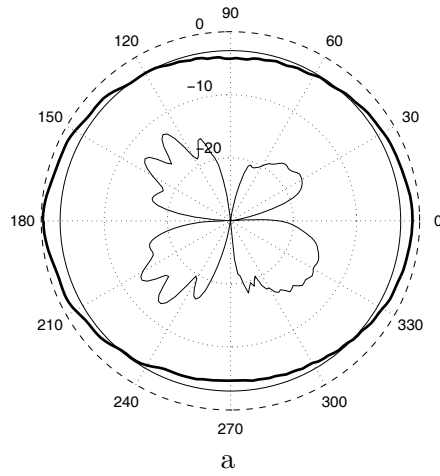


Figure 3.36: Normalized measured radiation patterns (in decibels) at 12 GHz: thick line – co-polar component; thin line – cross polar component. (a) $\{\phi = 0^\circ; \phi = 180^\circ\}$ cut; (b) $\{\phi = 90^\circ; \phi = 270^\circ\}$ cut; (c) $\theta = 85^\circ$ cut.

For effectuating the actual measurements reported in Figs. 3.35 (a) and 3.36 (a) the antenna was mounted on the turntable in an upright position and an (almost) omnidirectional radiation patterns could be observed. The small deviations must be attributed to the measurement cable winding around the turntable; this may result in marginal alterations of the matching conditions in the measurement set-up. These abnormalities are more visible in the cross-polar behavior (see Fig. 3.35 (a), the thin line plot).

The measurements reported in Fig. 3.35 (b) and 3.36 (b) were carried out with the antenna being mounted parallel to the turntable, with the antenna pointing towards the standard-gain horn source for $\theta = 90^\circ$. Consequently, in the diametrically opposite orientation, namely at $\theta = 270^\circ$, the antenna is obscured by the comparatively large SMA connector and the enclosing absorber. This effect is clearly noticeable in the relevant radiation patterns that present high attenuations for large intervals enclosing $\theta = 270^\circ$. Moreover, a similar effect manifests itself in Fig. 3.35 (c) and in Fig. 3.36 (c), this time for around $\phi = 270^\circ$.

In order to facilitate comparisons, the radiation patterns were normalized, per frequency, to the same maximum value. The radiation patterns in Figs. 3.35 (a-b) and Figs. 3.36 (a-b) do satisfy the condition of sharing identical radiation levels at identical directions, except for the case in Figs. 3.35 (a-b) where a small discrepancy of about 1.5 dB is noticed at $\theta = 180^\circ$. This dissimilarity can be explained by small alignment errors and/or differences in the calibration of the measurement set-up. Summarizing, it can be affirmed that the investigated antenna has favorable radiation properties that are, moreover, stable over the whole frequency band of interest.

The impact of the feed section on the radiation characteristics

Since the loop antenna radiates primarily from *grounded* the loop enclosing the tuning stub, extending the CPW lines increases the effective length of the antenna. Consequently, unlike in the case of the “Eared” antenna, the feed section *does* intervene in the electrical properties of the “loop” antenna, its effect being visible in both the impedance matching characteristic and the radiation pattern. To substantiate this, the measurements reported in Section 3.4.2 were repeated after removing the absorbing shield from the feed line. The effect of the feed radiation can be seen in Fig. 3.37. Note that in real applications the feed line can be much shorter, thus, its impact on the overall radiation pattern is much lower.

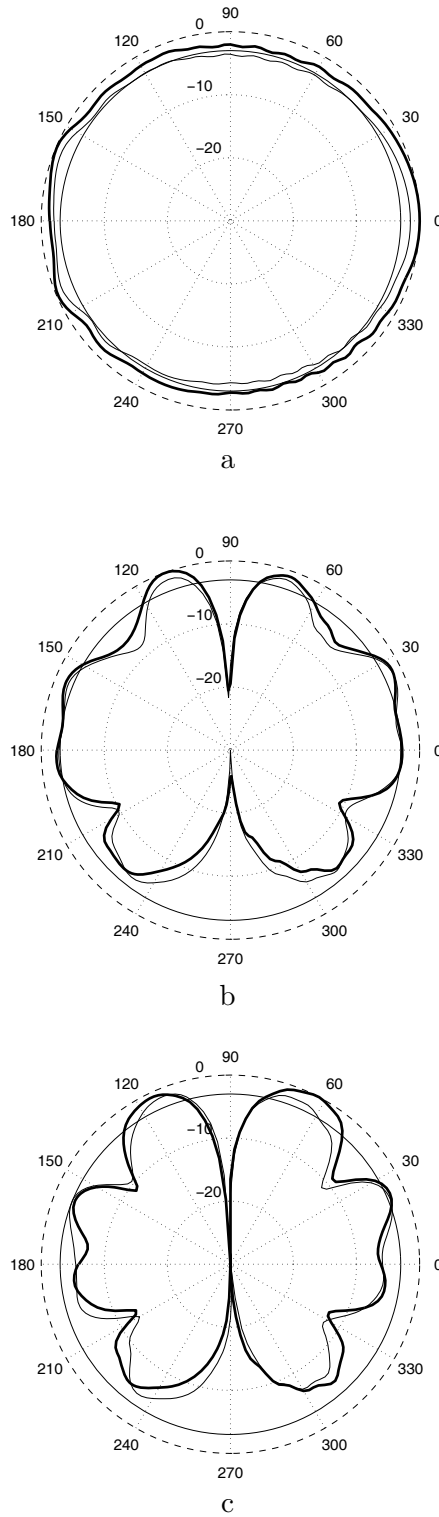


Figure 3.37: Comparison between the normalized radiation patterns (in decibels) at 8 GHz corresponding to the (a) $\{\phi = 0^\circ; \phi = 180^\circ\}$ cut; (b) $\{\phi = 90^\circ; \phi = 270^\circ\}$ cut; (c) $\theta = 85^\circ$ cuts, for 8 GHz: thick line – co-polar component, without the absorber shield; thin line – co-polar component, with the absorber shield.

3.5 Conclusions

Two types of new antennas, namely the “Eared” and the “Tulip” loop antennas have been investigated. A systematic approach for designing the “Eared” antenna which has a relative bandwidth of more than 150% is described; to the author’s knowledge this antenna has the widest impedance bandwidth with this electrically small size compared to other printed and low-profile antennas described in literature. All predicted performances of the antennas are confirmed by measurements. A systematic way of designing the “Tulip” loop antenna was also discussed. This antenna has an impedance bandwidth of more than 70% and to the author’s knowledge this antenna is the smallest and simplest antenna compared to other printed loop antennas discussed in the literature. Similarly to the “Eared” antenna, all simulated results of the antenna are also verified by measurements.

Elements of novelty

The primary novelties presented in this chapter are listed as follows:

- The design of an UWB antenna which has a relative bandwidth of more than 150% is introduced. To the author’s knowledge this antenna has the widest impedance bandwidth compared to other printed and low-profile antennas described in literature.

This antenna element has inherently low mutual coupling interactions with neighboring elements in an array environments due to the feeding line design and the confined electric field lines around the transmission region of the antenna (Chapter 5).

- The design of a printed loop antenna which has an impedance bandwidth of 70% is introduced. To the author’s knowledge this antenna has the smallest electrical size for the mentioned impedance bandwidth compared to other printed and low-profile radiators found in literature.

Chapter 4

Design of an Artificial Magnetic Conductor

The radiators studied in Chapter 3 have all bi-directional radiation patterns¹. Since some applications require uni-directional radiation patterns², this chapter explores the ways of converting the bi-directional radiation patterns into uni-directional ones by using Artificial Magnetic Conductors (AMC). The isolation of the antenna is also important when it is placed in the vicinity of a conductive medium, such as an aeroplane fuselage, a car chassis or biological structures, in UWB communication applications. The AMC plane changes the type of the interaction between the antenna and the conducting surface on which the antenna is mounted. The chapter starts by examining a standard implementation of an AMC, using a uniform lattice. The use of this type of AMC, in conjunction with the previously examined “Tulip” loop antenna (see Section 3.4), will be shown to be sub-optimal. The solution to these limitation will be found by resorting to non-standard, a-periodic AMC structures. This chapter will be finalized by drawing some conclusions together with cataloging the novelties presented in it.

4.1 High impedance electromagnetic surfaces— standard approach

High impedance electromagnetic surfaces, also known as 2-D photonic band gap (PBG) materials, exhibit attractive properties for many applications.

¹Bidirectional antennas radiate or receive efficiently in only two directions.

²Unidirectional antennas radiate or receive efficiently in only one direction.

These surfaces behave as perfect magnetic conductors (PMC) (with respect to a plane wave with normal incidence) within a limited frequency band gap [85]. Obtaining high impedance surface properties is intrinsically associated with periodic structures and corrugated surfaces, under the provision that the hereby considered corrugated surfaces, unlike the traditional ones, are much thinner than the operating wavelength, this making them low-profile [80].

PMCs can be used as back planes in low profile antenna configurations in order to direct the radiation in one direction. Conventional reflecting planes reflect the waves with a phase reversal of 180° . For the printed antennas, generally, the electrical height of the radiating element should be about $\lambda/4$ above the ground plane in order to obtain good unidirectional patterns at the desired frequency. For heights different than $\lambda/4$, the pattern starts splitting at the bore-sight due to wave cancellation, an effect that can be explained by resorting to the image theory. A first advantage of using high impedance electromagnetic surfaces comes from this point. A very thin layer of densely packed 2-D periodic structures on top of a surface shields the ground plane from inducing an image current to cancel the propagating E-field [60]. The surface reflects the waves in-phase, rather than out-of-phase as a normal metallic surface does. In other words, the image currents results in constructive, rather than destructive interference, allowing the antenna to radiate more efficiently. Therefore antenna elements can be placed closer to the ground plane which allows compact antenna designs where the radiating elements are confined to limited spaces. Assuming no losses and exactly 0° of reflection phase, the surface is referred to as a PMC, which is complementary to a Perfect Electric Conductor (PEC). In practice, the reflection phase of Artificial Magnetic Conductors (AMCs) crosses zero at one frequency, only. The useful bandwidth of an AMC is in general defined at each side of the central frequency, since limited phase shifts would not cause destructive interference between direct and reflected waves [32].

In reality, the reflecting plane is always finite and its edges contribute to the radiation pattern. The antenna generates surface currents and when they radiate from the edges and the corners, they cause multipath interference [82]. Unlike the standard conductors, the metallic electromagnetic structures characterized by a high surface impedance suppresses the propagation of surface waves [8]. This property is important because the radiating elements are isolated in this way from the nearby conductive media (such as the biological structures). Thus, smoother radiation patterns can be achieved than with the same antenna on a conventional radiating plane.

Despite these advantages, the high impedance surfaces suffer from a

limited bandwidth. For example, the bandwidth reported in [8] was 8.11% only. In addition to the limited bandwidth, the production of these structures is difficult and costly.

The account now proceeds by examining some general results concerning high impedance surfaces.

4.1.1 Theoretical background

Many properties of high impedance surfaces can be explained by invoking an *effective medium model*. The structure is assigned a surface impedance equal to that of a parallel LC circuit. The use of lumped parameters to describe the electromagnetic structures is valid when the wavelength is much longer than the size of the individual features [82].

The properties of high impedance electromagnetic surfaces are similar to those of corrugated slabs. The quarter-wavelength slots have simply been folded up into lumped elements, capacitors and inductors, and distributed in two dimensional arrays. The two dimensional array of resonant elements can be viewed as a kind of filter.

A typical implementation of a high impedance surface is represented in Fig. 4.1. The surface consists of an array of metal protrusions connected to the metal base by means of metallic via posts. A voltage applied parallel to the surface causes charges to build up at the ends of the top metal plates which can be described as capacitors. As the charges slosh back and forth, in response to a radio-frequency field, they flow around a long path through the vias and the bottom metal surface. These currents are associated with a magnetic field and, thus, with an inductance [8], [82]. The proximity of the neighboring metal elements provides the capacitance and the conducting path linking them together provides the inductance. They behave as parallel resonant LC circuits. The impedance of the circuit can be calculated through the following equation:

$$Z = \frac{jwL}{1 - w^2LC} \quad (4.1)$$

where:

- $j = \sqrt{-1}$;
- $w = 2\pi f$ is the angular frequency;

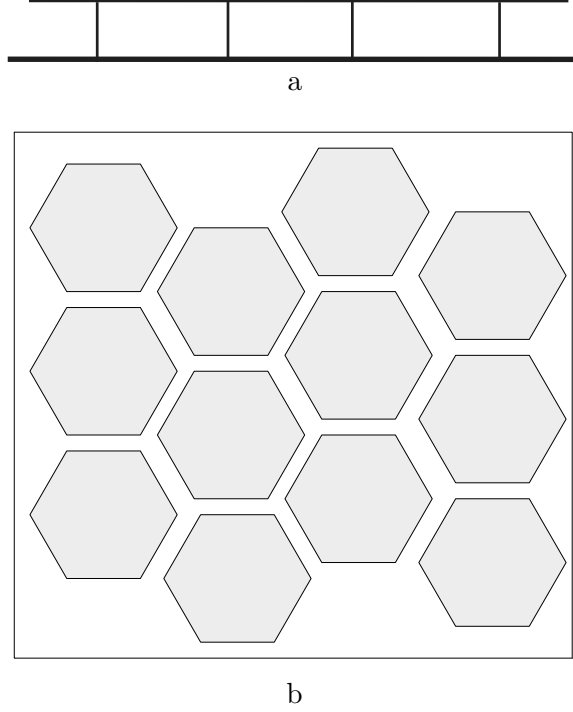


Figure 4.1: High impedance surface. (a) Side view; (b) top view [81].

- L and C are the capacitance and the inductance in the equivalent circuit model.

In Eq. (4.1), it can be seen that the structure exhibits a high surface impedance in a narrow band around the LC resonance. The resonant frequency of $w_0 = 2\pi f_0 = 1/\sqrt{LC}$ is the center of the band. The high-impedance bandwidth Δw is obtained by the evaluating following equation [8].

$$\frac{\Delta w}{w_0} = \frac{\sqrt{L/C}}{\eta_0} \quad (4.2)$$

where $\eta_0 \approx 120\pi$ (Ω) is the free space impedance [73, p. 16]. Using the definition of w_0 in Eq. (4.2), Δw can be obtained as

$$\Delta w = \frac{1}{C\eta_0} \quad (4.3)$$

The capacitance in this model comes from the fringing electric field

between the adjacent metal planes and the inductance is determined by the thickness of the substrate and the magnetic permeability. Using Eqs. (4.1) and (4.2), the lower and the upper frequency ends of the frequency band can be found.

In the literature, the interactions of AMC surfaces with planar antennas have been widely investigated. As an example, the interaction of such a surface with a patch antenna is studied in detail in [105]. In this chapter, the interaction of an AMC surface with a wide-bandwidth quasi-magnetic antenna will be investigated. Metallic patches printed on a grounded dielectric substrate and connected to the ground through vias have been presented as AMCs in some manuscripts [21, 80, 81]. AMC surfaces have also been produced from similar structures in the absence of vias, which eases the fabrication process [32]. In this chapter an AMC surface composed of metallic patches in the absence of vias will be explored.

4.1.2 Design procedure

In the design of AMC ground planes, the phase curve of the reflected field (of a plane wave) which is incident on the AMC surface is a very important parameter. In the case of the studies reported in this thesis, the phase curve of the field reflected from the AMC is computed by using the commercially available CST Microwave Studio software [26]. Since it is not possible to obtain the phase curves directly with CST, two different structures are excited with plane waves. Firstly, the AMC structure is excited with a plane wave and, from this experiment, the data for incident plus reflected waves from the AMC surface is obtained. Subsequently, the “air box” with the same dimensions as the AMC structure is excited and in this way the incident wave is found. After post processing of these data in MATLAB, the reflection coefficient for the reflected wave and its phase are found. Obtaining this phase curve helps the designer to realize the AMC condition at, or near, the desired frequency. At the desired frequency, the phase of the reflected wave should be close to 0° .

The initially considered AMC is depicted in Fig. 4.2. It consists of a perfect PEC at the back side, a dielectric material of RT/duroid 5870 with a relative permittivity $\epsilon_r = 2.33$ in between and square PEC patches at the upper surface. The height of the substrate is 3.175 mm. On the dielectric substrate, there are 4×4 square patches with edge lengths of 7.48 mm and the gap between the patches of 1.245 mm. When this structure is excited with a plane wave, the reflected wave phase curve depicted in Fig. 4.3 is obtained [91].

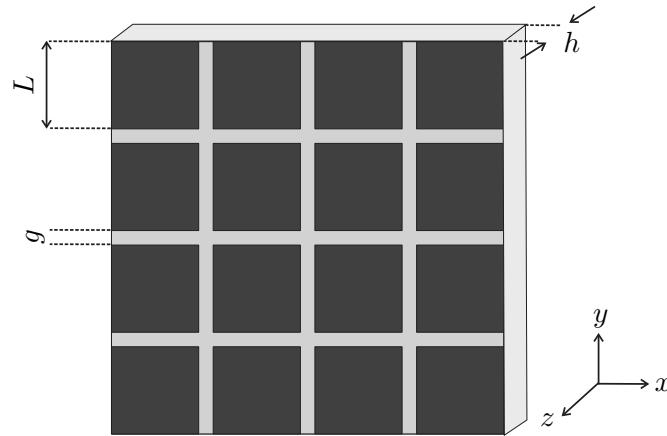


Figure 4.2: 4 by 4 Artificial Magnetic Conductor.

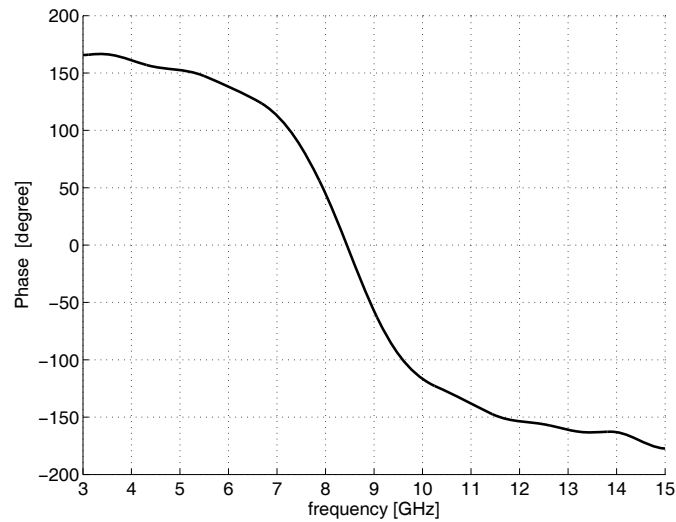


Figure 4.3: The phase of the reflected field from the AMC surface depicted in Fig. 4.2.

It has been stated that, for the AMC to work efficiently, the phase of the reflected wave should be close to 0° at the desired frequency.

4.1.3 Integration of the “Tulip” loop antenna and standard AMC structures

Once the AMC dimensions are fixed, the interaction of the surface presented in Fig. 4.2 with the “Tulip” loop antenna (Section 3.4) is investigated. The “Tulip” loop antenna is placed on the AMC as seen in Fig. 4.4 and the performance of the whole structure is examined. The antenna is etched on the same material (RT/duroid 5870) that was used in the design of the AMC. The height of the substrate of the antenna is 3.175 mm, as well. The bandwidth of the whole structure depends on the curve depicted in Fig. 4.3. In the literature, it was stated that the frequency range corresponding to either $\pm 90^\circ$ or $\pm 45^\circ$ regions [103] can be considered as the effective bandwidth of the antenna and AMC structure, depending on the performance of the antenna.

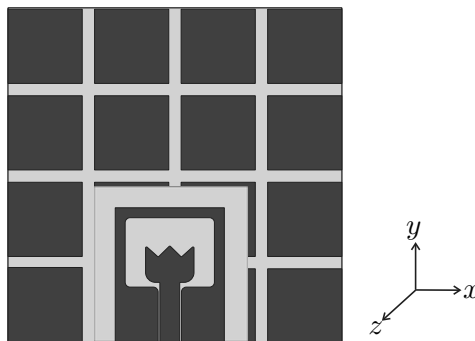


Figure 4.4: The “Tulip” loop antenna on a 4×4 AMC structure.

Impedance bandwidth analysis

The antenna plus the AMC structure depicted in Fig. 4.4 are simulated and a $VSWR \leq 2$ impedance bandwidth of 44%, extending from 7.5 GHz to 11.5 GHz, is achieved, the relevant frequency characteristic being depicted in Fig. 4.5.

Radiation pattern analysis

Although the result for the reflection coefficient magnitude seems satisfactory, a split in the radiation patterns is observed as the frequency increases. This is due to the phase difference between the currents induced in adjacent

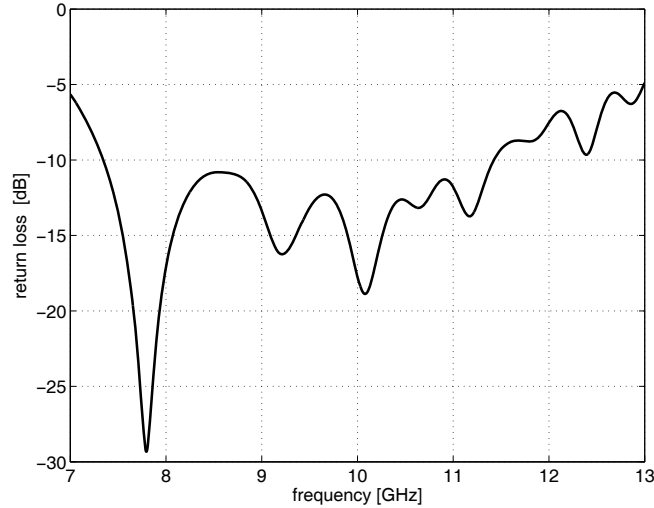


Figure 4.5: Simulated return loss concerning the “Tulip” loop antenna and AMC plane.

patches, these currents adding up destructively at broadside. Typical examples of this pattern splitting are depicted in Fig. 4.6 (a), (b) at 8 GHz and 10 GHz, respectively. These figures contain the yOz – plane of the antenna when ϕ is kept constant at 90° , θ is variable and the coordinate system of Fig. 4.4 is used. In Fig. 4.6 (a), (b), $\theta = 0^\circ$ corresponds to the broadside direction of the antenna. A deep notch, at a level below -20 dB, is clearly visible in both plots. The radiation patterns at the $\phi = 0^\circ$ plane can be seen in Fig. 4.7 (a), (b) at 8 GHz and 10 GHz, respectively. In order to facilitate comparisons, the radiation patterns were normalized, per frequency, to the same maximum value. Thus the radiation patterns in Fig 4.6 (a) and Fig. 4.7 (a) display the same value (around -10 dB) at $\theta = 0^\circ$, which is the broadside direction of the antenna. This is also valid for the radiation patterns in Fig 4.6(b) and Fig. 4.7 (b), in which the patterns are at approximately -17 dB in the broadside direction, at 10 GHz [91].

To overcome the pattern splitting problem, the AMC structure has been reshaped as a rectangle, as suggested in [67], [68]. Since the antenna is located in the xOy – plane and the current is mainly flowing along the y direction, the four patches on the right side of the antenna and the other four patches on the left side of the antenna are eliminated. This is also beneficial in order to reduce the overall size of the structure. This structure exhibits a bandwidth from 8.9 GHz to 11.5 GHz, indicating a noticeable impedance bandwidth reduction when compared with the previous example. The radiation patterns are better, as compared to the Fig. 4.6 (a), (b) cases, but they

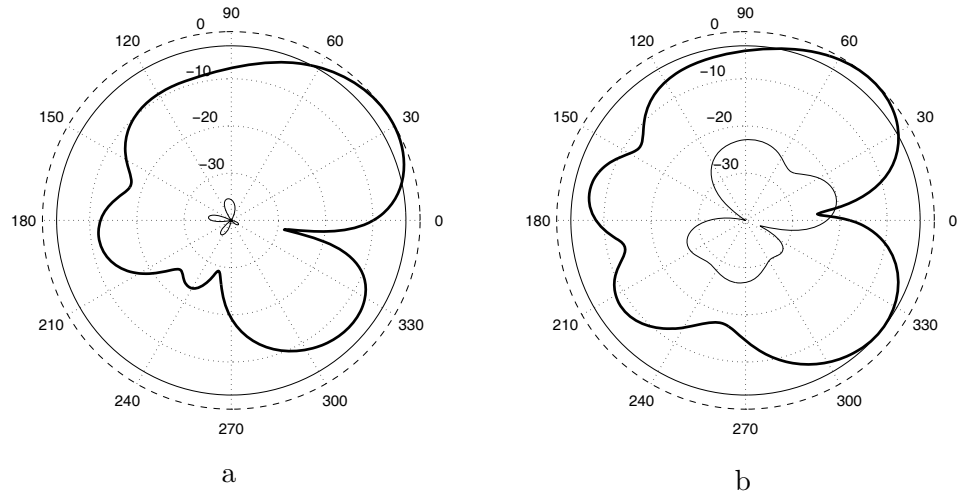


Figure 4.6: Radiation patterns for the “Tulip” loop antenna plus the AMC structure at the $\phi = 90^\circ$ cut at (a) 8 GHz, (b) 10 GHz: thick line – co-polar component; thin line – cross polar component.

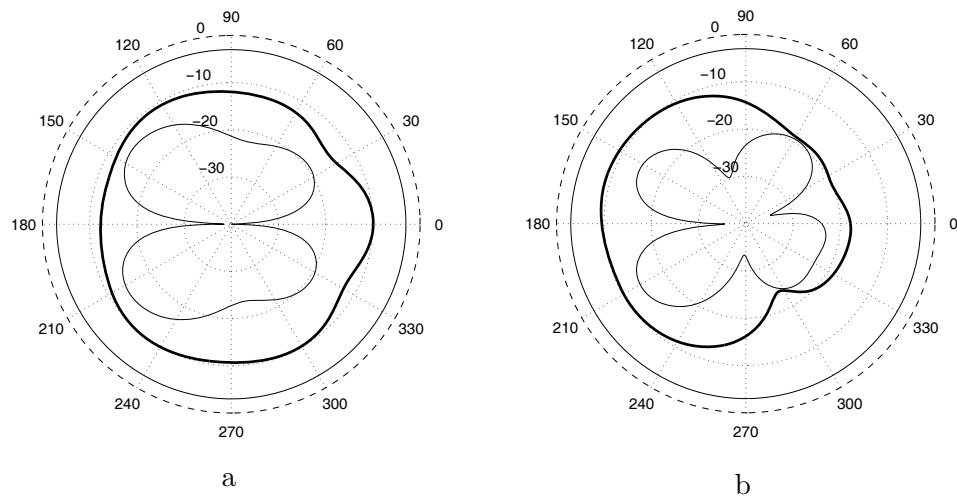


Figure 4.7: Radiation patterns at the $\phi = 0^\circ$ cut at (a) 8 GHz, (b) 10 GHz: thick line – co-polar component; thin line – cross polar component.

still leave space for improvement; i.e. the level of the notch at the $\phi = 90^\circ$ cut is at a level of approximately -13 dB at 10 GHz in the current case.

4.2 Non-standard, a-periodic AMC structure

As explained in Paragraph 4.1.3, although the impedance bandwidth of the “Tulip” loop antenna with the standard AMC is satisfactory, the radiation patterns need to be improved. For achieving this the idea was born to break the periodicity (without removing any patch) in the y direction, which may lead to further improvements. Making the AMC structure *a-periodic* as in [67], [68] reduces the phase difference between the successive patches which causes the pattern splitting in the broadside direction.

4.2.1 Integration of the “Tulip” loop antenna and non-standard AMC structures

The antenna, together with the a-periodic AMC surface, is depicted in Fig. 4.8. The main difference compared to [67], [68] is that the structure is of *quasi-magnetic* type, which is more easy to feed, contrary to the idealized balanced excitation considered in the simulations in [67] and in [68].

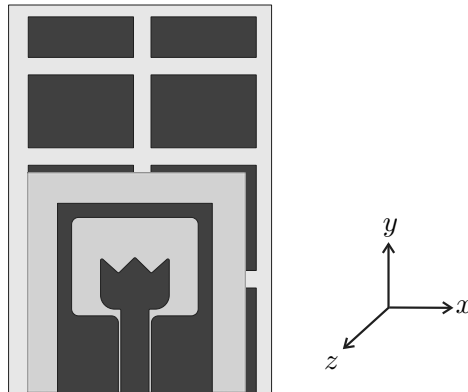


Figure 4.8: Configuration of the antenna together with the a-periodic AMC structure and coordinate system.

Design choices

The edge lengths of the lowermost two rows of patches are 7.48 mm, as stated before. The heights of the third and fourth rows are recursively shortened by 2.7 mm, while their width is kept constant. The spacing between the patches (1.245 mm) is kept the same as in the previous cases. Note that the patch height reduction results in a significant reduction of the overall size of the structure [91].

Impedance bandwidth analysis

With these choices, an impedance bandwidth, for a $VSWR \leq 2$, from 7.5 GHz up to 11.5 GHz is obtained. The return loss of the antenna mounted on the a-periodic AMC is depicted in Fig. 4.9. An impedance bandwidth of 44% is preserved as in the periodic AMC case.

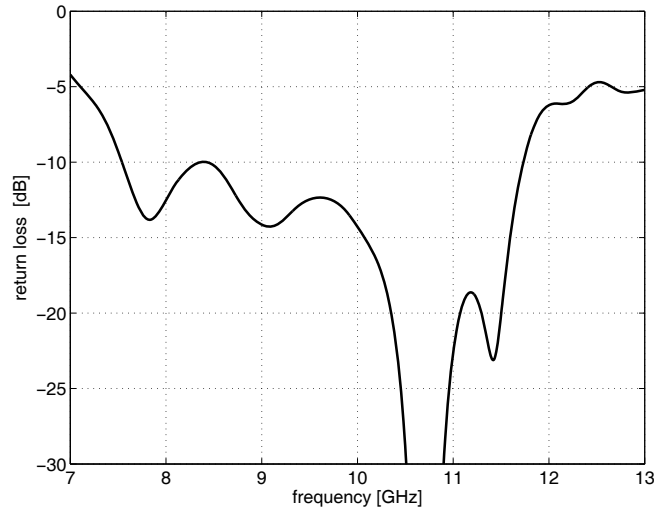


Figure 4.9: Simulated return loss concerning the antenna and the a-periodic AMC plane.

Radiation pattern analysis

More importantly, the radiation patterns are better compared to the 4×4 periodic case, i.e. the maximum near broadside is restored. These modified radiation patterns are depicted in Fig. 4.10 (a),(b) and Fig. 4.11 (a),(b). Although the maximum is restored near broadside at 8 GHz in Fig. 4.10 (a), as the frequency increases a split appears in the broadside direction due to the destructive effects of the currents at $\theta = 0^\circ$. It should be noted that the level of the trough at the broadside has improved from -23 dB for the rectangular AMC configuration to -6.5 dB for the a-periodic AMC case. Another observation is that due to the small size of the AMC, the front-to-back ratio is not satisfactory (i.e. 7.5 dB at 8 GHz), thus, for the sake of completeness, the size of the back plane is increased in order to confirm that the front to back ratio is also increased.

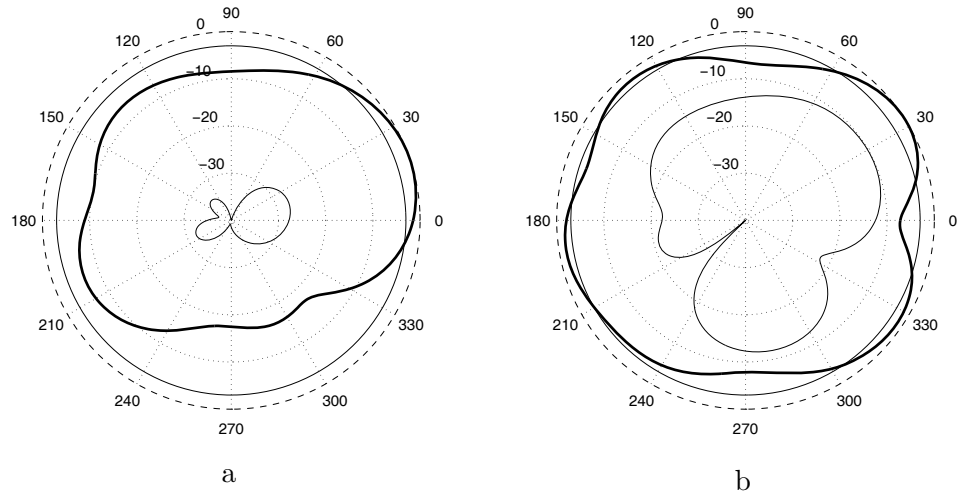


Figure 4.10: Modified normalized radiation patterns at the $\phi = 90^\circ$ cut at (a)8 GHz, (b)10 GHz: (for a-periodic AMC surface): thick line – co-polar component; thin line – cross polar component.

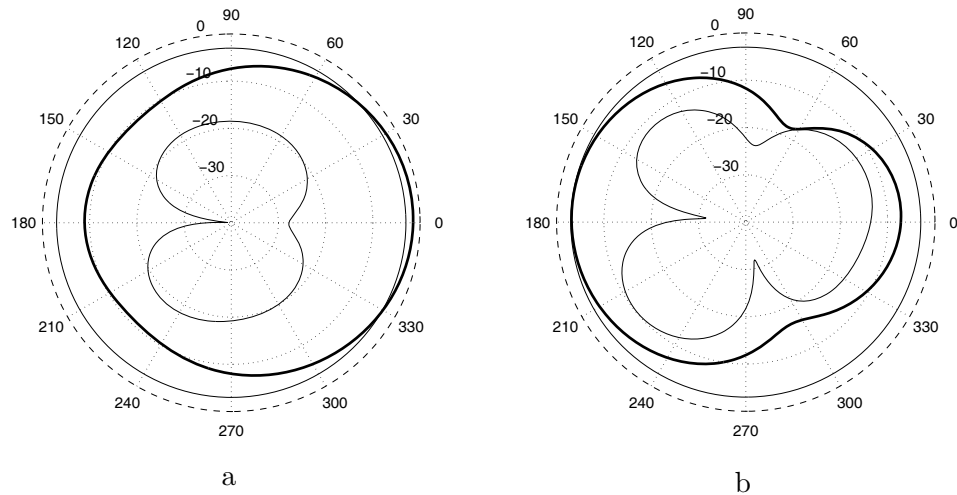


Figure 4.11: Modified normalized radiation patterns at the $\phi = 0^\circ$ cut at (a)8 GHz, (b)10 GHz: thick line – co-polar component; thin line – cross polar component.

4.2.2 The effect of extending the size of a-periodic AMC structures

As discussed in Section 4.2.1, the size of the ground plane is increased in order to improve the front-to-back ratio of the antenna. A ground plane is placed

under and around the antenna such that the antenna “sees” approximately a 2λ ground plane on each side of the antenna at 8 GHz.

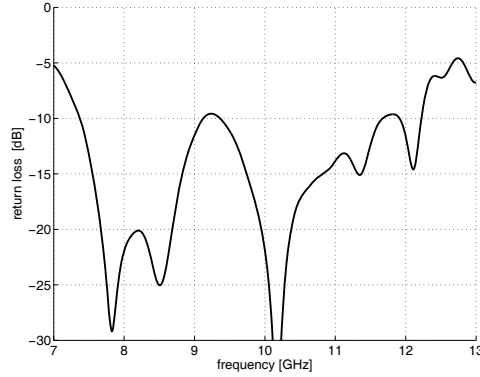


Figure 4.12: Simulated return loss concerning the “Tulip” loop antenna and AMC plane on a large ground plane.

The simulated reflection coefficient magnitude of the final configuration is presented in Fig. 4.12. The simulated result indicates an operational bandwidth for a VSWR ≤ 2 of 51.5%, stretching between 7.2 GHz and 12.2 GHz.

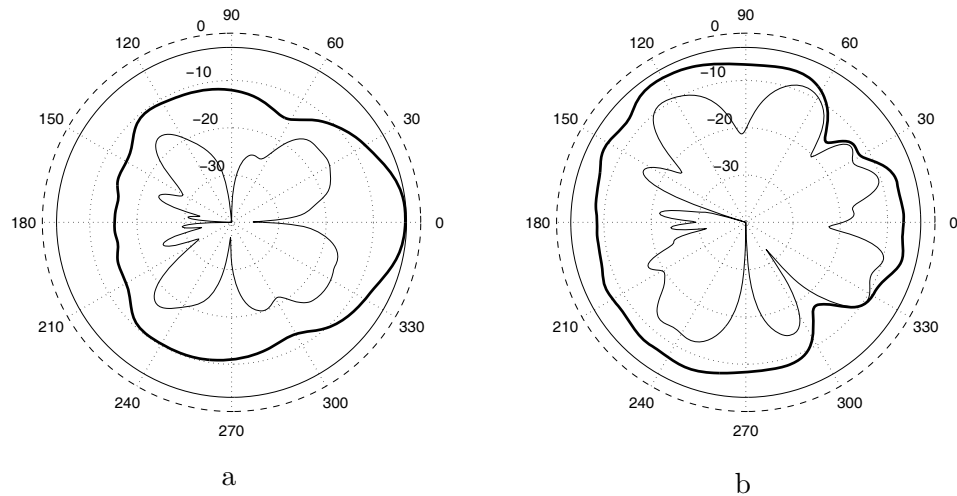


Figure 4.13: Modified normalized radiation patterns on a larger ground plane at the $\phi = 0^\circ$ cut at (a) 8 GHz, (b) 10 GHz: thick line – co-polar component; thin line – cross polar component.

The $\phi = 0^\circ$ cut radiation patterns are depicted in Fig. 4.13 (a) and (b) at 8 GHz and 10 GHz respectively. The front to back ratio is increased to more

than 12 dB at 8 GHz. The corresponding radiation patterns at the $\phi = 90^\circ$ cut at 8 GHz and 10 GHz are depicted in Fig. 4.14(a) and (b). It can be concluded that as the size of the ground plane increases, better front-to-back ratios are observed as expected. Similar as performed for the radiation patterns depicted in Fig. 4.6(a)- Fig. 4.7(a) and Fig. 4.6(b)-Fig. 4.7(b), the radiation patterns presented in Fig. 4.13(a) Fig. 4.14(a) and Fig. 4.13(b) Fig. 4.14(b) were normalized, per frequency, to the same maximum value.

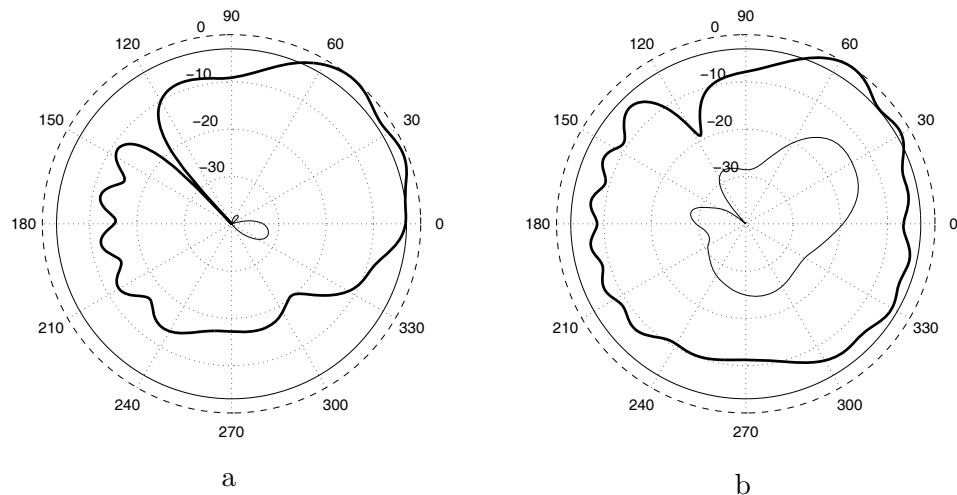


Figure 4.14: Final normalized radiation patterns on a larger ground plane at the $\phi = 90^\circ$ cut at (a) 8 GHz, (b) 10 GHz: (for a-periodic AMC surface): thick line – co-polar component; thin line – cross polar component.

4.3 Conclusions

This Chapter explores the use of Artificial Magnetic Conductors in order to convert the bi-directional radiation patterns of elementary radiators into uni-directional ones. The interaction of the “Tulip” loop antenna presented in Chapter 3 with the AMC is investigated. Since the periodic AMC results in pattern splitting problems in the broadside direction, this problem is solved by the a-periodic AMC design. The resulting antenna structure with the optimized AMC has an impedance bandwidth of 44%. The radiation patterns show smooth main lobe at broadside direction at low frequencies (i.e. at 7.5 GHz), however dips appear at the broadside direction gradually with the increase in frequency (i.e. after 10 GHz). Although the front-to-back ratio is poor, the radiation patterns show that the antenna can be

placed in the vicinity of a conductive media since the radiation patterns do not exhibit unwanted phenomena such as dips at the bore-sight. However the gain is still reduced due to the presence of the unavoidable back radiation.

Elements of novelty

The primary novelties presented in this chapter are listed as follows:

- The radiation pattern of the “Tulip” loop antenna is converted to a uni-directional one by a simple, low-cost, but successful design of an AMC.
- Although high impedance surfaces suffer from a limited impedance bandwidth, a quite satisfactory impedance bandwidth is obtained.

Chapter 5

Integration of the designed radiators in UWB array environments

In Chapter 3 two types of radiators, namely the “Eared” and the “Tulip” loop antennas, have been investigated in detail. Both type of elements are characterised by wide impedance bandwidths and stable radiation patterns, features that were demonstrated via numerical simulations and validated experimentally. Nevertheless, as stated in Chapter 1, the appropriate radiation properties that are manifest at element level may drop dramatically when antennas are embedded in array configurations. Moreover, the insufficiently small electrical size of these elements may cause the onset of grating lobes in array environments.

In line with the general requirements within the WiSE project (See Appendix A) the suitability of the radiators presented in Chapter 3 to integration in (linear) arrays needs now to be verified. To this end, a linear array consisting of “Tulip” loop antennas will be firstly investigated, the numerical experiments and physical measurements documenting an appropriate performance. Subsequently, a complex investigation of (large) linear arrays of “Eared” antennas will be effectuated, insisting on the attainable scanning capabilities. In this process, an efficient method for predicting the performance of large arrays will be presented.

5.1 Linear array consisting of “Tulip” loop elements

In Section 3.4, a CPW-fed, printed “Tulip” loop antenna was described and investigated in detail. The single antenna has a measured operational bandwidth for a VSWR ≤ 2 of 70%, stretching between 7.26 GHz and 15.04 GHz. By using these antennas, linear arrays are constructed in order to study the behaviour of the antennas in array structures. The linear array consisting of “Tulip” loop antennas is depicted in Fig. 5.1. It consists of 4 elements, the center-to-center spacing between two consecutive elements being $d_{\text{CTC}} = 11$ mm.

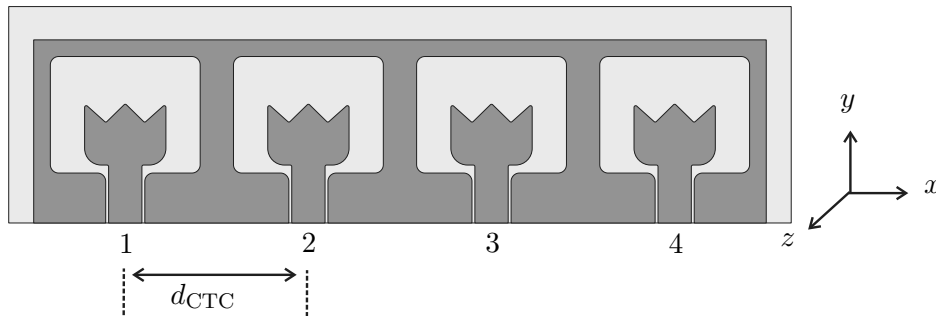


Figure 5.1: Linear array of four “Tulip” loop antennas with coordinate system.

5.1.1 Array architecture optimization

Scattering parameters numerical analysis

The frequency dependence of the reflection coefficient at the terminals of the array elements with all other elements being closed on matched loads will be investigated firstly for the array presented in Fig. 5.1. The return loss of the “Tulip” array from the first and the second ports of the array can be seen in Fig. 5.2. Since the array in Fig. 5.1 is symmetric with respect to its middle point, S_{11} is equal to S_{44} and similarly S_{22} to S_{33} in both magnitude and phase, this justifying the displaying of S_{11} and S_{22} in Fig. 5.2, only. It can be noticed that the antenna can not radiate properly from its second port below 11.5 GHz (see Fig. 5.2). Since the first element is not totally affected by the other elements in the array, it can be learned from Fig. 5.2 that, in terms of impedance bandwidth, S_{11} is sufficiently good. Thus, to be able to understand the behavior in array environments, an element which

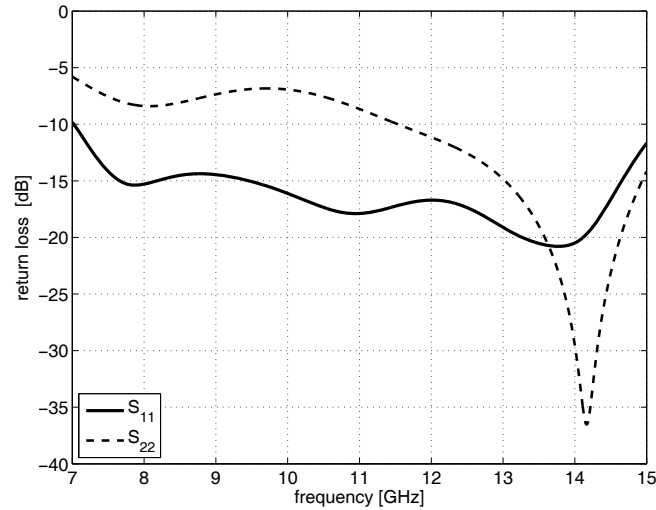


Figure 5.2: Return loss of the “Tulip” array, depicted in Fig. 5.1, from the first and second ports of the array with all other elements are loaded with matched loads.

is *significantly* affected by its inclusion in an array environment should be investigated, and this is the element 2 in the current case.

The second item to be examined is the coupling between the elements of the array. The initial investigations have shown a very high coupling, especially between the nearby elements, the frequency dependence of these couplings being presented in Fig. 5.3. Since there is a strong mutual coupling problem in the current configuration, the ways to reduce the mutual couplings need now to be addressed.

Mutual coupling mitigation

Once radiators are placed in array environments, their performance is affected by the mutual coupling that inherently manifests itself. This phenomenon was observed to have a detrimental effect on the antenna characteristics and, consequently, methods for efficiently mitigating it had to be identified for safeguarding the favorable radiation properties of the isolated antenna.

To this end, a reference is made to Appendix B where the concepts of “electric” and “magnetic” antennas are discussed, the former being associated with an electric field that is orthogonal to the antenna base plane while the latter with an electric field that is parallel to that plane. In the

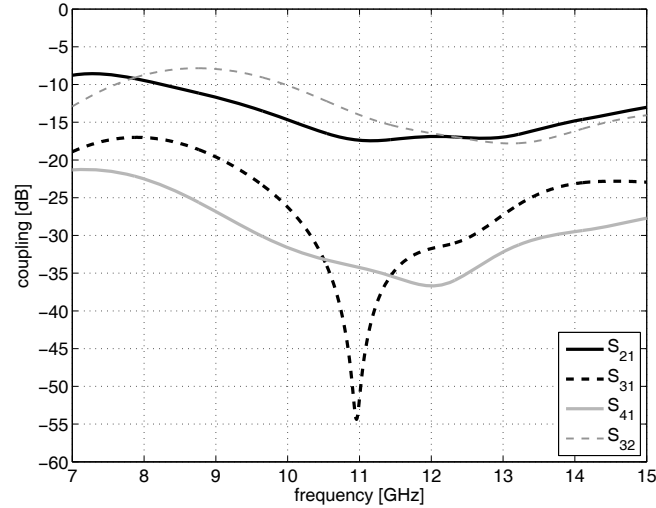


Figure 5.3: The coupling levels for the “Tulip” array.

case of antennas of the “electric” type, the mutual coupling reduction is traditionally achieved by using metal plated via enclosures of the radiating structure [58], [59]. The relevant vias, being parallel to the electric field lines, block the field directly coupled from one element to its neighbors. This idea was ported to the case of the loop-antenna described in Fig. 5.1 (that is of the “(quasi) magnetic” type), by replacing the through vias by means of slots (see Fig. 5.4). This novel technique allows the reduction of the mutual coupling without increasing the distance between the elements. Note that, while the use of via enclosures results in significant operational bandwidth reduction, the inclusion of the slots has virtually no such effect. Figure 5.5 depicts the return losses for the first and second antennas while the coupling levels in the array are depicted in Fig. 5.6. The most evident effect of the inclusion of the slots is the drastic reduction of S_{22} , accompanied by an extension of the impedance matching bandwidth that stretches now between 8.5 GHz and 15 GHz.

The length of the slot (h_{slot} in Fig. 5.4) is an important parameter to achieve the best performance of the array. The return losses of the array at the first two ports as a function of the slot lengths are represented in Figs. 5.7 and 5.8. From these graphs it can be concluded that the slot length should be greater than the stub length ($l+w_c+G=8$ mm in Fig. 5.9) since the field is concentrated between the stub and the ground. After a detailed investigation, it was decided to set h_{slot} to 9 mm in order to obtain the best return loss values.

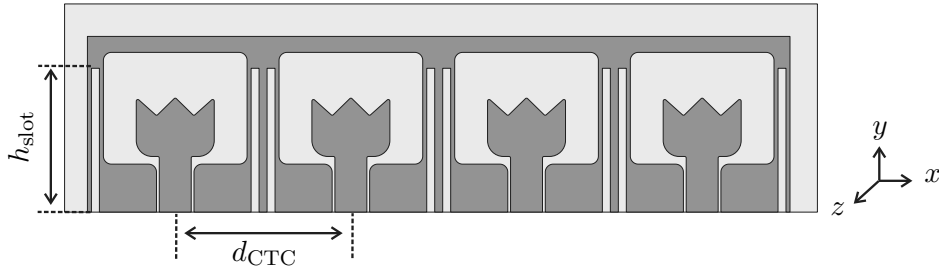


Figure 5.4: Linear array of slotted “Tulip” antenna.

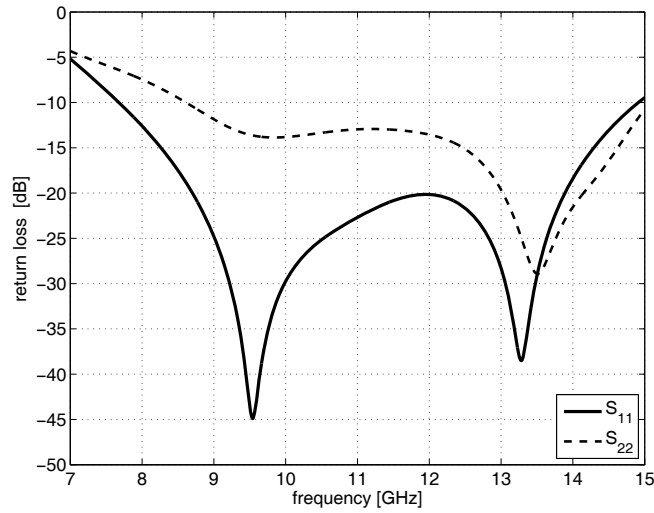


Figure 5.5: Return loss of the slotted “Tulip” array antenna.

The return loss frequency dependences in Figs. 5.7 and 5.8 highlight another important phenomenon. The shift of the lowest resonant frequency towards lower frequencies can be interpreted as indicative for an increase of the slot length. The increase of the stub length forces the current to travel along longer paths in both arms of the loop which eventually reduces the minimum resonant frequency.

Implementation considerations

The numerical investigation of the linear array consisting of “Tulip” loop antennas was commenced based on the configuration shown in Fig. 5.4. When implementing this configuration in a structure amenable to physical measurements, the very short length of the CPW necessitates for appending

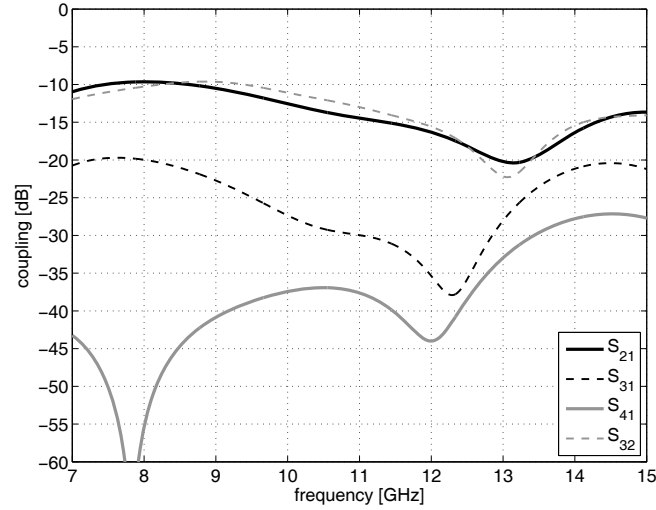


Figure 5.6: The coupling levels of the slotted “Tulip” array antenna.

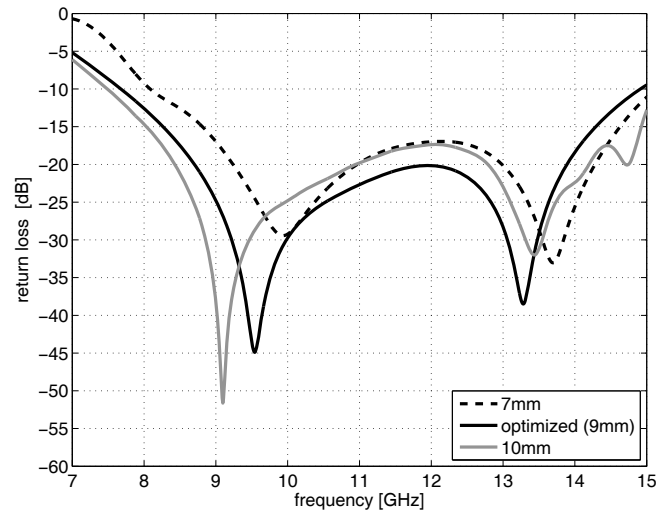


Figure 5.7: Return loss from the first port of the array depicted in Fig. 5.4, while the other ports are matched, versus slot length dependence.

the connectors a solution reminiscent of the one presented in Fig. 3.30, using a short piece of semi-rigid cable. This approach was already shown in Section 3.4.1 to be impeded upon by serious shortcomings that prevent the effectuation of quality measurements; a clear preference was therefore given to the extension of the CPW section by a safety segment of 40 mm.

Initial numerical experiments using a slot separating the zone occupied by

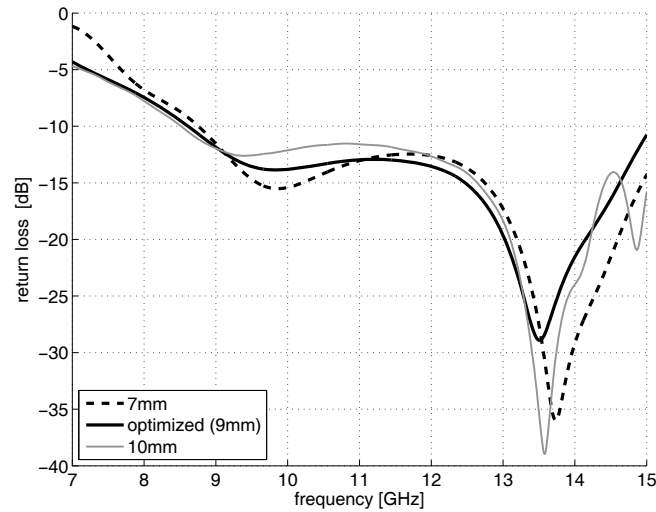


Figure 5.8: Return loss from the second port of the array depicted in Fig. 5.4, while the other ports are matched, versus slot length dependence.

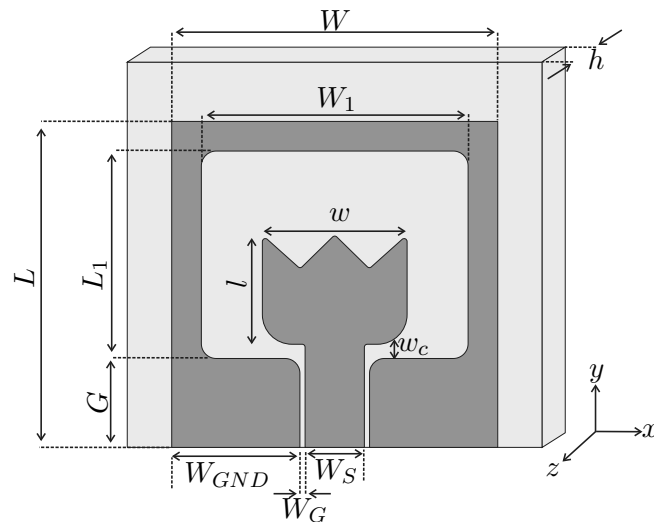


Figure 5.9: “Tulip” loop antenna, geometry, parameters and coordinate system.

the loops, only, demonstrated a dramatic deterioration of the impedance matching properties of the elements in the array. Upon zooming in on the current distribution in the feeding section it became abundantly clear that strong currents penetrated the ground plates, the behavior of the resulting transmission line deviating drastically from that of a CPW. This observation

pointed at the need to separate the ground plates pertaining to adjacent elements.

The straightforward solution to obtaining the desired separation would have been extending the slots in Fig. 5.4 along the complete CPW line. Nonetheless, the capacitive coupling that would have occurred due to the relatively high capacitance of the relevant structure would have yielded an insufficient separation between the lines. A much better solution is replacing the continuous slot by a succession of short slots acting collectively as a resonant circuit, the relevant structure being equivalent to an *electronic band-gap (EBG)*. A parametric study indicated as optimum solution the use of a row of equi-spaced short slots, the center-to-center distance of which amounting to $\lambda_g/18^1$ at the center frequency (10 GHz). Note that the relevant EBG structure also provides an efficacious mitigation of the mutual coupling between the radiators in the array. (This material will be published as a journal paper [89].)

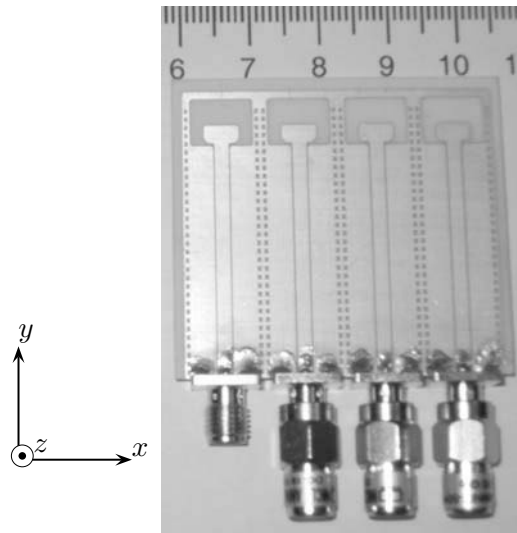


Figure 5.10: Fabricated linear array of CPW fed, printed, loop antennas and coordinate system.

To conclude with, the spacing between the adjacent elementary antennas was kept as 11 mm, corresponding to 0.44λ at 12 GHz. With these choices, the fabricated linear array is depicted in Fig. 5.10.

¹Here, λ_g is defined as $\lambda/\sqrt{\epsilon_{eff}}$ where λ is the free space wave length and ϵ_{eff} is some effective permittivity that applies to the domain occupied by the radiator.

5.1.2 Array performance assessment

Scattering parameters measurement

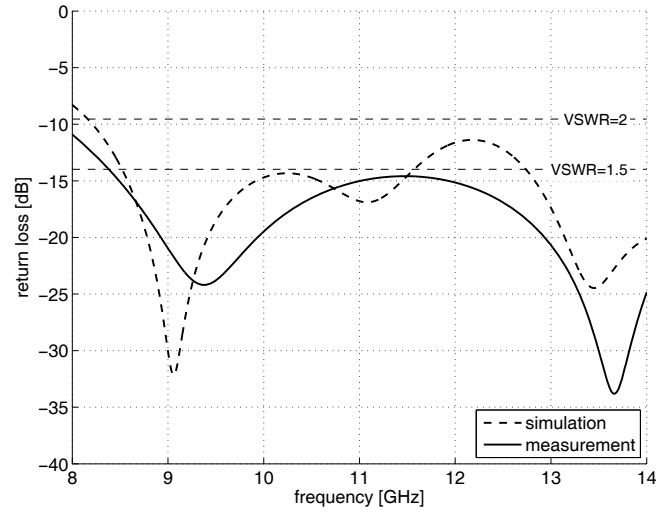
As in the case of the previously reported scattering parameter numerical experiments, the first set of measurements concerned the reflection coefficient at each port, with all other ports terminated on matched loads of $50\ \Omega$, as depicted in Fig. 5.10. Due to the reasons explained in Section 5.1, the magnitude of the reflection coefficients at port 1 (S_{11}) and port 2 (S_{22}) are depicted in Fig. 5.11, only.

These reflection coefficients, as stated previously, were measured by resorting to time-domain de-embedding for suppressing the extraneous effects of the SMA to CPW waveguide transition and of the soldering. From Figs. 5.11 (a) and (b) it can be inferred that, although the general trend of the measurement and the simulated curves are similar, the measured ones give a smoother response (except around the resonance regions) due to the employed measurement technique. The measured result from port 2 indicates an operational bandwidth for a $VSWR \leq 2$ of 47%, stretching between 8.7 GHz and 14 GHz. (This material will be published as a journal paper [89].)

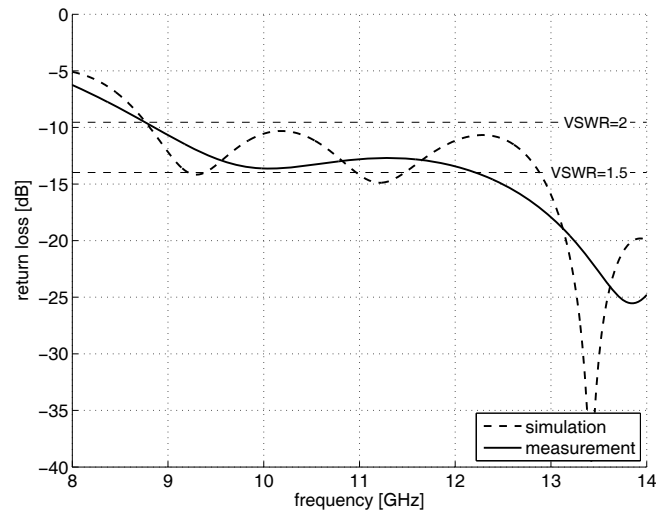
Array impedance matching analysis

The analysis of the frequency dependence of the array reflection coefficient was carried out in two steps. Firstly, a truly UWB study was conducted by *synthesizing* the array behavior by means of the strategy described in the Appendix D. Both computer simulations and direct measurements were employed for generating the array scattering matrix $[S]$. This study focuses on the *array return loss*, defined as the reflection coefficient experienced at the access port of the array antenna, when fed via a divider/combiner network, the phase shifters needed for ensuring progressive phase included². In a second stage, the behavior of a complete, *non-scanning* array was examined by feeding the array via a 1:4 Wilkinson divider. This device presents its optimum performance at 9 GHz (input reflection coefficients at all ports below -20 dB) and an operational bandwidth of $7\ \text{GHz} \div 9.5\ \text{GHz}$, that was also adopted as the explored frequency band in this study.

²The performed numerical experiments assumed *ideal* divider/combiner networks and an *ideal* true-time implementation of the phase shifters.



(a)



(b)

Figure 5.11: Simulated and measured return loss concerning the loop array antenna of Fig. 5.10 (a) $S_{11}(=S_{44})$; (b) $S_{22}(=S_{33})$.

UWB synthetic array performance study The UWB study of the synthetic array was effectuated for the frequency in the range $7\text{ GHz} \div 14\text{ GHz}$. The reduced dimension of the investigated array allowed evaluating the $[S]$ matrix at 1001 frequency samples in the examined band. By applying the algorithm in Appendix D, the reflection coefficient was calculated at all frequency samples for scanning angles in the range $\vartheta_0 \in [0^\circ, 90^\circ]$.

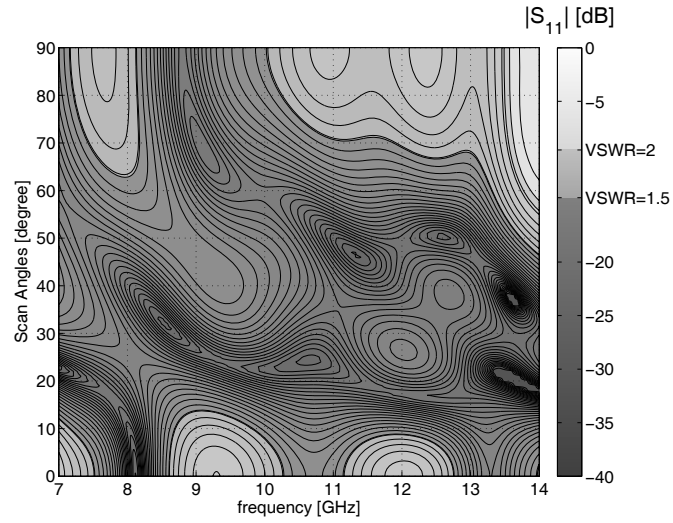


Figure 5.12: Frequency and scanning angle dependence of the array return loss for the simulated scattering matrix. Note that $|S_{11}|$ stands in these plots for the array return loss.

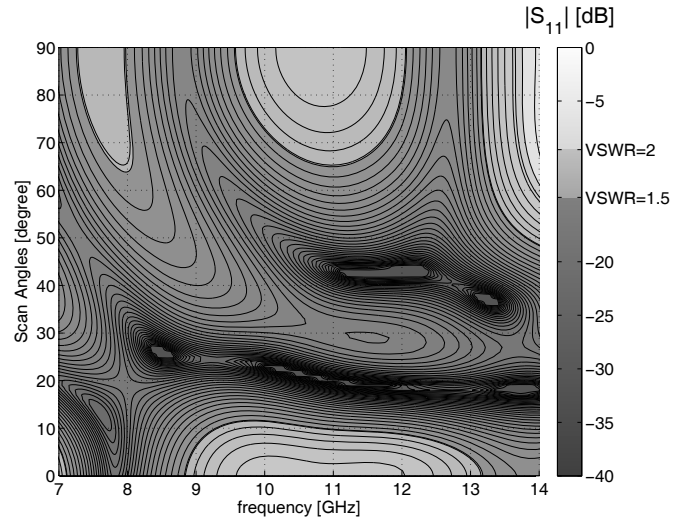


Figure 5.13: Frequency and scanning angle dependence of the array return loss for the measured scattering matrix. Note that $|S_{11}|$ stands in these plots for the array return loss.

This strategy was applied to the *simulated* scattering matrix, the results of this analysis are reported in Fig. 5.12. From it, it can be derived that, except for a small region corresponding to scanning angles $\vartheta_0 \geq 60^\circ$

and frequencies $f \geq 13.6$ GHz, the array performance satisfies the condition $\text{VSWR} \leq 2$. Moreover, an excellent impedance matching ($\text{VSWR} \leq 1.5$) is obtained for scanning angles ranging from $\vartheta_0 = 10^\circ$ to $\vartheta_0 = 60^\circ$. These results demonstrate the extremely adequate behavior of the advocated CPW fed, printed loop antenna in array environments. Based on Fig. 5.12 it can be concluded that, for scanning angles $\vartheta_0 \leq 60^\circ$, the array's operational bandwidth for $\text{VSWR} \leq 2$ stretches over the investigated 7 GHz \div 14 GHz range (corresponding to a fractional bandwidth of 67%). Nevertheless, this value has to be corrected by accounting for the onset of grating lobes. To this end, it is noted that the electrical spacing between the individual elements becomes 0.5λ for $f = 13.6$ GHz, with λ denoting the free space wavelength. Upon taking this frequency as the limit of the operational bandwidth, the fractional bandwidth becomes 64%, which will be hereafter employed as a reference.

The same approach was then applied to the *measured* scattering matrix, the relevant frequency–scanning angle characteristic being shown in Fig. 5.13. The general features of the simulated results can also be identified here. The dissimilarities are ascribed to a twofold cause. Firstly, certain inconsistencies are to be expected in the process of replicating the model (small shape inaccuracies, variations in the material properties, etc). A second source of differences is the time-domain de-embedding employed for effectuating the measurements, a measure that was called upon for suppressing the extraneous effects of the SMA to CPW waveguide transition and of the soldering. It should also be noted that no regions where the VSWR exceeds 2 are present in Fig. 5.13. To conclude with, the operational bandwidth that characterized the simulated values are preserved in the case of the measured data.

UWB, direct measurement examination of a non-scanning array

A final array reflection coefficient study concerned a non-scanning linear array obtained by feeding the elements via a 1:4 Wilkinson divider. The divider ensures a balance between the output ports that is better than 0.5 dB in magnitude and 44° in phase. The obtained measurement results are compared in Fig. 5.14 against the corresponding synthetic array performance. As concerns the resonance occurring in the explored band, there is an excellent agreement between the two measured results. As for the difference of 0.33 GHz between the measured and the simulated data, it is interpreted as an effect of the twofold reasoning mentioned in Section 5.1.2.

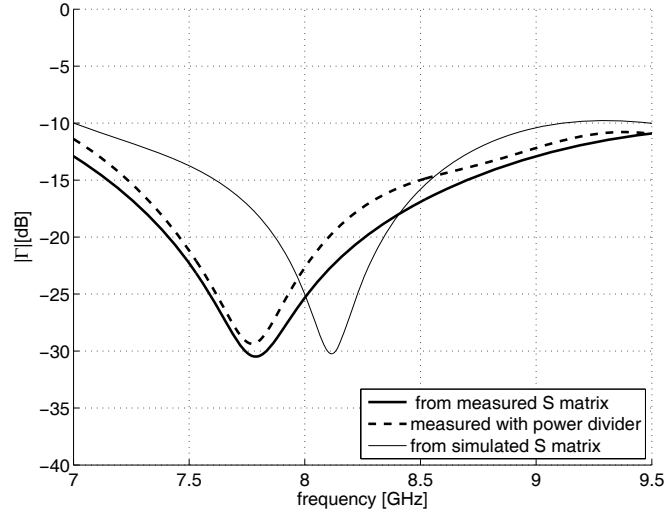


Figure 5.14: Frequency dependence of the array return loss for the power divider fed array. Comparison with the synthesized data concerning the simulated and measured scattering matrix.

Radiation pattern investigation

Due to the individual radiators being deployed along the Ox – axis (see the coordinate system in Fig. 5.10) and having (practically) omnidirectional patterns in the $\phi = 0^\circ$ cut, thus allowing excellent scanning possibilities, the reported radiation pattern explorations are confined to this cut. By assuming a time-harmonic excitation of frequency f_0 , the radiation pattern of the array consisting of 4 elements reads [57, p. 79]

$$\mathbf{E}(\vartheta) = \sum_{i=1}^4 \mathbf{f}_i(\vartheta) \exp \{j k x_i [\sin(\vartheta) - \sin(\vartheta_0)]\}, \quad (5.1)$$

in which $\mathbf{f}_i(\vartheta)$ denote the individual radiation patterns as a function of ϑ , $j = \sqrt{-1}$, $k = 2\pi f/c_0$ denotes the wave number in free space (with $c_0 = 3 \cdot 10^8$ m/s representing the electromagnetic wave velocity in free space), x_i denote the element locations with respect to the chosen reference frame and ϑ_0 defines the main beam’s steering direction. Furthermore, for ensuring the consistency with Section 3.4.2, f is taken as 8.5 GHz and 12 GHz respectively.

With these choices, a first set of radiation patterns is obtained by considering the elementary radiation patterns and multiplying them with the array factor, which will be hereafter referred to as *simulated*. As for the

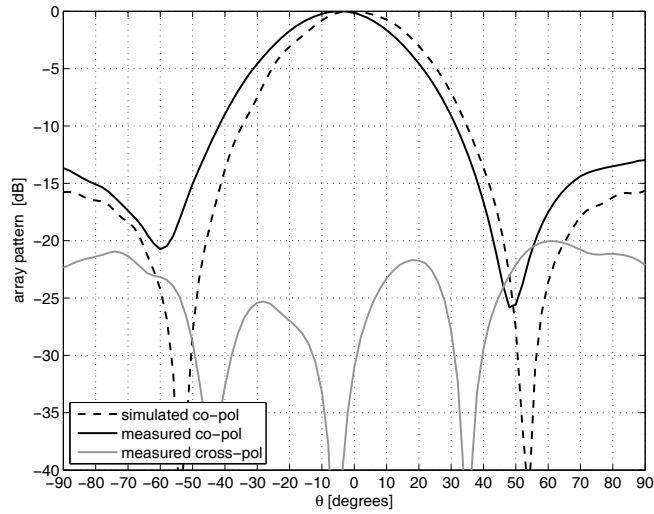
measured radiation patterns, these were evaluated by mounting the array in an upright position on a rotating turntable, with its symmetry axis aligned with the turntable axis. The individual radiation patterns were measured with all other ports terminated with matched loads. By keeping the array phase center fixed, the $\exp[jkx_i \sin(\vartheta_0)]$ terms in Eq. (5.1) are incorporated in the complex measured data $f_i(\vartheta)$. This will be hereafter referred to as *measured*.

The simulated and the measured results are presented in Fig. 5.15. The first observation is that there is a beam shift of about 4° in the measured radiation patterns. This is due to small alignment problems of the measurement set-up. The difference between the null depths is also related to this alignment problem. Another difference comes from the mutual coupling. In the simulated radiation pattern, no mutual coupling was included since the radiation pattern of an isolated antenna was used. However, in the measured radiation patterns, since the patterns were measured in the array environment, the related mutual coupling effects were inherently taken into account. This may also contribute to the little discrepancies between the simulated and the measured data in Fig. 5.15. It should also be noted that the cross polar component of the radiation pattern is more than 25 dB below the main beam in the $\{\phi = 0^\circ; \phi = 180^\circ\}$ cut.

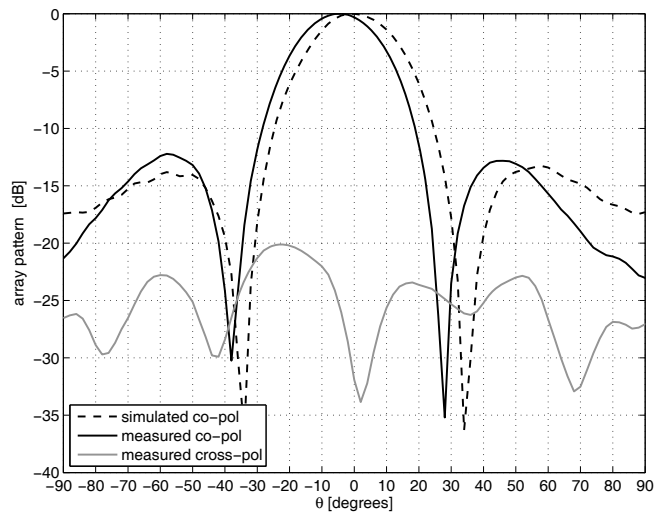
The pattern measurements were completed by examining the non-scanning, broadside array using the Wilkinson divider. In view of the divider providing optimum power transfer at 9 GHz, the measurement was carried out at this frequency, the results being compared in Fig. 5.16 with the corresponding synthesized pattern. Note that at this frequency the balance between the output ports amounts to 0.1 dB in magnitude and to 42° in phase. The two patterns compare very well, except for the fact that no main beam squint is observed in the power divider measurements and that some variations in the side-lobe distribution and in the depth of the first nulls are visible. The latter dissimilarities can be easily explained by observing that the phase unbalance between the signals fed to the individual radiators is relatively high. (This material will be published as a journal paper [90].)

5.2 Linear arrays consisting of “Eared” elements

In Section 3.2, a CPW-fed, quasi-magnetic, printed “Eared” antenna was described and investigated in detail. The single antenna has a measured operational bandwidth for $VSWR \leq 2$ of 149.8%, stretching over the frequency range $6.46 \div 45$ GHz. The maximum dimension of the single antenna in the x direction is 12 mm, which amounts to 0.5λ at 12.5 GHz.



(a)



(b)

Figure 5.15: Normalized simulated and measured radiation patterns at (a) 8.5 GHz; (b) 12 GHz.

The behavior of this type of antenna in uniform, linear array environments is now investigated based on two prototypes, one containing 7 elements and one containing 15 elements. Some general remarks apply to the examined array antennas. Firstly, based on arguments that were elaborated upon in the previous section, a feeding by means of an extended CPW section was taken into account, exclusively (See Fig. 3.19 for an image of

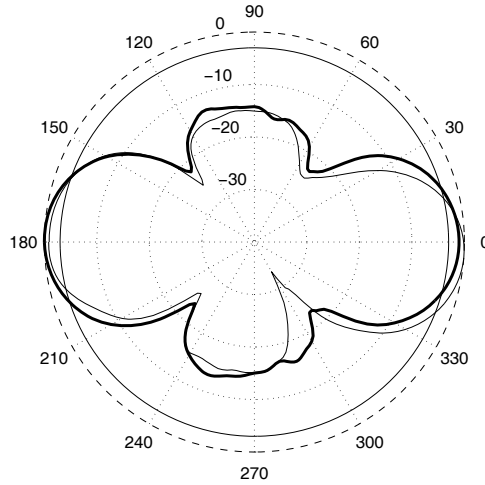


Figure 5.16: Normalized radiation patterns corresponding to the $\{\phi = 0^\circ; \phi = 180^\circ\}$ cut, at 9 GHz. Thick line – measurement with power divider feeding; thin line – separate measurement of each antenna and MATLAB summing up.

an individual “Eared” antenna, with the pertaining extended CPW line). Furthermore, the current penetration in the ground planes required, in the case of the array consisting of “Tulip” loop antennas, the separation of the CPW lines by means of rows of slots (see Fig. 5.10). Nevertheless, unlike in the case of the “Tulip” loop antenna, at Section 3.2.3 it was shown that the electromagnetic field is concentrated in the case of the “Eared” antenna in the close proximity of the radiating part’s neck. This observation led to conjecturing that the field will be further confined to the CPW line gaps, with negligible diffusion into the ground plates. This hypothesis was verified numerically by analysing variants of the linear array with solid ground plates and with separating slot rows, the observed differences being marginal. In view of ease of fabrication, it was then decided to resort to solid ground plates for the CPW lines.

5.2.1 Analysis of the linear array containing 7 elements

To begin with, a linear array consisting of 7 “Eared” antennas is considered. With the choices explained above, the linear array depicted in Fig. 5.17 was eventually opted for. The center-to-center spacing of two consecutive elements is $d_{\text{CtC}} = 14 \text{ mm}$ (0.56λ at 12 GHz), yielding a minimum distance $g = 2 \text{ mm}$ (this distance is measured between the closest circular sections of

adjacent radiators). The aggregate length of the array amounts to 98 mm.

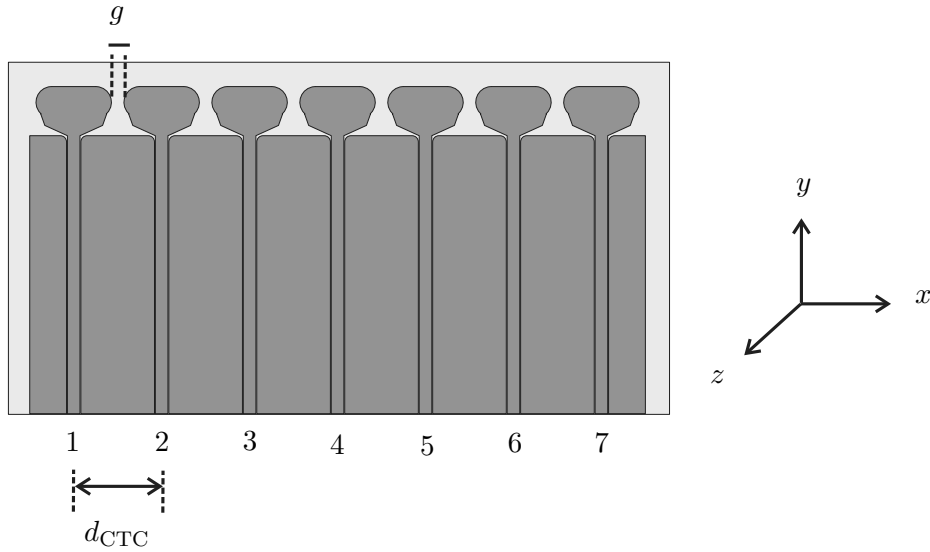


Figure 5.17: Configuration of the linear array consisting of 7 “Eared” antennas and the coordinate system.

The adopted configuration was then manufactured in etched microwave laminate technology. The employed laminate was Duroid RT 5870 with a relative permittivity $\epsilon_r = 2.33$. The completely assembled array is shown in Fig. 5.18.

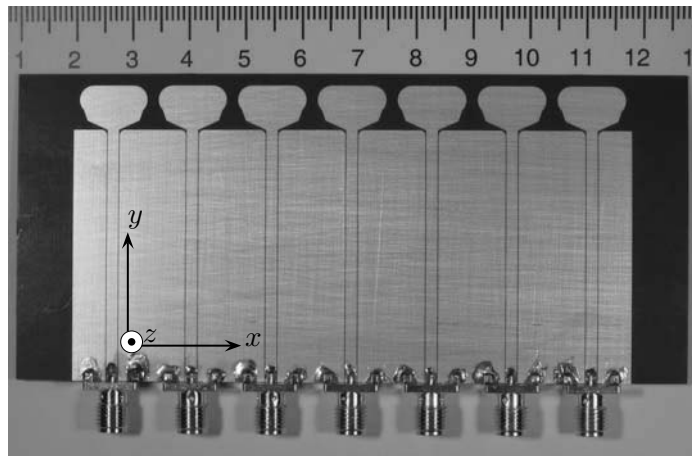


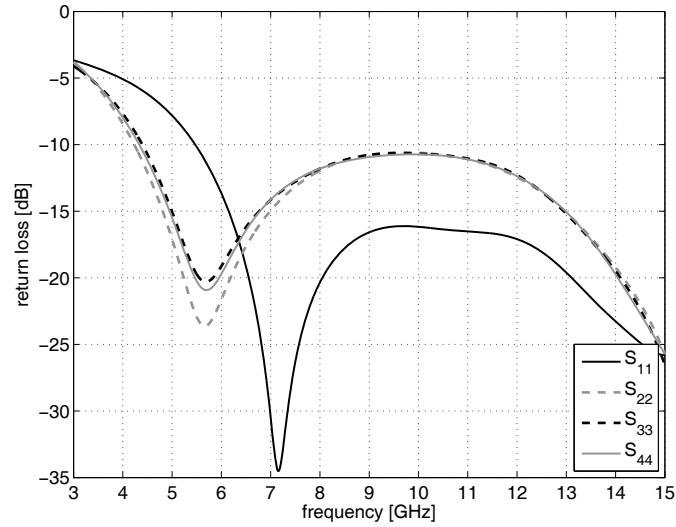
Figure 5.18: Photo of the linear array consisting of 7 “Eared” antennas.

Scattering parameters numerical analysis

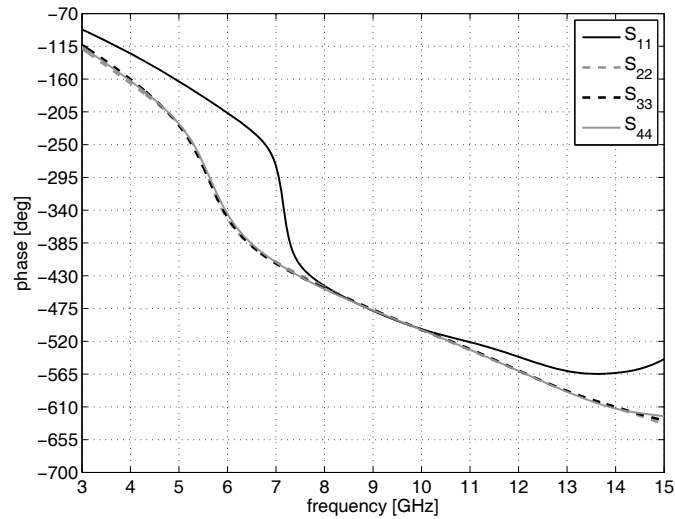
The analysis starts with a numerical study of the frequency dependence of the reflection coefficient at the terminals of the array elements. In view of the configuration's symmetry, the study is confined to the elements 1 to 4, the relevant return losses being depicted in Fig. 5.19. From these plots it can be seen that the elements 1 to 3 present a clearly different behavior. Nonetheless, the behavior of the elements 3 and 4 is remarkably consistent, allowing to infer that starting from element 3 onwards the individual radiators perform as if incorporated in an infinite array. This observation will allow a drastic reduction of the number of elementary parameter evaluations in the case of (much) larger, linear arrays, this rendering feasible the examination of such configurations. Concretely, in those cases, after simulating or measuring the elements at the array edges, the performance of the inner elements will be extrapolated based on the data corresponding to that of element 3.

The next step was represented by the evaluation of the coupling coefficients in the scattering matrix of the linear array. Based on numerical experiments it was decided that, except for the elements 1 and 7, the couplings between neighboring elements, i.e. S_{23} , S_{34} , S_{45} and S_{56} , can be taken to be equal. Similarly, the couplings between elements having one element in between, i.e. S_{24} , S_{35} and S_{46} , can be also taken to be equal. In order to justify this, the largest discrepancies between quantities taken to be equal, in this case between S_{35} and S_{46} , are shown in Fig. 5.20. The differences amount to at most 5% in the relative deviation between magnitudes and to at most 4° shift in phase, this fully justifying the assumption that was made. Finally the couplings between the elements having two or more elements in between are below -30 dB and can be neglected. These approximations, in conjunction with the assumption that the return loss for elements situated further than two elements away from the array edges is constant, will be hereafter referred to as *approximation rules*. Resorting to these rules provides an effective method for filling the scattering matrix of (large) arrays consisting of "Eared" antennas. A similar approach was suggested in [50] regarding the synthesis of array patterns, where elements beyond the first two from the edges are considered to have the same radiation pattern. With this contribution we have extended this approach by calculating the complete reflection coefficients of the array.

Once the complete scattering matrix is assembled, the *active reflection* coefficients, i.e. the reflection coefficient at the terminals of an array element when all array elements are in place and excited [5], of the embedded radiators can be computed, the results being presented in Fig. 5.21. In it, the



(a)



(b)

Figure 5.19: Simulated reflection coefficient magnitude for the linear array of Fig. 5.17: (a) magnitude; (b) phase.

attribute “actual” refers to scattering matrix entries following directly from the numerical simulations whereas the attribute “approximate” refers to the values adopted according to the approximation rules referred to above. From these plots it can be derived that the deviations due to accounting for the indicated approximations are very small. The plots also document a clear

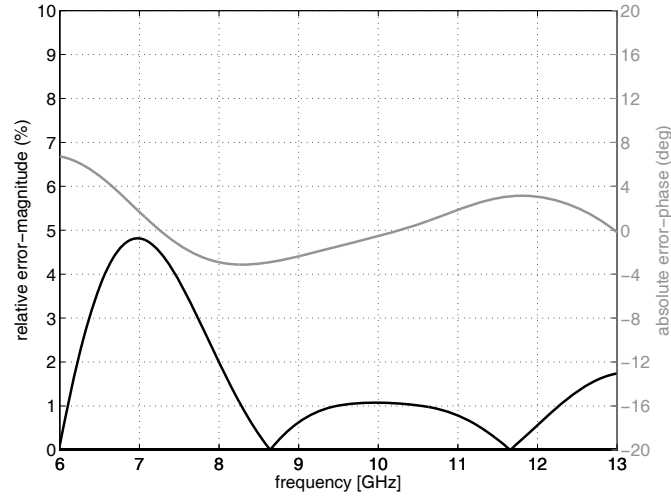


Figure 5.20: Magnitude and phase difference of S_{35} and S_{46} concerning the linear array of Fig. 5.17.

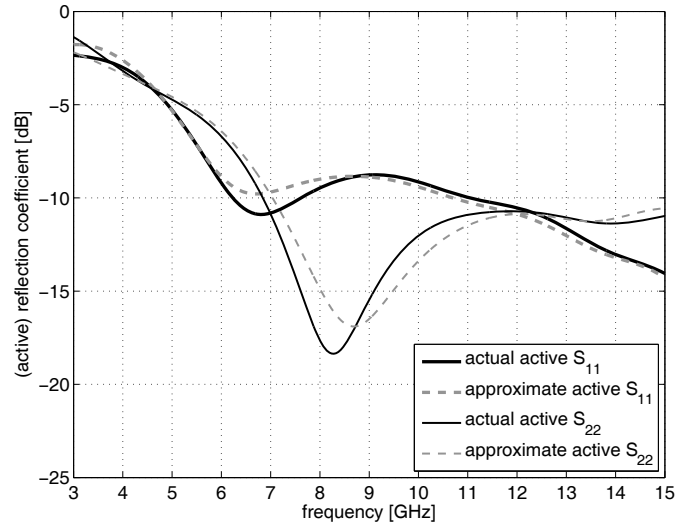
“convergence” of the active reflection coefficient when moving towards the array center, this being illustrative for the innermost elements behaving as if included in infinite arrays.

Finally, except for the extreme elements, the embedded radiators display excellent UWB properties, with matching better than $VSWR \leq 2$ matching for frequencies between 4 and 15 GHz.

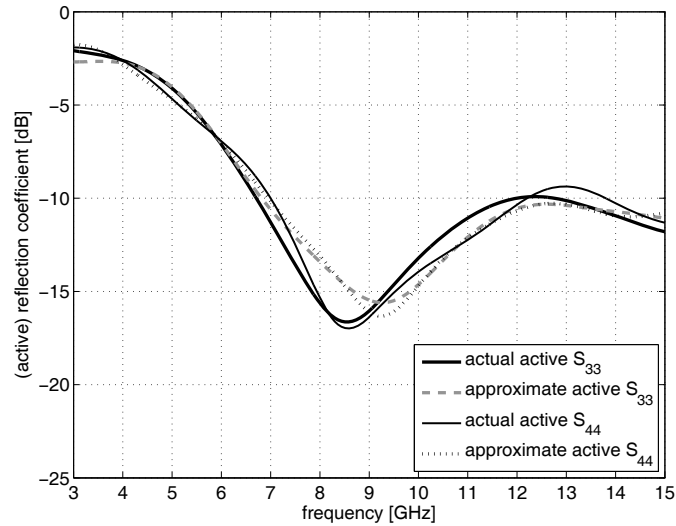
Array impedance matching analysis

The frequency behavior of the reflection coefficients at different scanning angles is now evaluated by means of the method described in Appendix D. Note that, unlike in the case of the “Tulip” loop antennas, results following from the measured data will be now reported, only. The measurements were carried out by using a multi-port test-set (MTS) (Agilent 87050A, Option K24)³ in which the time-domain de-embedding methods were applied in order to suppress the extraneous effects of the SMA to CPW waveguide transition and of the soldering. The beam forming matrix is emulated in MATLAB. The synthesized reflection coefficient of the array is depicted in Fig. 5.22, showing that there is an excellent impedance matching beyond 7.5 GHz for scanning angles between $\vartheta_0 = 0^\circ$ and $\vartheta_0 = 70^\circ$. However some

³The experimental set-up concerning the array impedance matching analysis is depicted in Fig. 5.27.



(a)



(b)

Figure 5.21: Active reflection coefficients, for $\vartheta_0 = 30^\circ$, concerning the linear array of Fig. 5.17: (a) S_{11} and S_{22} ; (b) S_{33} and S_{44} .

blind angles can be observed above $\vartheta_0 = 70^\circ$ between 10 GHz and 11 GHz.

Figure 5.23 shows a comparison between the measurement results and the simulated array reflection coefficient evaluated by means of the CST Microwave Studio package [26], the data referring to a broadside array. A minimum frequency for $\text{VSWR} \leq 2$ of approximately 7.5 GHz is observed in

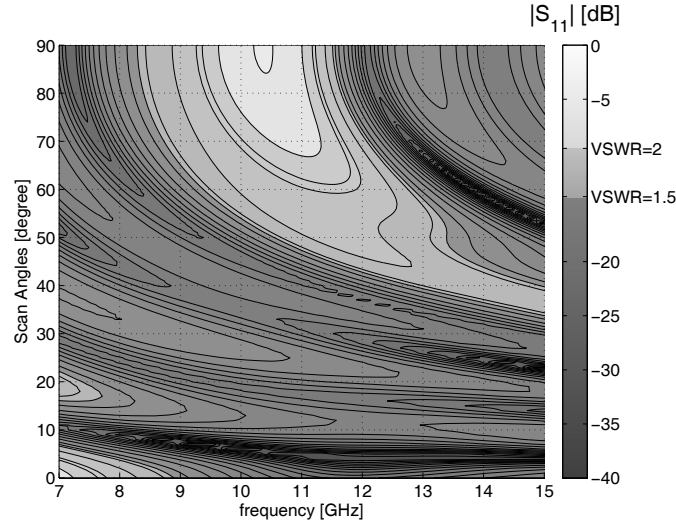


Figure 5.22: Frequency dependence of the reflection coefficient magnitude for different values of scanning angles; as derived from the measured data for the linear array of Fig. 5.18. Note that $|S_{11}|$ stands in these plots for the array return loss.

both cases. Nevertheless, on the overall, the measured results indicate lower reflection coefficients than the simulated ones. This discrepancy arises from the time-domain de-embedding technique that was employed for measuring the S matrix.

Radiation pattern investigation

Following the same reasoning given in Section 5.1.2, the reported radiation pattern explorations are confined to the $\phi = 0^\circ$ cut. These results were obtained by summing up the measured radiation patterns, on the one hand, and by direct numerical simulation, on the other hand, the two sets of data being plotted in Fig. 5.24 for two operational frequencies, namely at 8 GHz and 10 GHz.

A calibration was needed for compensating for the intervening phase differences that amounted to a maximum of 35° in the case of the multi-port test-set and to a maximum of 10° for the interconnecting cables. Note that the use of the MTS⁴ allowed measuring all antennas, sequentially, for each angle of the turntable. In this manner, a significant reduction

⁴The experimental set-up concerning the radiation pattern investigation is depicted in Fig. 5.29.

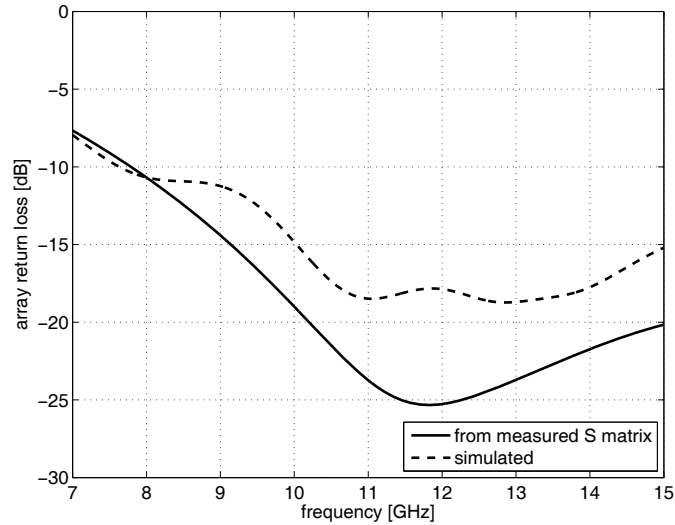


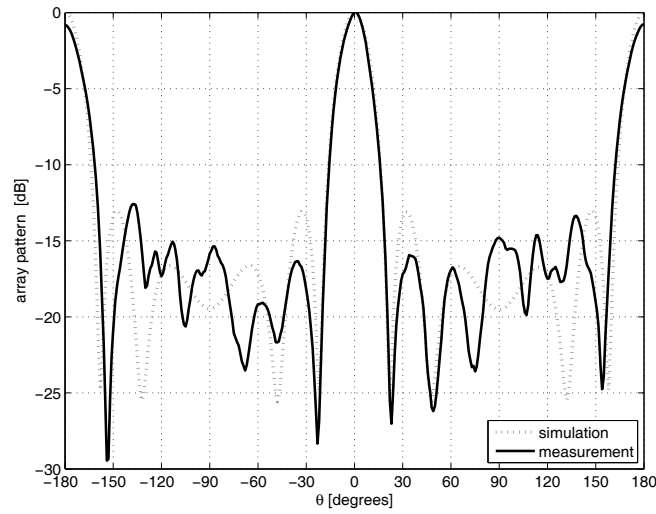
Figure 5.23: Simulated and calculated array return loss concerning the “Eared” antenna array of Figs. 5.17 and 5.18.

of the measurement time was achieved by eliminating the need to return the turntable at its initial position for carrying out a full radiation pattern measurement for each element, separately.

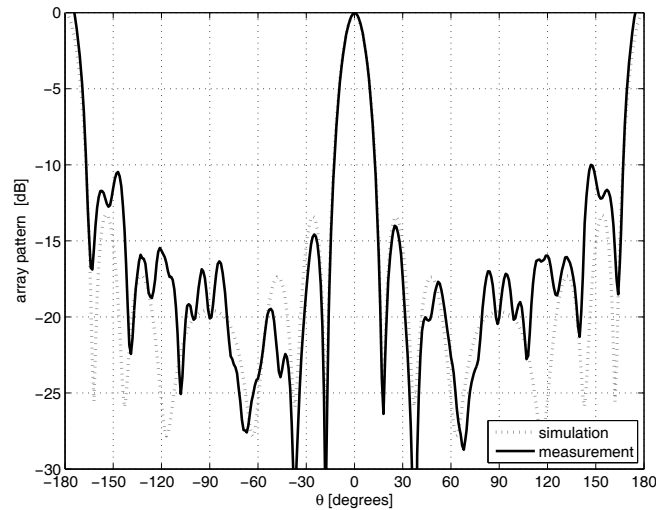
In both plots there is an excellent agreement between the measured and simulated data around the main beam region of the radiation patterns. A 3 dB difference in the first sidelobe level at 8 GHz and some discrepancies around the far side lobes are noticed, especially at 8 GHz. For example, the nulls appearing around $\theta = \pm 90^\circ$ in the simulated pattern are replaced by side lobes.

5.2.2 Analysis of the linear array containing 15 elements

The experience acquired during the study of the array consisting of 7 elements created the basis for carrying out an investigation of a significantly larger linear array, consisting of 15 “Eared” antennas. The design and fabrication principles that were elaborately discussed in the previous section were employed for realising the larger antenna, the completely assembled device being shown in Fig. 5.25.



a



b

Figure 5.24: Normalized simulated and measured radiation patterns of the linear array composed of 7 elements (Figs. 5.17 and 5.18) at (a) 8 GHz; (b) 10 GHz.

Scattering parameters numerical analysis

Initially, the scattering matrix of the complete array is assembled by using the simulated results obtained for the 7 elements array studied before, in conjunction with the approximation rules introduced in Section 5.2.1. The knowledge of the complete scattering matrix allows evaluating the active reflection coefficients. For example, the frequency behavior of the active

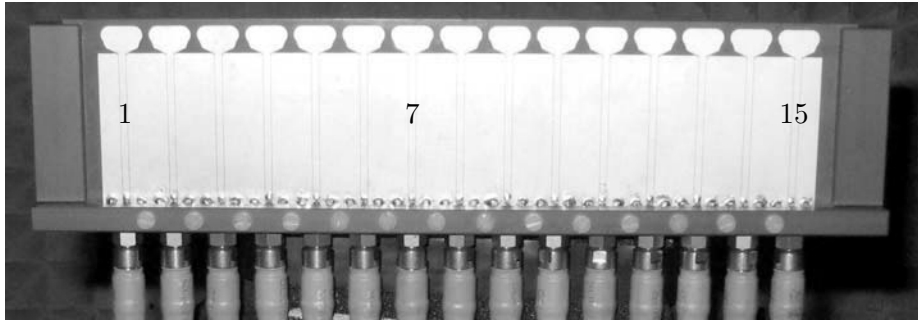


Figure 5.25: Photo of linear array of 15 CPW fed “Eared” antennas.

reflection coefficients pertaining to the elements 1-7 only⁵, calculated for a scanning angle $\vartheta_0 = 30^\circ$, are represented in Fig. 5.26. This plot shows a clear “convergence” of the active reflection coefficient when moving towards the center of the array, this supporting the idea that the inner elements behave as if they are embedded in infinite arrays. Furthermore, except for the first and the last elements of the array, the radiators exhibit good UWB properties, with better than $VSWR \leq 2$ matching for frequencies between 7 and 15 GHz.

Array impedance matching analysis

Just like in the case of the linear array consisting of 7 elements, the study reported in this section will employ measured data, exclusively. Moreover, the multi-port test-set was employed for increasing the efficiency of the measurements, the complete set-up being illustrated in Fig. 5.27.

To demonstrate the accuracy of the analysis strategy already employed in the case of the array consisting of 7 elements, the scattering matrix of the linear array is assembled in two ways: on the one hand, by resorting to the approximation rules, the relevant results being termed as “approximated”;

⁵In view of the configuration’s symmetry, this study is relevant for the complete array.

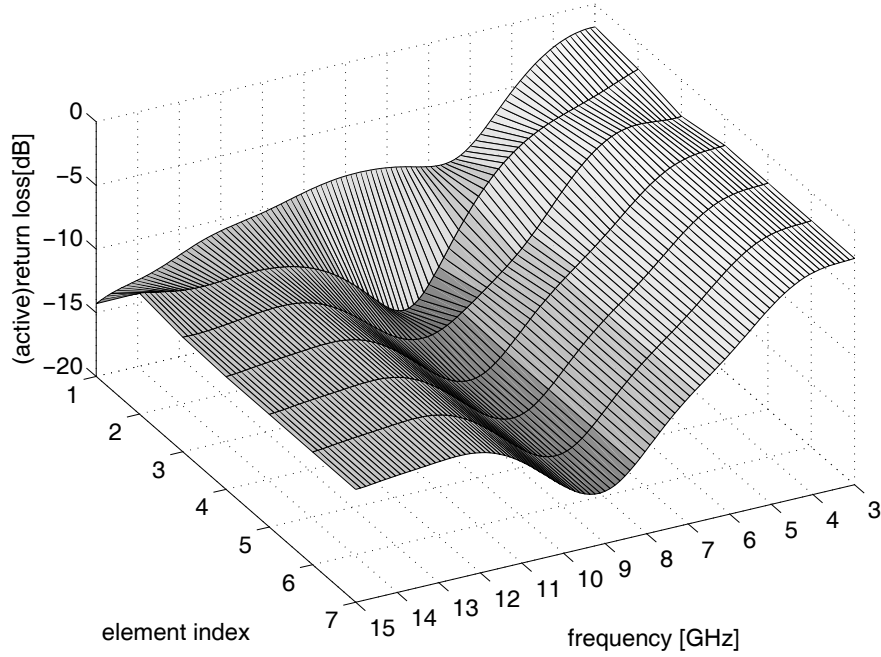


Figure 5.26: Calculated active reflection coefficients concerning the linear array of Fig. 5.25.



Figure 5.27: Reflection coefficient measurement set-up of the linear array of 15 CPW fed “Eared” antennas.

on the other hand, by a full measurement of all entries, the relevant results being referred to as “measured”. By now resorting to the algorithm given in

Appendix D, the frequency dependence of the array reflection coefficient at variable scanning angles are evaluated by means of the two scattering matrices, the results being presented in Fig. 5.28. By comparing the two plots, the similarity is evident, this providing a convincing proof of the accuracy of the employed approximation. As for the effectiveness of this approach, it suffices to say that in the case of the linear antenna consisting of 15 elements it allows a reduction of the measurement time by a factor of 15. Nonetheless, the largest time saving following from the use of the approximation rules comes from drastically reducing the time needed for calibrating the system. As discussed in Section 5.2.1, the MTS was used for measuring the scattering parameters of the array and before starting the measurement a calibration procedure should be applied in order to eliminate all effects coming from the MTS and the cables connecting the array to the MTS.

Although the calibration is done via an electronic calibration set (E-cal set), a single two port calibration takes approximately 5 minutes, including the fastening and the detaching of the connectors. On the one hand, for the array without any approximation the calibration procedure should be carried out 105 times, yielding a total of 525 minutes to calibrate the full system. On the other hand, the approximated measurement requires only 4 two-port calibrations, this resulting into a total calibration time of only 20 minutes. Consequently, resorting to the approximation rules allows reducing the calibration time by a factor of 26.

The examination of Fig. 5.28 also allows deriving that the linear array under investigation has an operational bandwidth for a VSWR ≤ 2 of 61% stretching between 8 GHz and 15 GHz. An excellent impedance matching for the scanning angles between $\vartheta_0 = 0^\circ$ and $\vartheta_0 = 60^\circ$ for the whole frequency band can be noticed. However some blind angles can be observed above $\vartheta_0 = 60^\circ$ between 10 GHz and 12 GHz similar to the case of the array consisting of 7 elements.

Radiation patterns investigation

The validation of the linear array composed of 15 elements, was rounded off by measuring the radiation patterns.

UWB broadside performance assessment These patterns were measured by using the MTS, as explained previously, the measurement set-up being depicted in Fig. 5.29. During the measurements, the front side of the measurement set-up under the antenna connectors, together with the measurement cables connecting the array and the multiport test set, are covered

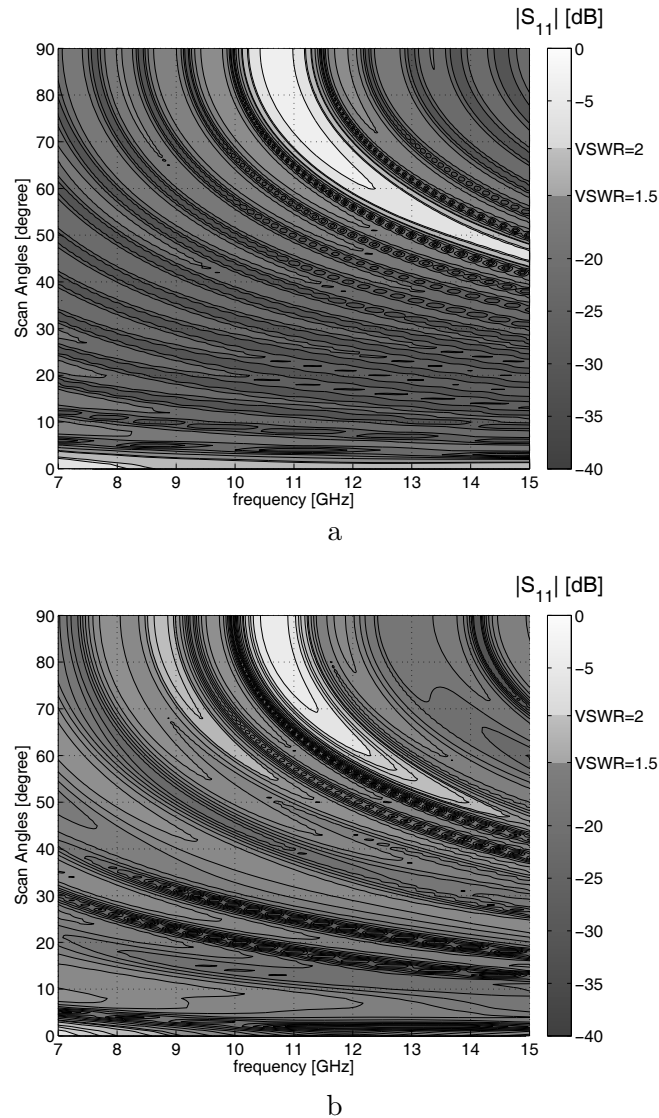


Figure 5.28: Frequency dependence of the reflection coefficient magnitude for different values of scanning angles; (a) assembled from the approximated data; (b) assembled from the measured data. Note that $|S_{11}|$ stands in these plots for the array return loss.

with absorbers in order to eliminate the reflections from these parts. As described in Section 5.2.1 the radiation patterns are measured sequentially at each angle and the phase differences given by the MTS and the cables are calibrated out. Since all the antennas are measured in the array environment, all the mutual coupling effects are inherently included. The rationale behind this assessment lies in the fact that, since the other elements are

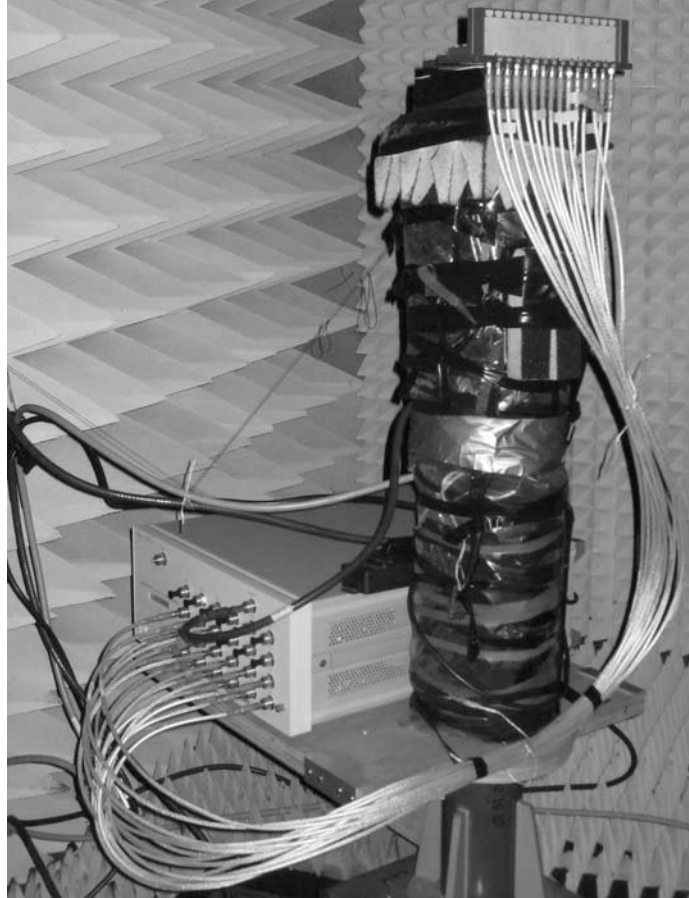


Figure 5.29: Radiation pattern measurement of the linear array of 15 CPW fed “Eared” antennas.

terminated with matches loads during the excitation of each antenna element, the couplings from the excited element to the passive elements are already accounted for in the antenna pattern measurement. The individual measured radiation patterns are then combined by means of a MATLAB post-processing that performs the summation of the complex antenna element patterns. In this manner, the effect of the complete scattering matrix of the array on its radiation pattern is automatically accounted for.

A plot showing all radiation patterns between 5 GHz and 15 GHz is depicted in Fig. 5.30. In this graph the values are normalized with respect to the maximum value in the complete experiment. As expected, the main beam gets smaller by moving to higher frequencies due to the linear array becoming electrically longer. Since the element pattern is bi-directional, the

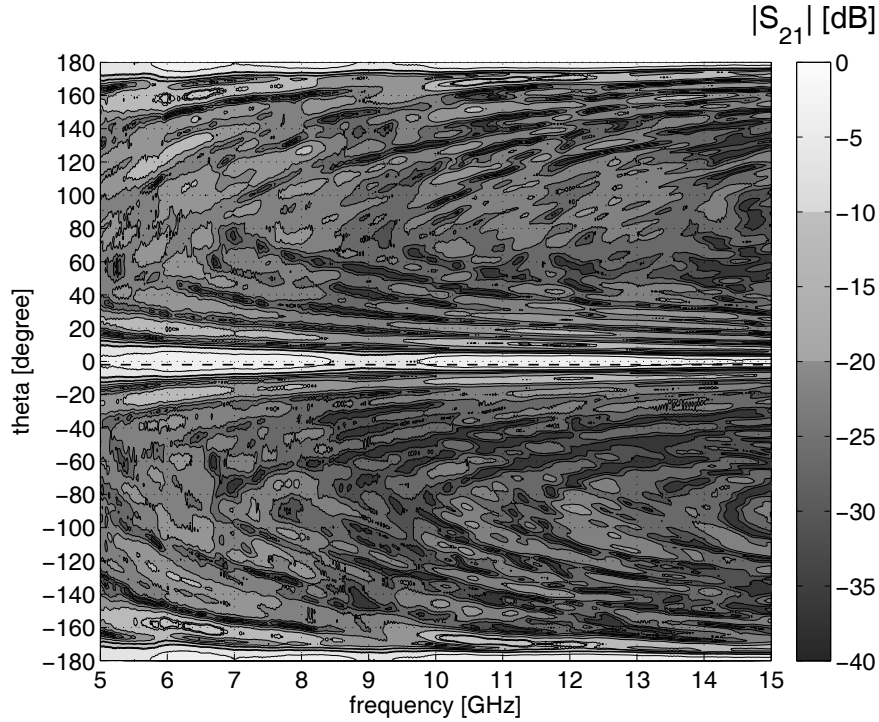


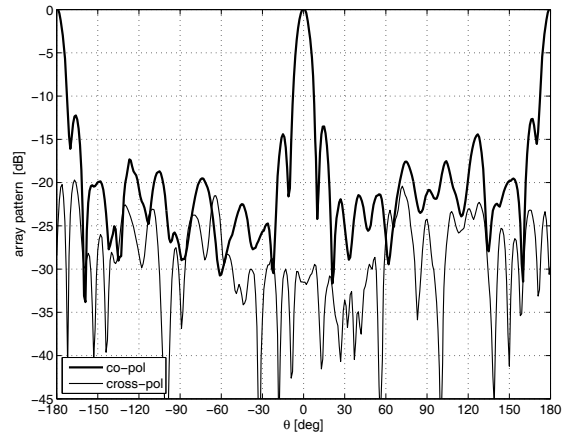
Figure 5.30: Radiation pattern measurement of the linear array of 15 CPW fed “Eared” antennas.

array pattern is also bi-directional which can be seen in this figure at $\theta = 0^\circ$ (broadside of the array) and to $\theta = 180^\circ$ (back side of the array).

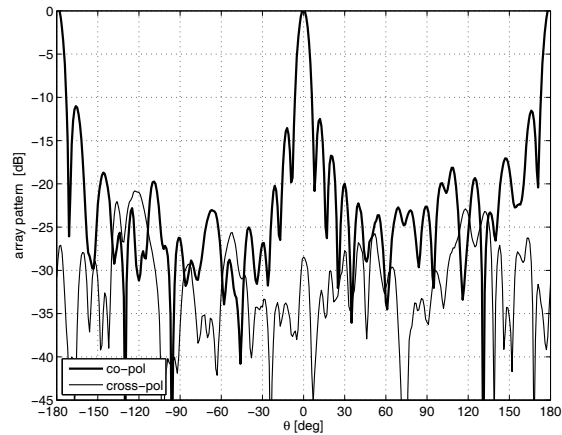
Upon focusing on 3 representative frequencies, the measured co- and cross polar radiation patterns at 8 GHz, 10 GHz and 12 GHz, respectively, are shown in Fig. 5.31. At least 25 dB difference is noticed between the co- and the cross polar components at the broadside direction ($\theta = 0^\circ$) at all the frequencies.

UWB scanning performance assessment In this section the scanning performances of the array depicted in Fig. 5.25 will be investigated. As mentioned before, the center-to-center spacing of two consecutive elements is 14 mm, corresponding to 0.56λ at 12 GHz. According to Eq. (2.3) the grating lobes appear after $\vartheta_0 = 51.8^\circ$ scanning angle.

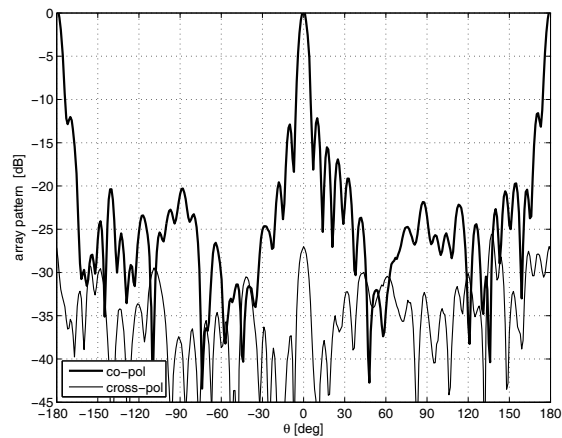
The radiation patterns are obtained by means of a MATLAB post-processing that performs the summation of the measured antenna elements patterns, upon accounting for the phase shifts needed for steering the beam



a



b



c

Figure 5.31: Normalized radiation patterns (in decibels) corresponding to the $\{\phi = 0^\circ; \phi = 180^\circ\}$ cut, for 3 characteristic frequencies ((a) at 8 GHz (b) at 10 GHz and (c) at 12 GHz) : thick line – co-polar component; thin line – cross polar component.

in the desired direction. This radiation pattern synthesis is justified by the measurement methodology which calibrates all the antenna ports to the same magnitude and phase plane. Hence, the required phase at each antenna port to steer the beam into a certain direction is added to the complex radiation patterns of the individual radiators in the post-processing of the data.

To begin with, the radiation patterns of the 15 elements were measured, 3 representative such patterns being shown in Fig. 5.32 for the elements 1, 2 and 7, respectively. When compared with the corresponding radiation pattern of the *isolated* element (see Fig. 3.21 (a)) the results in Fig. 5.32 show the drastic effect of including the elements in array environments. In the case of the *edge* elements, namely 1 and 2, the omnidirectional behaviour evolves into a pattern having a “main beam” and a very pronounced notch at about $\theta = 52^\circ$. Upon comparing Fig. 5.32 (a) and (b), it is evident that the outline of the “main beam” becomes clearer as moving towards the center of the array. It is interesting to notice the appearance of a second notch in Fig. 5.32 (b) at approximately 124° . When moving to Fig. 5.32 (c), corresponding to the center element, a clear “main beam” can be identified. This focusing properties present in the radiation patterns of *individual elements* can only be understood when accounting for the array environment. More specifically, the isolated elements have omnidirectional patterns. Nonetheless, in the array, these patterns intersect the neighbouring elements that collectively constitute a periodic, conductive structure. Obviously, the effect of these structures is different for the edge elements, “seeing” an asymmetric configuration, and for the center element, placed in a symmetric environment. The waves launched by the radiator travel along these structures and are eventually, radiated at the edges, with part of the energy being diffracted underway. The fact that the structure formed by the neighbouring radiators is periodic suggests that the effect on the radiation patterns is frequency dependent. This was indeed observed in measurements effectuated at other frequencies that are not reported in this account for reasons of brevity.

Another remarkable feature of the patterns displayed in Fig. 5.32 is that the front and the back lobes are not symmetric. This difference is mainly ascribed to the dielectric backing of the array. Again, at variance with the case of the isolated element, the wave launched along the periodic structure has as a secondary effect the radiation of a leaky wave at the back air to dielectric interface.

The measured elementary radiation patterns of all 15 radiators are now combined for obtaining the radiation pattern of the array. This characteristic is displayed in Fig. 5.33 at 3 different scanning angles (i.e. $\vartheta_0 = 30^\circ$, $\vartheta_0 = 51.8^\circ$ and $\vartheta_0 = 65^\circ$). All the radiation patterns in these plots are normalized

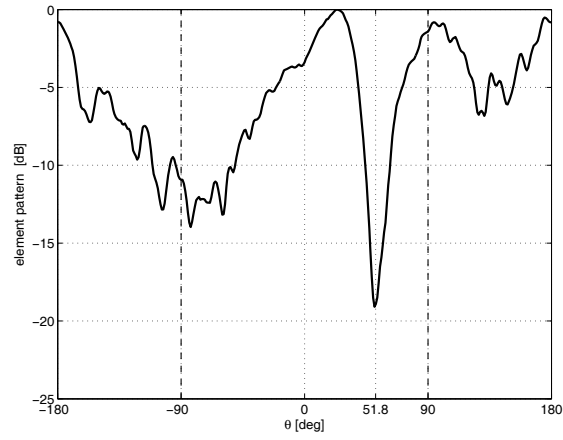
with respect to the maximum of the case where the array is scanned to the broad side direction ($\vartheta_0 = 0^\circ$). The main purpose of this study is to verify the array’s scanning performance, with a special attention being paid to the onset of *grating lobes* and to possible *scan blindness*⁶ effects.

The bi-directional element pattern gives rise to the bi-directional array pattern which can be observed in all plots as two main lobes symmetrical with respect to $\theta = 90^\circ$. In Fig. 5.33 (a) the maximum of the radiation pattern appears at approximately $\vartheta = 30^\circ$. The radiation pattern has another maximum around $\vartheta = 150^\circ$, these two maxima being symmetric with respect to $\theta = 90^\circ$. The main beams of the radiation pattern appear around $\theta = 51.8^\circ$ and $\theta = 128.2^\circ$ in Fig. 5.33 (b) where a grating lobe appears at $\theta = -90^\circ$. Two such grating lobes, symmetrical with respect to $\theta = -90^\circ$, can be observed in Fig. 5.33 (c) due to the same reason explained above. In this case the main beams appear at $\theta = 65^\circ$ and $\theta = 115^\circ$. An interesting phenomenon is observed in Fig. 5.33 (b). The level of the grating lobe which appears at $\theta = -90^\circ$ is greater than the level of the main beams which appear around $\theta = 51.8^\circ$ and $\theta = 128.2^\circ$.

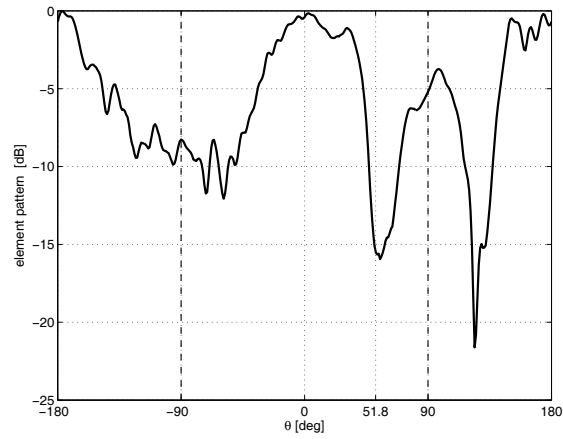
After examining the elementary radiation patterns depicted in Fig. 5.32, it is then clear that the array patterns can deviate a lot from the array factor. This is exactly the case when scanning at $\theta_0 = 51.8^\circ$, Fig. 5.32 indicating differences between -8.16 dB and -6 dB between the levels at $\theta = 51.8^\circ$ and $\theta = -90^\circ$, respectively. These differences directly reflect in the approximately 5 dB lower main beams, when compared to the grating lobe at $\theta = -90^\circ$ (see Fig. 5.33 (b)).

The dips observed in Fig. 5.32 around $\theta_0 = 51.8^\circ$ can be associated with the scan blindness phenomenon. Fig. 5.34 shows the scanning angle dependence of the loss in the radiated power with respect to the broadside radiation case, which clearly presents the onset of the scan blindness around $\theta_0 = 52^\circ$ and $\theta_0 = 69^\circ$. Thus, the steep increase in the scan loss coincides with the similarly steep decrease in the individual elementary radiation patterns that can be seen in Fig. 5.32.

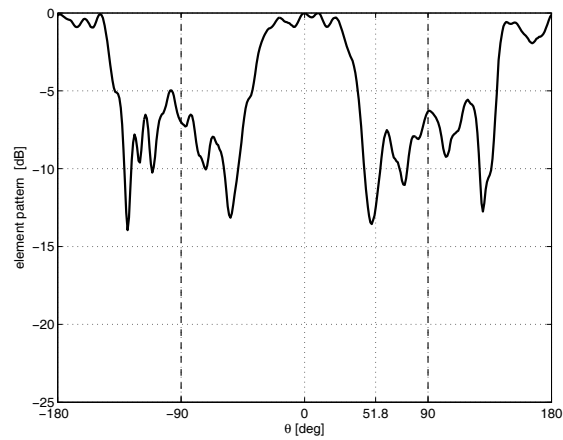
⁶The cancellation of all radiation for certain scan directions [57, p. 26].



a

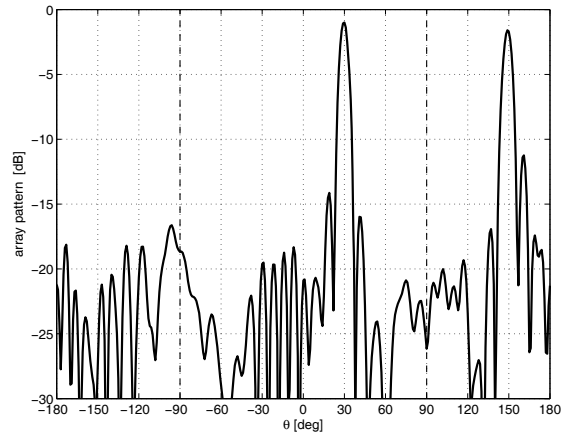


b

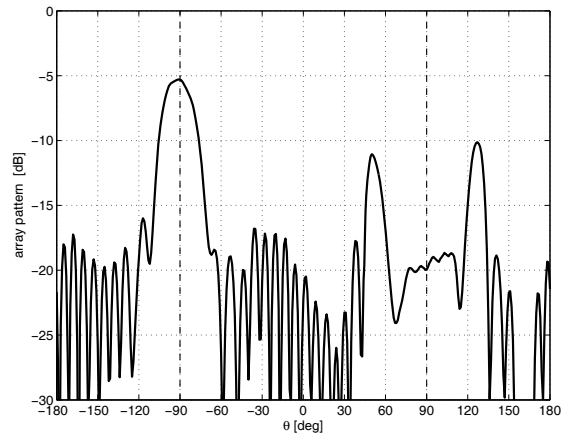


c

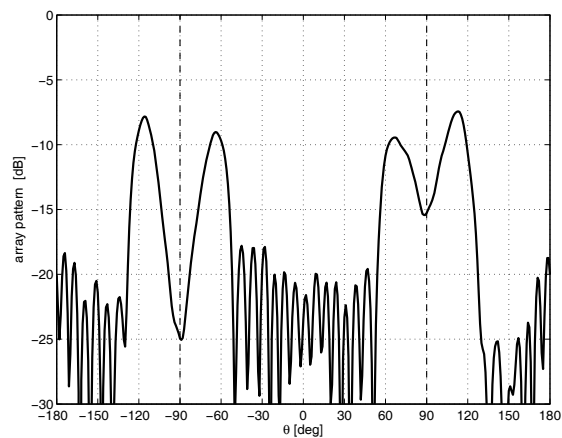
Figure 5.32: Measured element radiation patterns at the $\phi = 0^\circ$ cut and 12 GHz frequency for: (a) first array element; (b) second array element; (c) seventh array element.



a



b



c

Figure 5.33: Measured radiation patterns at $\phi = 0^\circ$ cut and 12 GHz frequency for: (a) $\vartheta_0 = 30^\circ$; (b) $\vartheta_0 = 51.8^\circ$; (c) $\vartheta_0 = 65^\circ$.

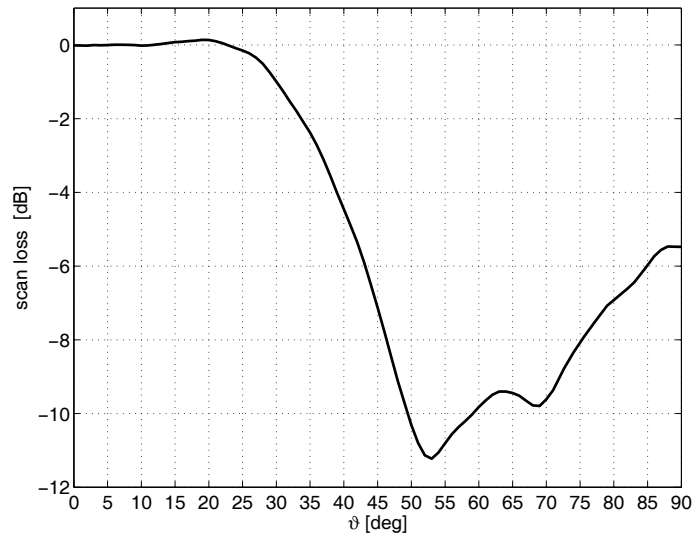


Figure 5.34: Scan loss curve of the array at 12 GHz.

5.3 Conclusions

In this chapter the linear array performances of two antennas introduced in Chapter 3 are explored in detail. Firstly, the “Tulip” loop antennas are integrated in a linear array composed of 4 elements. The mutual coupling between the elements is reduced by including slot rows between the elements. This novel technique allows reducing the mutual coupling without increasing the distance between the elements. In the second part of this chapter, “Eared” antennas are investigated in linear arrays of 7 and 15 elements. The approximation rules derived in the case of the 7 element linear array are used to predict the performances of the linear array composed of 15 elements. These results are confirmed via measurements.

It can be concluded that the “Eared” antenna is more suitable for array environments compared to the “Tulip” loop antenna. This is firstly due to the “Eared” antenna’s confined fields, whereas for the “Tulip” loop antenna, some mutual coupling mitigation methods should be called upon. Besides, the length of the feed section for the “Eared” antenna can be extended without any deterioration in the reflection and the radiation characteristics of the antenna. However, the antenna shape (i.e. the tuning stub) should be modified to make the electrical characteristics satisfactory in case of the extension of the feed lines of the “Tulip” loop antenna.

Elements of novelty

The primary novelties presented in this chapter are listed as follows:

- The UWB “Tulip” loop antenna is successfully integrated in linear array environments and the elements are successfully modified such that they have low mutual coupling with the neighboring elements. The array has an operational impedance bandwidth for $VSWR \leq 2$ which stretches between 7 GHz and 14 GHz corresponding to a fractional bandwidth of 67%. The radiation patterns of the array are also stable within this range.
- The UWB “Eared” antenna is successfully embedded in the linear array environments and in this way it was proven that these elements are suitable for being used in linear array environments. The array has a wide impedance bandwidth and stable radiation patterns. The simulations and the measurements prove that the magnitude of the reflection coefficient corresponding to $VSWR \leq 2$ starts at 8 GHz and goes beyond 15 GHz. It was also noticed that this value has to be corrected by accounting for the possibility of grating lobes being onset. Since the electrical spacing between the individual elements becomes 0.5λ for $f = 10.7$ GHz, with λ denoting the free space wavelength, the impedance bandwidth of the array turns out to be 29% for a full scanning condition.
- A novel method is developed in order to predict the performances of large arrays from simulations and measurements of smaller arrays. Thus, the performances are well predicted without doing lengthy simulations or, the more so, measurements.

Chapter 6

Suitability of antenna elements to Impulse Radio applications

Chapter 1 states that the design of the low-profile, electrically small-sized and wide impedance bandwidth antenna elements concentrated firstly on the X-band as this research is effectuated within the frame of the WISE project. Therefore the elements developed in Chapter 3 cover the frequency range of the X band. The goal of this chapter is demonstrating the use of these elementary radiators for Impulse Radio (IR) applications. Thus the elements should be re-designed so that they can be used in the FCC UWB frequency band stretching between 3.1 GHz and 10.6 GHz. Particularly, the “Eared” antenna will be re-designed in such a way that it covers the whole frequency range. All predicted electrical performances of the antenna are confirmed via measurements. The time-domain performance of the antenna is investigated by measuring the group delay. This chapter is concluded by a short summary and by cataloging the novelties in it.

6.1 Readily available solutions to full IR UWB band coverage

It is possible to find various antennas in the literature covering the UWB frequency range stretching between 3.1 GHz and 10.6 GHz, as the UWB technology has gained much popularity in the recent years. To the author’s knowledge, these antennas have some deficiencies. Some of these antennas

are electrically large, so it is difficult to use them in array environments and some of them have acceptable time domain behaviors up to a limited frequency, only. For example, the circular slot antenna investigated in [14] has a width of more than 29 mm, corresponding to 0.64λ at the central frequency of the UWB band (6.6 GHz), which makes it difficult to use this antenna in array environments. Similarly, a planar bell-shaped antenna investigated in [69] has the same electrically big size problem; the maximum size of the antenna is 86 mm which corresponds to 0.89λ at 6.6 GHz. Although there are other radiators that are electrically small, their time-domain behavior is not satisfactory over the entire frequency band. In [20], it is stated that the group delay of the thereby advocated antenna is good up to 7 GHz. Similarly, [36] introduced a radiator, the group delay of which has variations that are below 5 ns up to 7 GHz; however between 7 and 8 GHz these variations are up to 15 ns and the group delay within the rest of the frequency band is not even stated.

In the following, this chapter proceeds to offering a solution to mitigating the shortcomings enumerated above by proposing a radiator that effectively addresses the stringent requirements in the realm of IR.

6.2 IR UWB antenna design

6.2.1 Design philosophy

Chapter 3 discussed a radiator displaying remarkable UWB performance, namely the “Eared” antenna (see Fig. 6.1) that is deemed as a valid starting point for the design of the desired IR UWB antenna. The radiator was designed in Chapter 3 for covering the X-band, the corresponding values being summarized in Table 3.1. Obviously the “Eared” antenna needs to be re-tuned for accommodating the IR band.

Firstly, it is noted that non-linearities in the phase curve, a clearly undesirable feature in the case of time-domain antennas, are associated with (sharp) dips in the return loss frequency dependence. It then follows that an overall balance in this frequency characteristic, rather than extreme impedance matching bandwidth, is the preferred starting point in designing the intended IR UWB antenna. With reference to the “Eared” antenna discussed in Chapter 3, two variants were presented: the one depicted in Fig. 3.8, having a measured operational impedance bandwidth for $VSWR \leq 2$ stretching from 5.11 to 20 GHz, and the one shown in Fig. 3.19, having an impedance bandwidth stretching from 5 to 45 GHz. The relevant return loss frequency behaviors in the $5 \div 20$ GHz range are now collected in

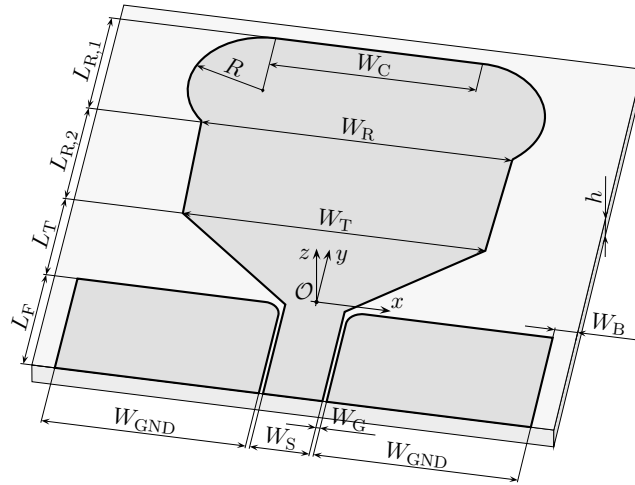


Figure 6.1: Configuration of the proposed CPW-fed, quasi-magnetic antenna.

Fig. 6.2, with “antenna 1” denoting the former of these two variants.

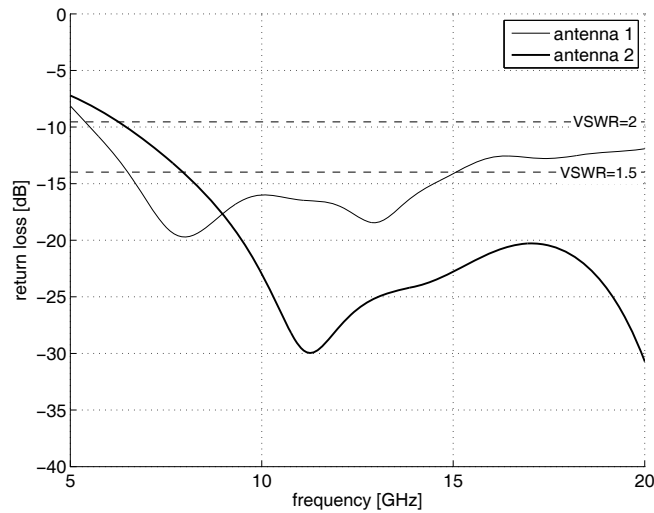


Figure 6.2: Frequency dependence of the return loss for “antenna 1” and “antenna 2”.

Although “antenna 2” displays a better impedance matching over an obviously broader range, the return loss characteristic of “antenna 1” is clearly flatter. Then, by invoking the argument above referred to, the “antenna 1” variant will be further dealt with in this chapter. Moreover, the frequency

band 6 to 20 GHz¹ will be taken as a reference in the reasoning to come.

A second conducive observation in the process of redesigning the “Eared” antenna is that the design frequency for this X-band antenna was 9 GHz, that is located close to the limit of the first quarter of the reference operational bandwidth. By keeping the same ratios in the case of the IR band, namely $3.1 \div 10.6$ GHz, the corresponding design frequency is approximately 4 GHz, this yielding a factor of $9/4 = 2.3$. By invoking a linear dependence of antenna dimensions with frequency, all dimensions in Table 3.1, except for the ones related to the feeding part, i.e. W_S and W_G , are initially multiplied by 2.3. These dimensions will then be subject to an optimization strategy in which the insight accumulated in the process of designing the “Eared” antenna will be efficaciously employed. The dimensions resulting after the up-scaling are summarized in Table 6.1.

Table 6.1: Initial geometric parameters of the IR UWB “Eared” antenna.

Parameter	Dimension [mm]	Description (see Fig. 6.1)
L_F	9.775	Length of the feed section
W_{GND}	15.778	Width of the ground
W_S	2	Width of the signal line
W_G	0.14	Width of the CPW’s gap
L_T	3.772	Tapering length in transition region
W_T	23.46	Upper tapering length in transition region
$L_R =$ $L_{R1} +$ L_{R2}	19.964	Resonator length in radiating region
W_R	24.15	Resonator width in radiating region
W_C	16.1	Circle’s separation width
R	5.75	Radius of top circular areas

Note that the L_T dimension was re-optimized in Section 3.2.3, its value being decreased with 2 mm with respect to the one quoted in Table 3.1.

¹The operational impedance bandwidth of the “antenna 1”.

Consequently, the optimized value of L_T , namely 1.64 mm, is used as a basis for the corresponding scaled quantity in Table 6.1.

6.2.2 Determination of the antenna dimensions

Chapter 3 highlighted the dimensions that play an important role in the performance of the antenna. It was shown there that the most important dimensions are L_T , W_T and L_{R2} (see Fig. 6.1). Consequently, the tuning of the IR UWB antenna will focus in a first stage on these dimensions. Additional improvements will subsequently be obtained by adjusting some of the remaining dimensions, as well. Note that all effectuated numerical experiments employed, deliberately, the same total bulk size $2W_{GND} + 2W_G + W_S = 33.8$ mm, with the dimensions W_{GND} , W_G and W_S being specified in Table 6.1.

Effect of the L_T dimension

Since the L_T dimension for the new antenna was calculated by using its optimized value obtained in Chapter 3, it was expected that $L_T = 3.772$ mm, the value tabulated in Table 6.1, would give the best result in terms of impedance bandwidth. However a brief parametric study has been performed around this value in order to be sure that the value is, indeed, optimal. The frequency dependence of the return loss for different values of the transition region's length is depicted in Fig. 6.3. Here, $L_{T,0}$ designates the value of the L_T parameter as stated in Table 6.1. This length seems to be optimal, however the frequency band between 7 GHz and 12 GHz should still be improved by tuning the other parameters such as W_T and L_{R2} .

Effect of the W_T dimension

Since the current density is maximum around the transition region of the antenna, the W_T dimension, which controls the width of the transition region between the feeding and radiation sections, is also an important parameter influencing the performance of the antenna. The parameter study depicted in Fig. 6.4 yields the conclusion that the optimum value for the width of the upper tapering length in the transition region is $W_T = W_{T,0} - 6$ mm. Here, as with $L_{T,0}$, the parameter $W_{T,0}$ shows the value of the W_T parameter that was stated in Table 6.1. It can be noticed that the unbalanced part between 7 GHz and 12 GHz in Fig. 6.3 starts to be more balanced at the cost of trading-off the very low return loss above 12 GHz. One can still

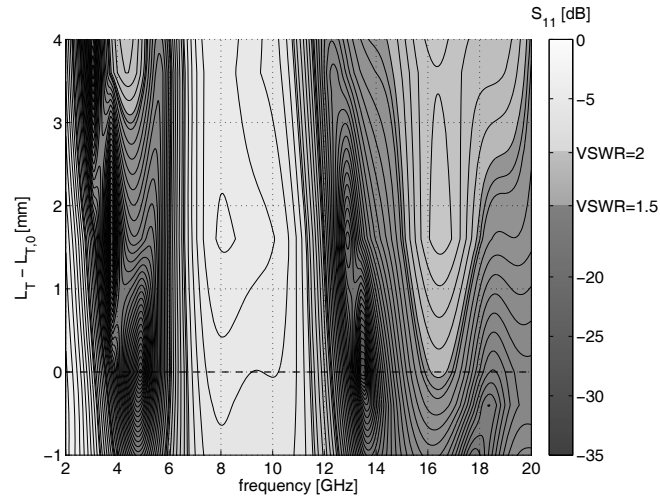


Figure 6.3: Frequency dependence of the return loss for different values of the transition length L_T .

notice that a small frequency region around 10 GHz needs further attention for improving the impedance bandwidth around the mentioned frequency.

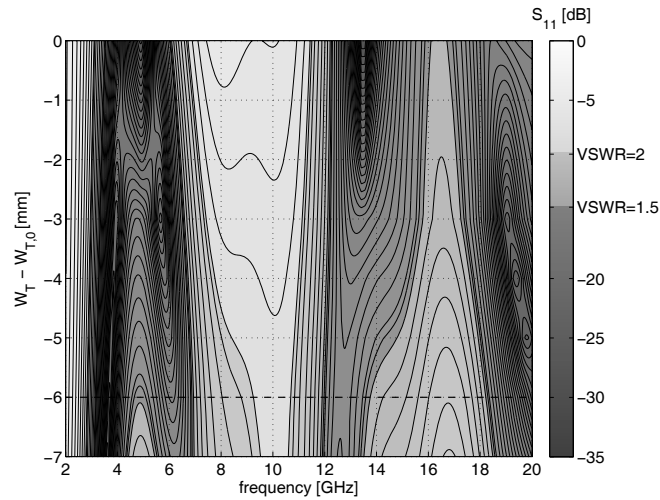


Figure 6.4: Frequency dependence of the return loss for different values of W_T , the upper tapering length of the transition region.

Effect of the L_{R2} dimension

After fixing W_T to 17.46 mm, the effect of L_{R2} is then investigated. The frequency dependence of the return loss for different values of the resonator length of the radiating region L_R is shown in Fig. 6.5. From this figure, it can be derived that decreasing this dimension by 3 mm results in a better impedance matching. Now it can be seen that the frequency dependence of the return loss gives a more balanced impedance bandwidth.

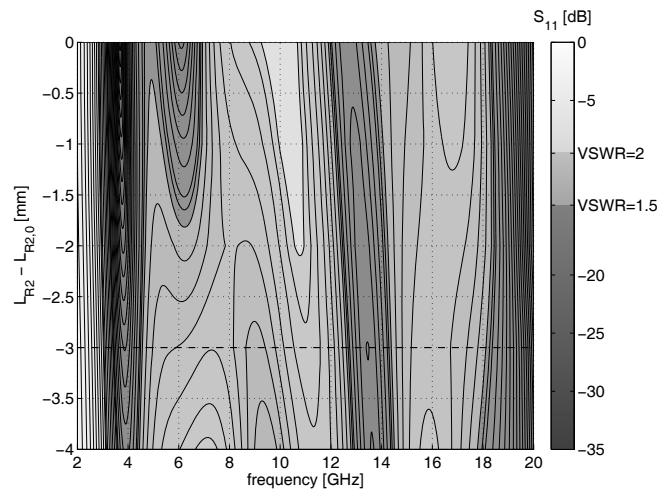


Figure 6.5: Frequency dependence of the return loss for different values of L_{R2} , the resonator length of the radiating region.

Modifications of the other parameters

Although the impedance bandwidth obtained as a result of the study described above and depicted in Fig. 6.5 ($L_{R2} - L_{R2,0} = -3$ mm) gives the essential impedance bandwidth for the required application; other dimensions, such as W_R , W_C and R , are also modified by means of a parameter study in order to decrease the size of the antenna. The result of this study is depicted in Fig. 6.6. In this picture “antenna 3” denotes the antenna obtained as a result of the parameter study on L_{R2} and “antenna 4” indicates the antenna with W_R , W_C and R values being all reduced by 6 mm. From this figure, it can be derived that decreasing W_R , W_C and R by 6 mm maintains good impedance matching while providing a considerable bulk size reduction.

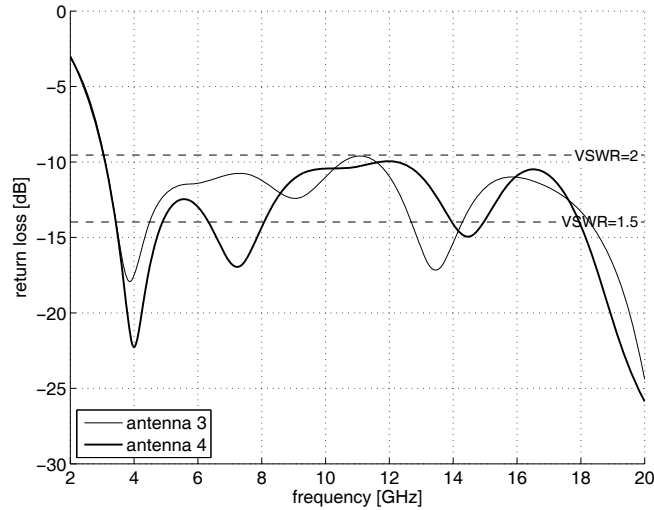


Figure 6.6: Frequency dependence of the return loss for “antenna 3” and “antenna 4”.

Effect of the ground width reduction on the antenna performance

A final test concerned the limit up to which the ground width W_{GND} can be reduced without degrading the antenna performance. This investigation was intended as a preparatory study in anticipation of the inclusion of this antenna in array environments, in which case the total antenna width plays a crucial role. This experiment was carried out by keeping the dimensions W_{G} and W_{S} constant, a choice dictated by the need to preserve the CPW transmission line properties. The numerical experiments have shown that the total width of the antenna ($2W_{\text{GND}} + 2W_{\text{G}} + W_{\text{S}}$) can be safely reduced up to 28 mm, a dimension that was then used for fabricating the device.

Manufactured antenna

As reported previously, in view of allowing a time-domain de-embedding of the effect of soldering and of the connectors to CPW line transitions, the CPW length was extended up to a total of 65 mm. The fabricated antenna is depicted in Fig. 6.7 and the final dimensions are summarized in Table 6.2.

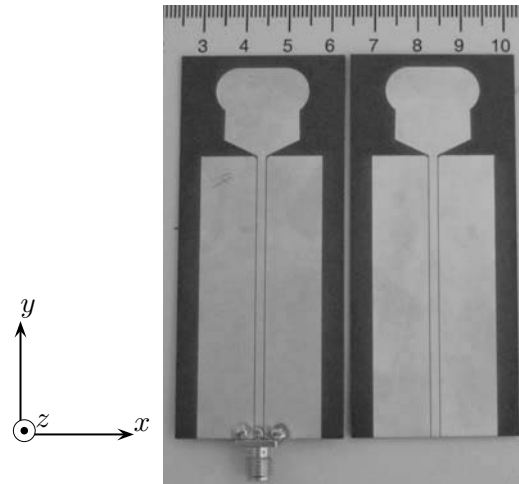


Figure 6.7: The IR UWB “Eared” antenna, with and without the pertaining SMA connector.

6.3 Frequency domain validation

6.3.1 Scattering parameter measurements

The simulated and the measured results corresponding to the antenna shown in Fig. 6.7 are depicted in Fig. 6.8. Similarly to the measurements discussed in Chapter 3, the time-domain de-embedding technique was used in order to eliminate the soldering and connector effects. The simulated and the measured data indicate an operational impedance bandwidth for $VSWR \leq 2$ of 169.7%, stretching over the frequency range starting at 2.7 GHz and ending at 33 GHz, the latter value being chosen due to the fact that it represents the upper limit of the operational band of the employed connector. The measured and the simulated results show considerable similarity.

6.3.2 Radiation pattern measurements

After performing the scattering parameter measurements, the radiation patterns of the antenna have been investigated. The radiation patterns were measured between 2 ÷ 20 GHz. The antenna was placed on the xOy – plane as seen in Fig. 6.7 and the radiation patterns were measured in the principal planes of the antenna (the xOz –, the yOz – and the xOy – planes). The

Table 6.2: Geometric parameters of the IR UWB “Eared” antenna.

Parameter	Dimension[mm]	Description (see Fig. 6.1)
L_F	64	Length of the feed section
W_{GND}	28	Width of the ground
W_S	2	Width of the signal line
W_G	0.14	Width of the CPW's gap
L_T	3.772	Tapering length in transition region
W_T	17.46	Upper tapering length in transition region
$L_R =$ $L_{R1} +$ L_{R2}	16.96	Resonator length in radiating region
W_R	18.15	Resonator width in radiating region
W_C	10.1	Circle's separation width
R	5.55	Radius of top circular areas

radiation patterns at 3.5, 6 and 9.5 GHz are presented in this section.

xOz – plane ($\phi = 0^\circ$ cut) radiation patterns

The radiation patterns corresponding to the $\phi = 0^\circ$ cut are depicted in Fig. 6.9 at the above indicated frequencies. The antenna shows omnidirectional characteristics, however towards the high frequencies (i.e. at 9.5 GHz) the radiation pattern starts showing distinct irregularities. The co- to cross-polar ratio is very good, around the middle of the frequency band (i.e. at 6 GHz) this ratio is more than 24 dB.

yOz – plane ($\phi = 90^\circ$ cut) radiation patterns

The radiation patterns corresponding to the $\phi = 90^\circ$ -cut of the antenna are depicted in Fig. 6.10. The co-polar radiation pattern displays a deep notch

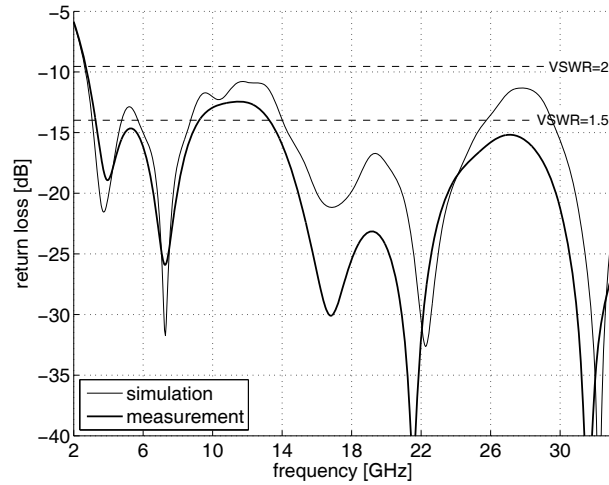


Figure 6.8: Simulation and measurement results concerning the final optimized IR UWB “Eared” antenna.

for $\theta = 90^\circ$ and $\theta = 270^\circ$. Theoretically, no cross polarization components can be observed in this cut since on the symmetry axis of the antenna all cross polar components cancel out each other. In a real case scenario, some cross polar components are observed, their level being, nonetheless, extremely low.

xOy – plane (θ cut) radiation patterns

The radiation patterns corresponding to the θ -cut of the antenna are shown in Fig. 6.11. The co-polar radiation pattern displays a deep notch for $\phi = 90^\circ$, i.e. along the symmetry axis of the antenna.

Radiation patterns at higher frequencies

It has been shown that the radiation patterns are stable within the frequency band stretching from 3.1 to 10.6 GHz. In order to give an idea about the behavior of the antenna at higher frequencies, the radiation patterns at 15 GHz are depicted in Fig. 6.12. It can be noticed that the omnidirectionality is clearly perturbed and the radiation pattern has a high cross-polar component, as seen in Fig. 6.12(a). Figure 6.12(b) shows the pattern in the xOz – plane of the antenna; even if we observe the null at $\theta = 90^\circ$, the pattern develops a lobed structure with a 6 dB depression separating the lobes around $\theta = 40^\circ$ and $\theta = 140^\circ$. The pattern deterioration in the xOy – plane is more visible as can be derived from Figure 6.12(c).

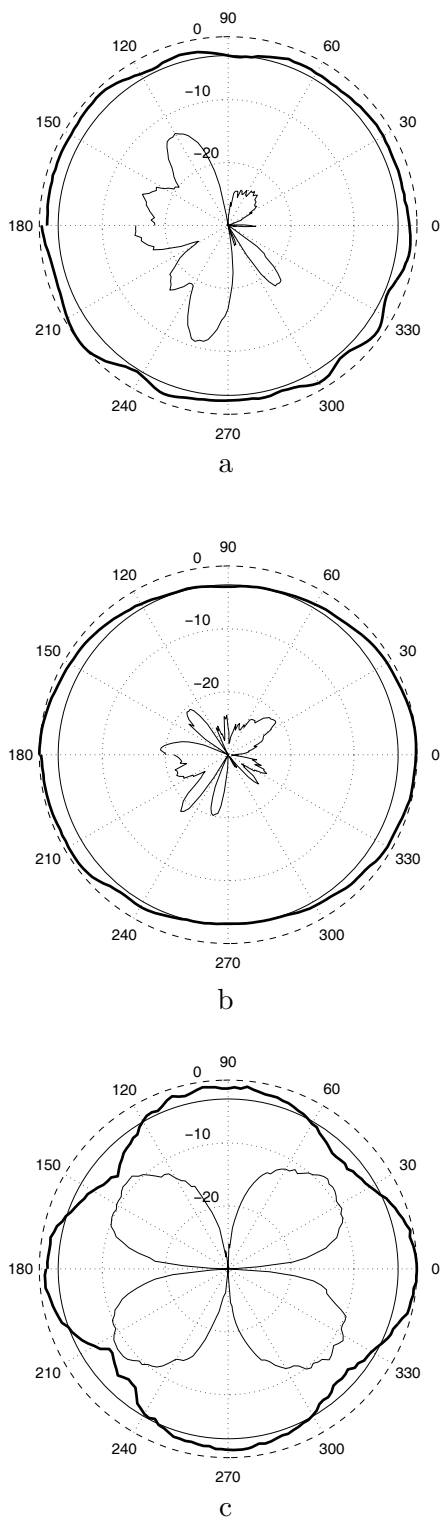


Figure 6.9: Measured radiation patterns concerning the final optimized IR UWB “Eared” antenna at the $\phi = 0^\circ$ cut (a) 3.5 GHz; (b) 6 GHz; (c) 9.5 GHz: thick line – co-polar component; thin line – cross-polar component.

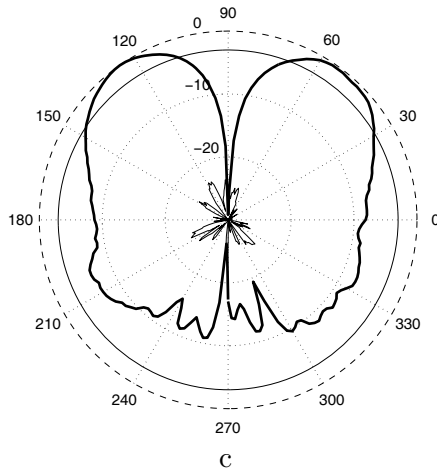
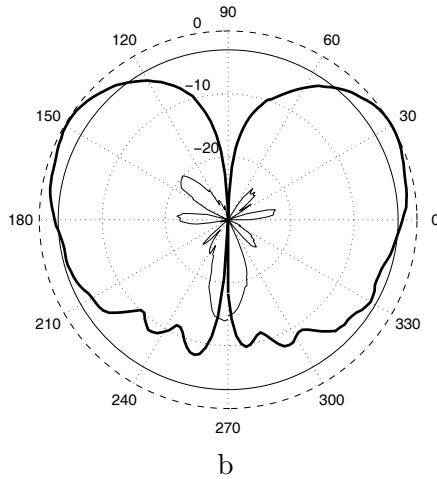
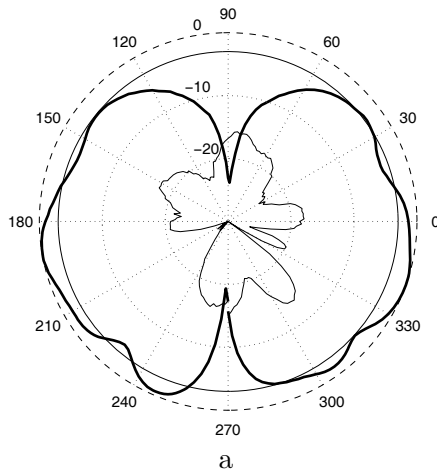


Figure 6.10: Measured radiation patterns concerning the final optimized IR UWB “Eared” antenna at the $\phi = 90^\circ$ cut(a) 3.5 GHz; (b) 6 GHz; (c) 9.5 GHz: thick line – co-polar component; thin line – cross-polar component.

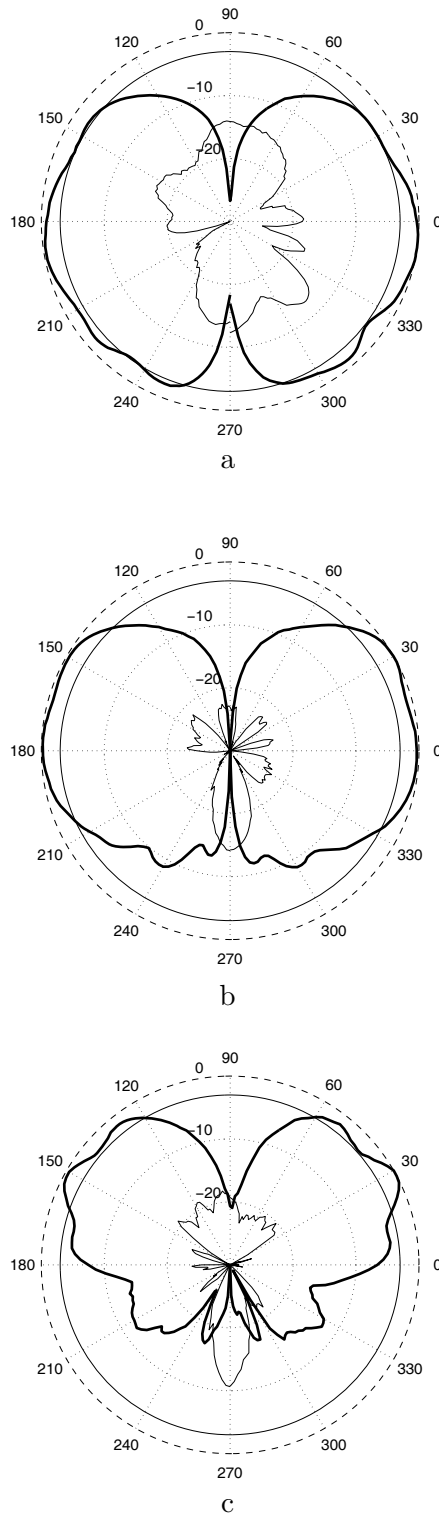


Figure 6.11: Measured radiation patterns concerning the final optimized IR UWB “Eared” antenna at the $\theta = 85^\circ$ cut(a) 3.5 GHz; (b) 6 GHz; (c) 9.5 GHz: thick line – co-polar component; thin line – cross-polar component.

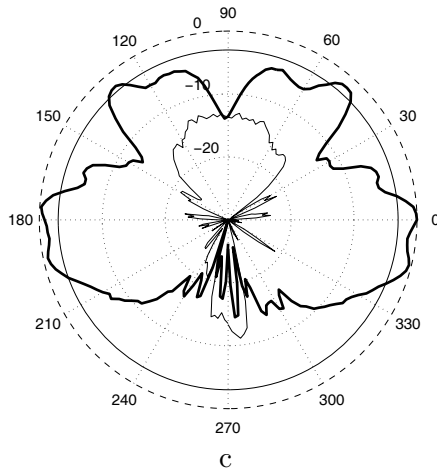
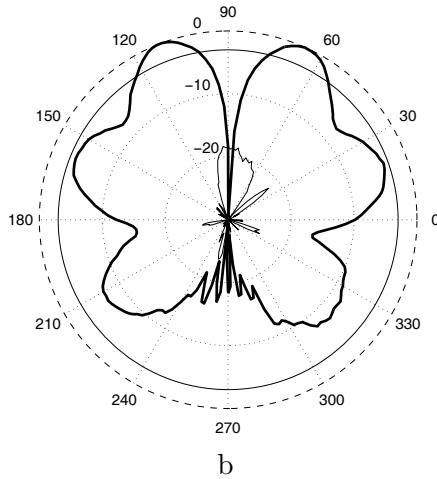
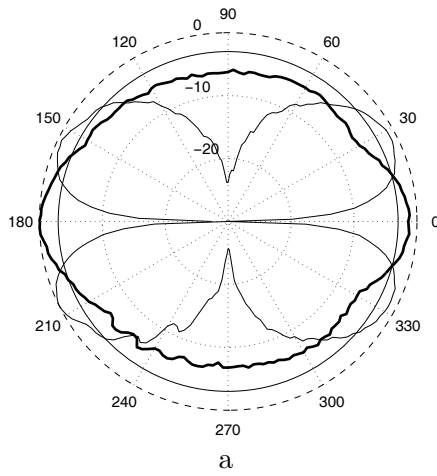


Figure 6.12: Measured radiation patterns concerning the final optimized IR UWB “Eared” antenna at 15 GHz for the (a) $\phi = 0^\circ$ cut; (b) $\phi = 90^\circ$ cut; (c) $\theta = 85^\circ$ cut: thick line – co-polar component; thin line – cross-polar component.

6.4 Time-domain validation

Section 6.3 has demonstrated that the antenna exhibits impedance matching following the FCC UWB characteristics, with nearly omnidirectional radiation patterns over the entire bandwidth. The time-domain behavior of the antenna should also be satisfactory for a well designed IR UWB antenna. In this section, the group delay of the antenna and the fidelity factor of an input signal satisfying the FCC regulations regarding the UWB are investigated based on experimental results. It is desirable for the group delay to be constant over the whole frequency bandwidth, otherwise the received signal may become distorted. Likewise it is desirable to have a fidelity factor close to 1 which indicates that the distortion on the pulse due to the antenna transfer function characteristics is limited.

6.4.1 System setup

All measurements are carried out inside the anechoic chamber. The antenna system consists of two identical IR UWB “Eared” antenna. The transmitter and receiver are placed at a distance of 3.5 meter in two different orientations, namely face-to-face² and side-by-side³.

6.4.2 Investigation of the group delay

For an antenna system consisting of one transmitter and one receiver antenna, the response of the system can be completely determined when the “transfer function” in the frequency domain is known [75]. The received signal is dependent on the transfer function of the system, in the discussed case this function being represented by S_{21} . The transfer function should have a linear phase response in the operational band in order to minimize the distortions in the received signal. The group delay dependence on frequency is defined as

$$\tau_g(f) = -\frac{\Delta\phi}{\Delta(2\pi f)}, \quad (6.1)$$

where τ_g is the group delay in nanoseconds, ϕ is the phase angle in radians and f is the frequency in GHz. This expression shows that the group delay

²The z axes of the antennas in Fig. 6.1 are aligned and the metalized surfaces are facing each other.

³The x axes of the antennas in Fig. 6.1 are aligned and the metalized surfaces are facing the same direction.

is a measure of the slope of the transmission phase response. Ideally, when the phase response of the transfer function is strictly linear, the group delay is constant, meaning that each frequency component is transmitted with the same delay. The degree of nonlinearity of the phase indicates the deviation of the group delay from a constant value.

Before calculating the group delay of the antenna under study, the phase response of the transfer function should be investigated and this characteristic is presented in Fig. 6.13. For both face-to-face and side-by-side examined combinations, the phase responses are remarkably linear over the entire operational band. Upon applying Eq. (6.1) to these results, the characteristics given in Fig. 6.14 are obtained. The group delay of the two cases are quite stable, with variations smaller than 2 ns up to 8 GHz and of about 4 ns above this frequency.

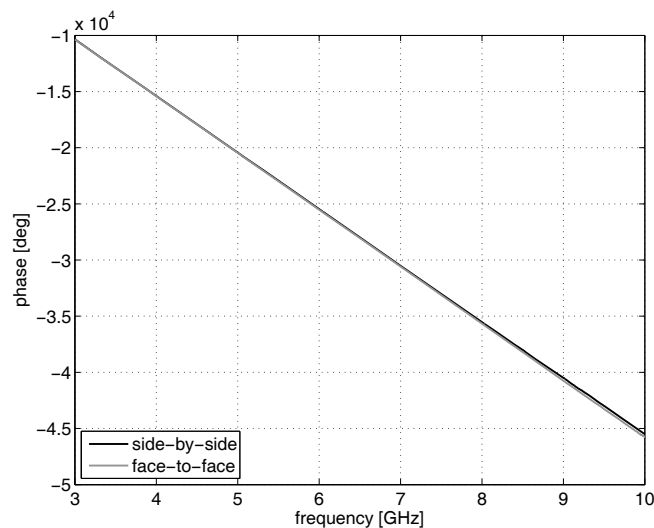


Figure 6.13: Measured phase concerning the transfer function of the UWB “Eared” antenna.

6.4.3 Investigation of the fidelity factor

Another metric for assessing the time domain behaviour of the antenna is the *fidelity factor* which is the correlation coefficient between the transmitted and the received signals. It demonstrates the similarity between two signals, in other words the amount of distortion that the antenna induces on the transmitted signal [3, 4], and it is calculated as:

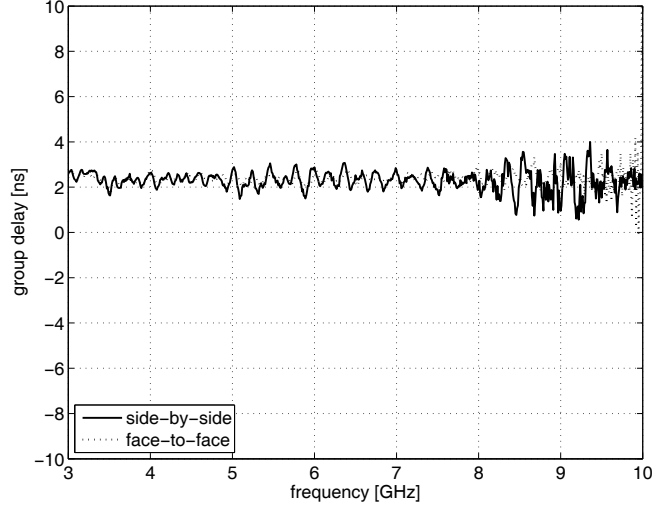


Figure 6.14: Measured group delay concerning the UWB “Eared” antenna.

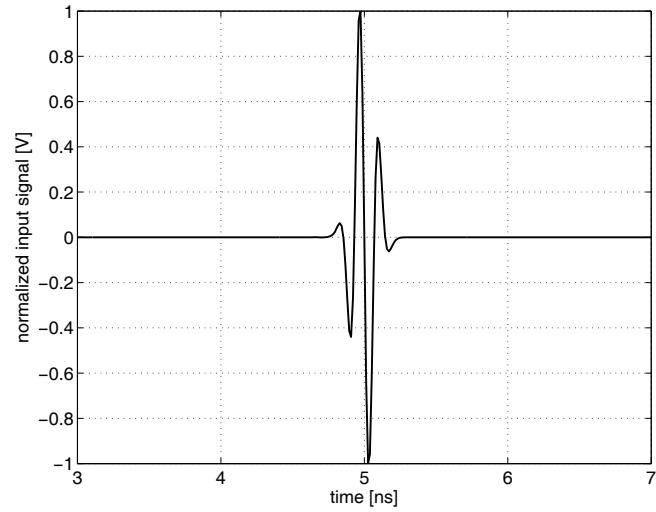
$$F = \max_{\tau} \frac{\int_{-\infty}^{\infty} s_t(t) s_r(t - \tau) dt}{\sqrt{\int_{-\infty}^{\infty} |s_r(t)|^2 dt} \sqrt{\int_{-\infty}^{\infty} |s_t(t)|^2 dt}}, \quad (6.2)$$

where $s_t(t)$ and $s_r(t)$ are the transmitted and the received pulses. The antennas are assumed to be excited by a UWB pulse which satisfies the FCC spectral mask for indoor systems. This signal, $s_t(t)$, is the 5th derivative of the Gaussian pulse given by [51]:

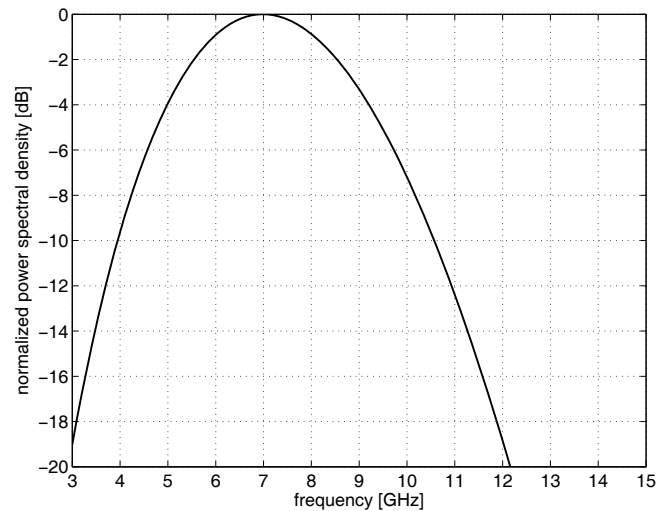
$$s_t(t) = A \left(-\frac{t^5}{\sqrt{2\pi}\sigma^{11}} + \frac{10t^3}{\sqrt{2\pi}\sigma^9} - \frac{15t^5}{\sqrt{2\pi}\sigma^7} \right) \exp\left(-\frac{t^2}{2\sigma^2}\right), \quad (6.3)$$

where A is the constant to meet the spectral power density limitations set by FCC and σ is taken as 51 ps to again satisfy the FCC limitations [51]. The normalized transmitted signal in time and frequency domains are depicted in Fig. 6.15. Fig. 6.15 (b) shows that the transmitted pulse has a bandwidth satisfying the FCC requirement (3.1- 10.6 GHz).

Then, the received pulse is calculated by convolving the transmitted signal, $s_t(t)$, with the transfer function of the antenna system. The received pulse is calculated for both face-to-face and side-by-side antenna configurations, the results being depicted in Fig. 6.16.



(a)



(b)

Figure 6.15: Antenna input signal, $s_t(t)$ in (a) time domain; (b) frequency domain.

The received pulses are similar to the input pulse with some distortions and ringing effects on them. It can be noticed that the fluctuations in the received pulse are more pronounced in the side-by-side case compared to the face-to-face case. This can be explained by the relatively less fluctuations in the group delay of the antenna for the face-to-face case in the whole FCC band (See Fig. 6.14). It can be concluded that non-linearities in the phase

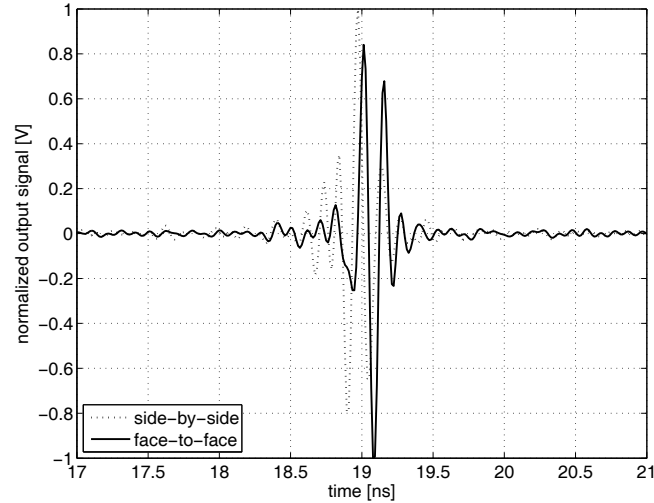


Figure 6.16: Antenna output signal, $s_r(t)$ in time domain.

curves of the transfer functions lead to some distortions in the received pulse. Another reason which causes dissimilarities between the received pulses is the difference between the magnitudes of the transfer functions, especially between 5 and 9 GHz. The fidelity factors are calculated by using Eq. (6.2) for face-to-face and side-by-side cases the corresponding values amounting to 0.93 and 0.88, respectively. Again, it can be noted that the configuration with group delay having less variation leads to better fidelity factor.

6.5 Conclusions

The “Eared” antenna was re-designed such that to cover (and largely exceed) the IR UWB frequency band starting at 3.1 GHz and ending at 10.6 GHz. All predicted results were confirmed via measurements. According to the measurement results, the antenna has an impedance bandwidth starting at 2.7 GHz and stable radiation patterns over the IR UWB frequency bandwidth with some stronger deterioration observed, only, towards the end of the frequency band of interest. The proper time-domain performance of the antenna was also certified by measurements and it was shown that the group delay of the antenna is almost constant ensuring, with smaller than 4 ns variations, very limited distortions in the received signal. This stable group delay guarantees an appropriate time-domain signal reception, with extremely limited distortions, as evidenced by in the calculations of the fidelity factors.

Elements of novelty

The primary novelties presented in this chapter are listed as follows:

- An IR UWB antenna has been successfully designed in order to make it cover the frequency band from 3.1 GHz to 10.6 GHz. The complete impedance bandwidth of this antenna reads 170%. The width of the radiator is 21.3 mm which corresponds to 0.47λ at the central frequency of the UWB band, i.e. 6.6 GHz. This radiator is one of the smallest antennas that has satisfactory time-domain performances (i.e. group delays), this making it appropriate for being included in array environments.
- The time-domain performance of this radiator turns out to be favorable, with group delay variations that are below 4 ns up to 9.98 GHz. This is better than most other antennas stated in the literature, such as the one reported in [36], having variations of group delay that are below 5 ns up to 7 GHz and 15 ns between 7 and 8 GHz.

Chapter 7

Conclusions

7.1 General conclusions and discussions

Presently, the topic of Ultra Wide-Band (UWB) antenna elements is a subject of intense investigation in the antenna research community. In view of many applications requiring beam shaping and scanning, this dissertation tackles the significantly less discussed topic of UWB *array antennas*, with an emphasis on low-profile, UWB antenna elements which can be embedded in such environments. The main objective of this research is expressed in the following research question:

How can one design optimal UWB elements for array environments?

The final product of this thesis is a robust set of design strategies for obtaining rugged, compact, low-profile and easily replicable antennas that can be used for Impulse Radio (IR) UWB applications, together with a number of exceptional devices falling in this category.

With direct application to UWB array antennas, in the first part of the thesis it was shown that the most important aspect for ensuring the UWB performance is having sufficiently small sized radiators, with satisfactory element bandwidths. The array bandwidth is likely to be determined by the element size rather than the element bandwidth because the element size determines how close the elements can be placed and, implicitly, the grating-lobes free operation. Thus, the key issue in designing the antenna elements for array environments is the antenna size. In order to develop a theory for small sized UWB elements, (quasi-) magnetic antennas were thoroughly examined in this dissertation. In this process formal definitions for “(quasi-) Magnetic” and “(quasi-) Electric” antennas were introduced,

this being one of the important contributions of the thesis.

The numerical evaluation of the performance of the isolated and array antennas was carried out, primarily, by using a commercial three-dimensional electromagnetic modeling tool, namely the finite-integration, time-domain CST Microwave Studio. Additionally, self-developed MATLAB scripts were used for post-processing of the computed and measured results.

By using the technological experience readily available within IRCTR and at its partners, a significant number of devices was produced. All manufactured samples were measured in the Delft University Chamber for Antenna Test (DUCAT). For ensuring the needed accuracy, a time-domain de-embedding technique was applied in the return-loss measurements for eliminating the artifacts in the produced demonstrators, such as extraneous reflections originating from soldering or from the employed connectors. Furthermore, a multi-port test-set was used for increasing the efficiency of array measurements.

The software resources, the technological insight and the accurate and effective experimental procedures were integrated in consistent and robust design methodologies that yielded radiators and arrays of a quality exceeding the state-of-the-art in the field.

Within the research question stated above, low-profile, quasi-magnetic antennas that are of dipole and loop types, examples of which are the “Eared” antenna and the “Tulip-loop” antenna, respectively, have been investigated thoroughly in the thesis. The working principles of these antennas can be extended for a large class of low profile “UWB antennas”. Due to its various advantages CPW feeding method was used for the design of all antennas. All antennas developed during this research are electrically small; however, they are different, especially in terms of their radiation mechanisms. When one looks at their working principles thoroughly it can be noticed that the dipole type antenna radiates mainly from its transition region that confines the electromagnetic fields into a limited area, this making the antenna inherently suitable for the arrays. Although the “Eared” antenna is electrically small (0.48λ at 12 GHz), when placed in linear array environments it requires some inter-element spacing to prevent electrical contact and reduce the mutual coupling. The increased spacing, in turn, brings back the grating lobes onset possibility. Thus, one should carefully balance the inter-element spacing by considering the grating lobes and mutual couplings in the array simultaneously. On the contrary, the loop type antenna radiates by means of the loop enclosing the tuning stub that is used to control the impedance matching. The size of the “Tulip-loop” antenna is 0.44λ at 12 GHz, hence a little smaller compared to the “Eared” antenna and, since this antenna

is enclosed by a loop, the radiators can be placed next to each other in an array. Despite its more reduced size when compared with the dipole type antennas, the loop type antenna is less suitable for arrays due to the higher mutual coupling levels that are associated with it. Moreover, when the loop type antennas are placed next to each other, since their ground planes are touching each other, there is an unwanted exchange of currents from one antenna to the other antenna. A novel technique, i.e. the inclusion of the equally spaced slots between the elements, has been introduced to allow the mitigation surface wave propagation. Note that this method also reduces the overall mutual coupling level. Application of these principles allowed obtaining “Eared” and “Tulip”-loop antennas having operational bandwidths for $VSWR \leq 2$ of 150 % and 70 %, respectively. To the author’s knowledge, these antennas have the widest impedance bandwidth with the electrically smallest size compared to other printed, low-profile antenna described in the literature. Moreover, the measured radiation patterns of these antennas are stable over the whole frequency band and they have low cross-polar components, especially around the design frequency.

Using the insight gained in the designing of isolated radiators, the antenna elements, initially developed for the X band were re-tuned for making them suitable for Impulse Radio applications. The dipole type of antenna, an example of which is the “Eared” antenna, was considered as a reference in order to design the new element working in the IR UWB frequency band. The final design characterised by an impedance bandwidth for $VSWR \leq 2$ of 170 %. The time-domain performance of the antenna has been shown to be most appropriate with variations that are smaller than 4 ns up to 9.98 GHz. To the author’s knowledge this is the smallest antenna, having the widest impedance bandwidth and proper time-domain characteristics compared to any printed, low-profile antenna described in the literature. There is still room to improve the time domain behavior of these antennas. When extreme dips are avoided in the return loss curves, a more linear phase curve of the return loss can be obtained. The negative derivative of this phase curve with respect to the frequency, i.e. the group delay, gives then better time domain performances.

The isolated antennas designed in this dissertation have “bi-directional” radiation patterns over the frequency band, making them good candidates for certain applications. However, since some applications require “uni-directional” radiation patterns, a feasibility study on adding a ground plane to be used in conjunction with the elementary radiators has been carried out. This study is also necessary for isolating the antenna when it is placed in the vicinity of conductive media. In this analysis, a loop type antenna has been used together with a properly designed Artificial Magnetic Conductor

(AMC). The preliminary study yielded an impedance bandwidth of 44%, that is better than that of similar structures reported in the literature.

As previously stated, the main objective of this work was designing novel antenna elements that can also be used in array environments and, thus it was crucial to investigate the array performances of the designed antennas. To this end, the loop type of antennas have been firstly integrated in a linear array consisting of 4 elements. Inclusion of slots between the antennas resulted in a satisfactory impedance bandwidth (i.e. for an $VSWR \leq 2$ of 67%) with stable radiation patterns. The array behavior of the dipole type of antennas has been also examined for linear arrays composed of 7 and 15 elements. It was proven that these elements are adequate for being used in linear arrays. The simulations and the measurements prove that the arrays have an operational impedance bandwidth for $VSWR \leq 2$ which starts at 8 GHz and goes beyond 15 GHz. The array investigations have been completed by developing a method to accurately predict the electrical performances of the large arrays by using the results of the smaller arrays. The performances of the large arrays could be well predicted without lengthy simulations and/or measurements. This method can be applied to any linear array. The validity of the method was confirmed via measurements.

7.2 Elements of novelty

The primary novelties presented in this dissertation are listed as follows:

- The rigorous definitions for the “(quasi-) Magnetic” and the “(quasi-) Electric” type antennas (Appendix B).
- The design of an UWB “Eared” antenna which has a relative bandwidth of more than 150% (Chapter 3). To the author’s knowledge, this antenna has the widest impedance bandwidth compared to any printed, low-profile antenna described in the literature.
- The design of a printed “Tulip” loop antenna which has an impedance bandwidth of 70% (Chapter 3). To the author’s knowledge, this antenna has the smallest electrical size for the mentioned impedance bandwidth compared to any printed, low-profile radiator found in the literature.
- The successful combination of the “Tulip” loop antenna and a simple, low-cost, but effective AMC (Chapter 4). Although high impedance

surfaces suffer from a limited impedance bandwidth, a quite satisfactory impedance bandwidth (i.e. 44 %) is obtained. The radiation patterns show smooth main lobes at broadside direction at low frequencies while dips appear gradually as the frequency increases.

- The UWB “Tulip” loop antenna is successfully integrated in linear array environments and the elements are successfully modified such that to have low mutual coupling with the neighboring elements. The array has an operational impedance bandwidth for $VSWR \leq 2$ which stretches between 7 GHz and 14 GHz, corresponding to a fractional bandwidth of 67%. The radiation patterns of the array are stable within this frequency range (Chapter 5).
- The UWB “Eared” antenna is successfully embedded in linear array environments. The array has a wide impedance bandwidth and stable radiation patterns. The simulations and the measurements demonstrate an operational bandwidth for $VSWR \leq 2$ starting at 8 GHz and going beyond 15 GHz (Chapter 5). The “Eared” antenna is an excellent candidate for functioning inside UWB, scannable, linear arrays.
- A novel method is developed in order to predict the performances of large arrays from simulations and measurements of smaller arrays. The performances are predicted accurately without the need for lengthy simulations or, the more so, measurements (Chapter 5).
- An IR UWB antenna has been successfully designed in order to make it cover the frequency band from 3.1 GHz to 10.6 GHz. The complete impedance bandwidth of this antenna amounts to 170%. This radiator is one of the smallest antennas that has satisfactory time-domain performances, this making it appropriate for being included in array environments (Chapter 6).
- The time-domain performance of the designed IR UWB radiator is extremely favorable, with group delay variations that are below 4 ns up to 9.98 GHz. This is far more superior than the other antennas reported in the literature (Chapter 6).

7.3 Future research

In this dissertation “UWB antenna elements that are appropriate candidates for array environments” have been studied in detail. A list of new directions to be investigated is hereafter catalogued:

- The study of the interaction between the dipole type bi-directional UWB (quasi-) magnetic antennas and the AMC planes in view of ensuring uni-directional radiation.
- The integration of the “dipole” type antennas and the “loop” type antennas in planar arrays, both with and without a ground plane.
- The antenna elements designed in Chapter 3 have linear polarizations. It would be extremely relevant to explore the possibilities to design low-profile, small sized, *dual polarized* or *circularly polarized* UWB elements. This can be achieved either at element and/or at array level.
- The integration of filtering structures into planar, CPW-fed and quasi-magnetic dipole type and loop type UWB antennas. This is essential for lowering the cost and minimizing the hardware. Some investigations have been already started on this issue; however, they still leave space for improvement. Band notch characteristics can be implemented by using the types of antennas presented in Chapter 3. For example, the dipole type antennas have been shown to have the feature of the currents being concentrated mainly at the edges. The fact that the current density is reduced in the central area of the radiators allows placing some slots in this region, the current perturbation introduced by such structures being, possibly, associated with filtering properties. Moreover, the fact that the radiation mechanism relies on the field concentration at the dipole neck, thus outside the area occupied by the slots, allows expecting a small impact on the extremely favorable radiation pattern characteristic of the “Eared” antenna.
- The placement of UWB (quasi-) magnetic dipole antennas and the “loop” antennas on conformal surfaces.

APPENDICES

Appendix A

Work embedding in IRCTR antenna research

The International Research Centre for Telecommunications and Radar (IRCTR) of Delft University of Technology initiated a major research programme in the antenna field in 2004 after 3 years of preparatory phase for the project. The project is called “Wide Band Sparse Element Array Antennas (WiSE)” and it is supported by the Netherlands Technology Foundation (STW) and (semi-) governmental and industrial organizations in the Netherlands. The Romanian Military Equipment and Technologies Research Agency (METRA) is the project partner from Romanian side and the Middle East Technical University (METU) from Turkish side. Both collaborators have been required to provide additional research performance to the project. One of the objectives of the WiSE project is to investigate and develop wide band elementary antenna radiators. The breakthroughs obtained during this investigation have laid the fundamentals for this thesis.

Appendix B

(Quasi-) magnetic antennas

Many different types of antennas, most of which of the electric type, have been investigated for UWB applications. In the framework of this thesis, own definitions of the author are employed for the electric and magnetic types of antennas. Before defining the electric and magnetic antennas, the definition of the base plane has to be clarified. The requirement for the field distribution to be concentrated in an area enclosed by the physical antenna structure on the base plane is also an integral part of the definition.

For *printed* antennas, the base plane can be defined as the plane where the antenna lies on, in other words, where the antenna is printed on. The definitions that will follow assume that most of the fields on the base plane are confined in an area practically surrounded by the physical structure of the antenna as in the case of the antenna defined in Paragraph 3.2.1. For this antenna, the fields concentrate more in the transition region of it and these fields are partly surrounded by the antenna physical structure.

Then, in the content of this work, the following definitions for electric and magnetic antennas are going to be used for 2.5-D, printed antennas. To begin with, an antenna for which the electric field lines are parallel to the base plane is referred to as a “magnetic” antenna. The distribution of the field lines is depicted in Fig. B.1 (a) for a magnetic antenna. Conversely, an antenna is referred to as “electric” when the electric field lines are orthogonal to the base plane. In other words, the magnetic field lines lie parallel to the base plane in the electric case. The distribution of the field lines is depicted in Fig. B.1 (b) for an electric antenna. In fact, the reader should note that the definition of a magnetic antenna is analogously evolved from the loop antenna - an example for a purely magnetic antenna- which tends to be more sensitive to magnetic fields passing through the loop area. In this

dissertation the design of (quasi-) magnetic antennas is one of the topics under investigation.

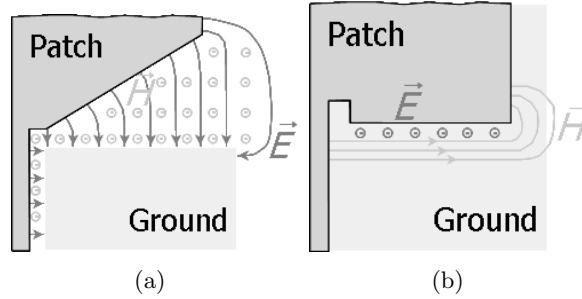


Figure B.1: Top view of (a) a (quasi-) magnetic antenna ; (b) an electric antenna

We can name the antenna defined in Paragraph 3.2.1 a *quasi* magnetic antenna. The term *quasi* comes from the following fact: In the transition region of the antenna the electric field lines are parallel while the magnetic field lines are perpendicular to the *base plane* as opposed to the microstrip antenna, which is an electric type of antenna where the electric fields are normal to the base plane. However since the antenna in Paragraph 3.2.1 consists of a metal region in the radiating part, the magnetic fields are not *allowed* to be perpendicular to the base plane which makes a discontinuity in the perpendicular direction of the magnetic field in the transition region of the antenna. It should be noted that, for a purely magnetic loop antenna, there is no discontinuity between the magnetic field enclosed by the loop itself.

Appendix C

Time-domain de-embedding techniques

The concept of the time gating method transforms the frequency-domain response into the time-domain via Fourier transform and filter out the time pulses which are caused by multi-path interferences by imposing a gating window [42, 49]. After this process, the signal can be re-converted to the frequency-domain via an inverse Fourier transform and a more accurate result can be displayed. Correct gating results in a significant improvement in the accuracy of the measurement. For example, this strategy was the key ingredient to ensuring the accuracy of the measurements reported in Chapter 3. With reference to the radiators examined in that chapter, namely the “Eared” Antenna and the “Tulip” loop Antenna, three principal types of spurious reflections needed to be suppressed by means of time gating:

- the first reflection, coming from the connector and soldering;
- the second one, coming from the antenna itself and
- the third one, coming from the surroundings of the antenna.

Placing a gate on the appropriate places suppresses all components that are not directly related to the antenna performance. The efficiency of the time de-embedding is demonstrated by the high level of similarity of simulation and measurement results reported in Figs. 3.9 and 3.33.

Appendix D

Array reflection coefficient synthesis

The configuration under study is presented in Fig. D.1. It consists of N radiators A_1, A_2, \dots, A_N that are fed individually via *ideal, reciprocal* phase shifters, providing the shifts β_1, \dots, β_N from an *ideal, reciprocal* equal divider/ combiner network. A good model for the phase shifters is that of a *true time delay* implementation while an ideal N -port Wilkinson divider is an accurate model for the divider/combiner network.

The system of N radiators is fully characterized by its scattering matrix $[S]$, its behavior over the frequency band of interest being assumed to be known by numerical simulations or direct measurements. As concerns the divider/combiner network, its transfer coefficients amount to $1/\sqrt{N}$ [73, p. 323]. The complete beam forming network, the phase shifters included is characterised by a diagonal matrix $[B]$ that reads

$$[B](f) = \frac{1}{\sqrt{N}} \begin{bmatrix} \exp(j\beta_1) & 0 & \dots & 0 \\ 0 & \exp(j\beta_2) & \dots & 0 \\ \vdots & \vdots & \ddots & \\ 0 & 0 & & \exp(j\beta_N) \end{bmatrix} \quad (\text{D.1})$$

with f denoting the frequency. Note that, for ensuring the progressive phase needed for steering the beam in a *linear* array, the phase shifts β_i read

$$\beta_i = k_0 d_i \sin(\vartheta_0) \text{ for } i = 1, \dots, N.$$

Here $j = \sqrt{-1}$; $k_0 = 2\pi f/c_0$ represents the wave number in free space, with c_0 being the electromagnetic wave velocity in free space, d_i denote the element

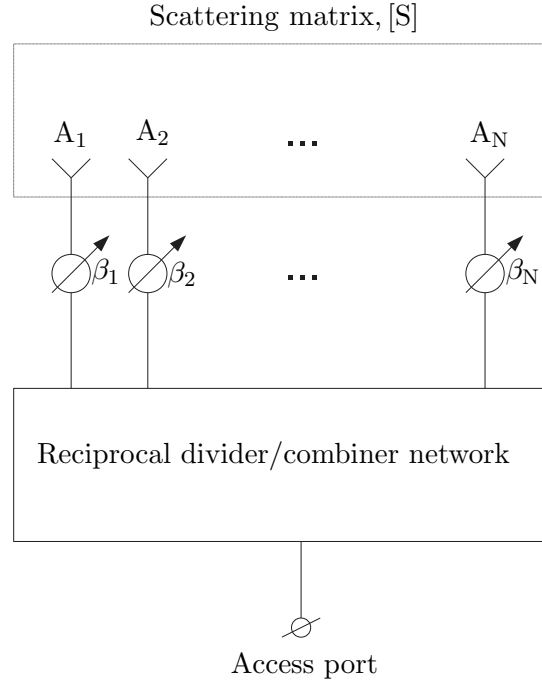


Figure D.1: Illustrative for the evaluation of the array reflection coefficient.

locations with respect to the chosen reference frame and ϑ_0 defines the main beam's steering direction. Note that Eq. (D.1) accounts for a *true time delay* implementation of the phase shifters, implying that the same signal delay will be experienced irrespective of the propagation direction (in the circuit). Obviously, the expression can be applied to other types of arrays, as well, with the phase shifts β_i being chosen in an adequate manner.

With these prerequisites, the steps for calculating the frequency and the scanning angle dependence of the reflection coefficient Γ that is experienced at the access port of the configuration in Fig. D.1 are hereafter enumerated:

As the *true time delay* implementation of the phase shifters modifies the phases of the input power, their effect on the other antenna ports can be determined as $[S][B]$. To calculate the total reflected power at each antenna port, the power coupled from other antennas as well as the reflection from the antenna itself have to be summed up, yielding the active reflection coefficient immediately at the antenna ports as

$$\Gamma_p(f) = [S][B]\mathbf{1}. \quad (\text{D.2})$$

The presence of the *true time delay* phase shifters implies that the reflected power at the antenna ports is modified further as:

$$\Gamma_{ac}(f) = [B] [S] [B] \mathbf{1}. \quad (\text{D.3})$$

Note that each row in $\Gamma_{ac}(f)$ matrix corresponds to the *active reflection coefficients* observed at the end of the delay lines.

The array reflection coefficient is calculated assuming the power is combined through an *ideal equal power combiner* at the end of the delay lines. Upon denoting as $\mathbf{1}$ the $N \times 1$ vector of ones, the array reflection coefficient follows as

$$\Gamma(f) = \mathbf{1} \cdot ([B] [S] [B] \mathbf{1}). \quad (\text{D.4})$$

Note that $|\Gamma|$ represents the array return loss as defined in Section 5.1.2.

This expression was implemented in a MATLAB code that was used for post-processing the simulated and/or measured scattering matrices, the result of which is the frequency and the scanning angle dependence of the input reflection coefficients discussed throughout the thesis.

Appendix E

Coplanar waveguide structures

A coplanar waveguide (CPW) fabricated on a dielectric substrate was firstly demonstrated by Cheng P. Wen in 1969 [101]. A conventional CPW on a dielectric substrate consists of a center strip conductor with semi-infinite ground planes on each side. The thickness of the dielectric substrate should be thick enough so that electromagnetic fields die out before they get out of the substrate. This structure supports even or odd quasi-TEM modes of propagation, depending on whether the E fields in the two slots are in the opposite direction, or the same direction. In the following sections two kinds of CPWs are going to be investigated.

E.1 Conventional coplanar waveguides

In this section, two important parameters of coplanar waveguides, namely; effective dielectric constant, ϵ_{eff} , and the characteristic impedance Z_0 for finite substrate thicknesses are presented. Conformal mapping techniques which assume a quasi-static TEM mode of propagation along the line are used to obtain ϵ_{eff} and Z_0 of the coplanar wave guides [34]. The cross-section of the coplanar waveguide (CPW) with top and bottom metal cover can be seen in Fig. E.1.

Total capacitance of the structure depicted in Fig. E.1 is required to be able to calculate ϵ_{eff} and can be calculated as follows:

$$C_{\text{CPW}} = C_1 + C_2 + C_{\text{air}} \quad (\text{E.1})$$

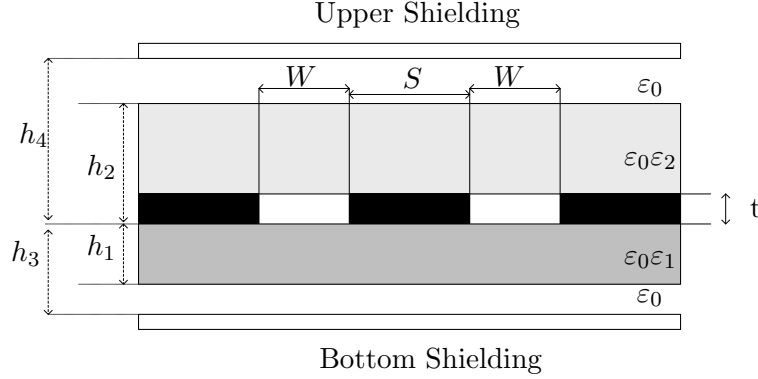


Figure E.1: Front view of a CPW, sandwiched between two dielectric substrates, with top and bottom shielding

where:

- C_{CPW} is the total capacitance of the CPW;
- C_1 and C_2 are the partial capacitance of CPW with only the lower and upper dielectric layers respectively;
- C_{air} is the partial capacitance of the CPW in the absence of the two dielectric layers.

In Eqs. (E.1), C_1 , C_2 and C_{air} can be defined as follows [34]:

$$C_1 = 2\epsilon_0(\epsilon_{r1} - 1) \frac{K(k_1)}{K(k'_1)} \quad (\text{E.2})$$

where

$$K(k) = \frac{\pi}{2} \sum_{n=0}^{\infty} \left[\frac{(2n-1)!}{(2n)!} \right]^2 k^{2n}, \quad (\text{E.3})$$

$$k_1 = \frac{\sinh(\pi S/4h_1)}{\sinh([\pi(2W+S)]/4h_1)}, \quad (\text{E.4})$$

$$k'_1 = \sqrt{1 - k_1^2}. \quad (\text{E.5})$$

$$C_2 = 2\epsilon_0(\epsilon_{r2} - 1) \frac{K(k_2)}{K(k'_2)}, \quad (\text{E.6})$$

where

$$k_2 = \frac{\sinh(\pi S/4h_2)}{\sinh([\pi(2W + S)]/4h_2)}, \quad (\text{E.7})$$

$$k'_2 = \sqrt{1 - k_2^2}. \quad (\text{E.8})$$

and

$$C_{air} = 2\epsilon_0 \frac{K(k_3)}{K(k'_3)} + 2\epsilon_0 \frac{K(k_4)}{K(k'_4)}, \quad (\text{E.9})$$

where

$$\begin{aligned} k_3 &= \frac{\tanh(\pi S/4h_3)}{\tanh([\pi(2W + S)]/4h_3)} \\ k_4 &= \frac{\tanh(\pi S/4h_4)}{\tanh([\pi(2W + S)]/4h_4)} \\ k'_3 &= \sqrt{1 - k_3^2} \\ k'_4 &= \sqrt{1 - k_4^2}. \end{aligned} \quad (\text{E.10})$$

For the CPW given in Fig. E.1, the effective dielectric constant ϵ_{eff} and the characteristic impedance Z_0 can be calculated from

$$\epsilon_{\text{eff}} = \frac{C_{\text{CPW}}}{C_{\text{air}}} \quad (\text{E.11})$$

and

$$Z_0 = \frac{\sqrt{\epsilon_{\text{eff}}}}{C_{\text{CPW}}c} = \frac{1}{cC_{\text{air}}\sqrt{\epsilon_{\text{eff}}}}, \quad (\text{E.12})$$

together with Eqs. (E.1), (E.2), (E.6) and (E.9) [34]. In Eq. (E.11) and Eq. (E.12) c is the electromagnetic wave velocity in free space. Equation (E.12) tells that when the effective dielectric constant increases the characteristic impedance Z_0 decreases.

E.2 Coplanar waveguides on a finite thickness dielectric substrate

In this thesis, coplanar waveguides on a dielectric substrate of finite thickness are used as feeding structures. Thus, ϵ_{eff} and Z_0 for this structure are important here. The cross-section of this CPW can be seen in Fig. E.2. Comparing Fig. E.1 and Fig. E.2, the following assumptions are noted with respect to the CPW on finite thickness dielectric substrate:

$$h_3 = h_4 = \infty;$$

$$\epsilon_{r2} = 1.$$

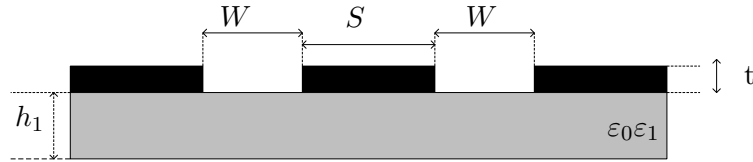


Figure E.2: Front view of a CPW on a finite thickness dielectric substrate

Under these assumptions, C_2 turns out to be 0, while k_3, k_4, k_0 become:

$$k_3 = k_4 = k_0 = \frac{S}{S + 2W}. \quad (\text{E.13})$$

Substituting k_3 and k_4 in Eq. (E.9), C_{air} is found as:

$$C_{\text{air}} = 4\epsilon_0 \frac{K(k_0)}{K(k'_0)}. \quad (\text{E.14})$$

Substituting Eq (E.2) and Eq (E.14) in Eq (E.1) gives:

$$C_{\text{CPW}} = C_1 + C_{\text{air}} = 2\epsilon_0(\epsilon_{r1} - 1) \frac{K(k_1)}{K(k'_1)} + 4\epsilon_0 \frac{K(k_0)}{K(k'_0)}. \quad (\text{E.15})$$

Using Eqs (E.11), (E.14) and (E.15), ϵ_{eff} of a CPW on a finite thickness dielectric substrate can be calculated through the following formula:

$$\epsilon_{\text{eff}} = \frac{C_{\text{CPW}}}{C_{\text{air}}} = 1 + \frac{(\epsilon_{r1} - 1) K(k_1)}{2} \frac{K(k_0)}{K(k'_1)} + \frac{K(k_0)}{K(k'_0)}. \quad (\text{E.16})$$

Finally, Z_0 of a CPW on a finite thickness dielectric substrate can be obtained using Eqs (E.12), (E.14) and (E.16)

$$Z_0 = \frac{\sqrt{\epsilon_{\text{eff}}}}{C_{\text{CPWC}}} = \frac{1}{cC_{\text{air}}\sqrt{\epsilon_{\text{eff}}}} = \frac{30\pi}{\sqrt{\epsilon_{\text{eff}}}} \frac{K(k'_0)}{K(k_0)}, \quad (\text{E.17})$$

From Eq (E.17), for a certain substrate thickness, it can be observed that the characteristic impedance decreases as the ratio $S/(S+2W)$ is increased [76]. Equations (E.16) and (E.17) provide the justification for using the CPW for feeding purposes.

Firstly, the characteristic impedance Z_0 of the line is one of the key points in ultra wide band matching. It is possible to achieve very wide bandwidth antenna elements with a CPW type of feeding as Z_0 depends on the dielectric constant of the substrate, the geometric ratio of the center strip line and the gaps which are located between the centre strip and the semi-infinite ground planes on each side.

Secondly, the effective dielectric constant, ϵ_{eff} also depends on the geometrical properties of the CPW and the dielectric constant of the substrate. Practical investigations [48] proved that the ϵ_{eff} is constant up to approximately 25 GHz and, after that, it changes linearly. In conclusion, Z_0 is independent on frequency up to high frequencies in CPW structures.

CPW's are easy to be produced as they require photo-etching on one side, only, this making them low-cost. They have low loss at low frequencies and the loss changes linearly with respect to frequency. Conversely, microstrip lines have dispersive characteristics. CPW's which have low radiation and conduction losses and less spurious radiation can be easily integrated with both microwave integrated circuits and monolithic microwave integrated circuits. Additionally, CPW's can also be employed in combination with surface mount devices and eliminate the need of the costly "Through-hole" technology.

At last, in terms of circuit isolation, a great isolation can be achieved using CPW because there are always RF grounds between the traces. For all these reasons, CPW type of feeding will be used in the design of the antennas within the scope of this dissertation.

Bibliography

- [1] “Advance Design System (ADS),” U.S.A., 2009.
- [2] A. Akdagli, C. Ozdemir, S. Yamacli *A Review of Recent Patents on Ultra Wide Band (UWB) Antennas*, Bentham Science Publishers Ltd, 2008.
- [3] O. E. Allen, “Baseband-pulse-antenna techniques,” *IEEE Antennas and Propag. Magazine*, vol. 36, pp. 20–30, 1994.
- [4] O. E. Allen, D. A. Hill, A. R. Ondrejka, “Time-domain antenna characterizations,” *IEEE Trans. on Electromagnetic Compatibility*, vol. 35, pp. 339–346, 1993.
- [5] Antenna Standards Committee of IEEE Antennas and Propagation Society, “IEEE Standard Definitions of Terms for Antennas,” New York: The Institute of Electrical and Electronics Engineers, Inc., 1983.
- [6] C. A. Balanis, *Antenna Theory: Analysis and Design*, 2nd ed., New York: John Wiley & Sons Inc., 1997.
- [7] A. K. Bhattacharyya, *Phased Array Antennas*, New York: John Wiley & Sons Inc., 2006.
- [8] R. F. J. Broas, D. F. Sievenpiper, E. Yablonovitch, “A high-impedance ground plane applied to a cellphone handset geometry,” *IEEE Trans. Microw. Theory Tech.*, vol.49, pp. 1262–1265, 2001.
- [9] C. Bruns, P. Leuchtman, R. Vahldieck, “Analysis and simulation of a 1-18-GHz broadband double-ridged horn Antenna,” *IEEE Trans. Electromagn. Compat.*, vol. 45, pp. 55–60, issue 1, 2003.
- [10] C. G. Buxton, *Design of a Broadband Array Using the Foursquare Radiating Element*, PhD Dissertation submitted to the Faculty of the Virginia Polytechnic Institute and State University, Blacksburg, Virginia, 2001.

- [11] F. M. Caimi (2002, July) *Theoretical size constraints for antennas based on quality factor Q* , Project document in IEEE P802.15 Working Group for Wireless Personal Area Networks, Melbourne. [Online]. Available: http://www.skycross.com/Technology/Whitepapers/UWB_Size_Constraints.pdf
- [12] E. D. Caswell, *Design and Analysis of Star Spiral with Application to Wideband Arrays with Variable Element Sizes*, PhD Dissertation submitted to the Faculty of the Virginia Polytechnic Institute and State University, Blacksburg, Virginia, 2001.
- [13] Z. N. Chen, "UWB Antennas: From Hype, Promise to Reality," *IEEE Antennas and Propag. Conference in Loughborough*, pp. 19–22, 2007.
- [14] X. Chen, J. Liang, P. Li, L. Guo, C. Chiau, C. G. Parini "Planar UWB monopole antennas" *Proc. of Asia-Pacific Microw. Conference*, Vol.1, 2005.
- [15] Z. H. Chen, G. D. Liu, Q. X. Chu, "A new method for analyzing large size parabolic cylindrical reflector antenna," *IEEE Antennas and Propag. Society International Symposium*, pp. 4421–4424, 2006.
- [16] Z. H. Chen, G. D. Liu, Q. X. Chu, "Reconfigurable printed cactus antenna," *IEEE Antennas and Propag. Society International Symposium*, pp. 201–204, 2006.
- [17] B. R. S. Cheo, V. H. Rumsey, W. J. Welch, "A solution to Frequency-Independent Antenna Problem," *IRE Transactions on Antennas and Propag.*, pp. 527–534, 1961.
- [18] J. -Y. Chiou, J. -Y. Sze, K. -L. Wong, "A Broad-band CPW-Fed Strip-Loaded Square Slot Antenna," *IEEE Trans. on Antenna and Propag.*, vol. 51, pp. 719–721, 2003.
- [19] L. J. Chu, "Physical limitations of omni-directional antennas," *Journal of Applied Physics*, vol. 19, pp. 1163–1175, 1948.
- [20] L.-W. Chua, "A new UWB antenna with excellent time domain characteristics," *European Microwave Conference on Wireless Technologies*, pp. 531–534, 2005.
- [21] S. Clavijo, R. E. Diaz, W. E. McKinzie, "Design methodology for Sievenpiper high-impedance surfaces: an artificial magnetic conductor for positive gain electrically small antennas," *IEEE Trans. on Antenna and Propag.*, vol. 51, pp. 2678–2690, 2003.

- [22] R. E. Collin, S. Rothschild, "Evaluation of antenna Q," *IEEE Trans. on Antenna and Propag.*, vol. 12, pp. 23–27, 1964.
- [23] C. I. Coman, *Shared Aperture Array Antennas Composed of Differently Sized Elements Arranged in Sparse Sub-arrays*, PhD Dissertation submitted to Delft University of Technology, Delft, 2006.
- [24] C. I. Coman, I. E. Lager, L. P. Ligthart, "The design of shared aperture antennas consisting of differently sized elements," IRCTR, Delft, Scientific Rep., IRCTR-S-001-05, 2005.
- [25] Y. Coulibaly, T. A. Denidni, L. Talbi, A. R. Sebak, "A new single layer broadband CPW fed-printed monopole antenna for wireless applications," *Canadian Conference on Elect. and Comput. Eng.*, vol. 3, pp. 1541–1544, 2004.
- [26] "CST Microwave Studio," Darmstadt, Germany, 2006.
- [27] T. A. Denidni, M. A. Habib "Broadband printed CPW-fed circular slot antenna," *IEEE Electronics Letters*, vol.42, no.3, pp. 135–136, 2006.
- [28] D. Z. Djurdjevic, B. D. Popovic, "Entire-domain analysis of thin-wire antennas in layered media," in *Proc. IEE Microw., Antennas and Propag.*, vol. 143, pp. 317–322, 1996.
- [29] R. S. Elliot, *Antenna Theory and Design*, London: Prentice-Hall Inc., 1981.
- [30] R. L. Fante, "Quality factor of general ideal antennas," *IEEE Trans. on Antenna and Propag.*, vol. 17, pp. 151–155, 1969.
- [31] Federal Communication Commission, "FCC 02-48 – First Report and Order: Revision of Part 15 of the Commission's Rules Regarding Ultra-Wideband Transmission Systems," Washington, DC, released April 22, 2002.
- [32] A. P. Feresidis, G. Goussetis, W. Shenhong, J. C. Vardaxoglou, "Artificial Magnetic conductor surfaces and their application to low-profile high-gain planar antennas," *IEEE Trans. on Antenna and Propag.*, vol. 53, pp. 209–215, 2005.
- [33] R. Garg, P. Bhartia, I. Bahl, A. Ittipiboon, *Microstrip Antenna Design Handbook*, Norwood: John Wiley & Sons Inc., 2001.
- [34] S. Gevorgian, L. J. P. Linner, E. L. Kollberg, "CAD models for shielded multilayered CPW," *IEEE Trans. Microw. Theory Tech.*, vol.43, pp. 772–779, 1995.

- [35] M. C. Greenberg, K. L. Virga, C. L. Hammond, "Performance characteristics of the dual exponentially tapered slot antenna (DE TSA) for wireless communications applications," *IEEE Transactions on Vehicular Technology*, pp. 305–312, 2003.
- [36] L. Guo, J. Liang, X. Chen, C. G. Parini, J. Yu "Performances of ultra-wideband disc monopoles in time domain," *IET Microwaves, Antennas and Propag.*, vol.1 pp. 955–959, 2007.
- [37] M. A. Habib, M. Nedil, T. A. Denidni, "New Ultra-Wideband Patch Antenna Using Coplanar Technology with Curved Ground," *Second International Conference on Wireless in Underground and Confined Areas*, 2008.
- [38] R. C. Hansen, *Phased Array Antennas*, 2nd ed., New York: Artech House, Inc., 1998.
- [39] R. F. Harrington, "Effects of Antenna Size on Gain, Bandwidth, and Efficiency," *J.Res. Nat. Bureau of Standards*, vol. 64-D, pp. 1–12, 1960.
- [40] T. Q. Ho, "An ultra-wideband reflector antenna," *IEEE Antennas and Propag. Society International Symposium*, vol. 1, pp. 470–473, 1993.
- [41] A. Z. Hood, T. Karacolak, E. Topsakal, "A Small Antipodal Vivaldi Antenna for Ultrawide-Band Applications," *IEEE Antennas and Propag. Letters*, vol.7 pp. 656–660, 2008.
- [42] Y.-T. Hsiao, Y.-Y. Lin, Y.-C. Lu, H.-T. Chou "Applications of Time-Gating Method to Improve the Measurement Accuracy of Antenna Radiation inside an Anechoic Chamber," *IEEE Antennas and Propag. Society International Symposium*, vol.3, pp. 794–797, 2003.
- [43] C. -Y. Huang, W. -C. Hsia "Planar elliptical antenna for ultra-wideband communications," *IEEE Electronics Letters*, vol. 41, pp. 296–297, 2005.
- [44] IEEE Std 1672-2006, "IEEE Standard for Ultrawideband Radar Definitions," IEEE-SA Standards Board, November 10, 2008.
- [45] A. Ishimaru, "Theory of unequally-spaced arrays," *IRE Trans. on Antenna and Propag.*, vol.10 pp. 691–702, 1962.
- [46] H. M. Jafari, M. J. Deen, S. Hranilovic, N. K. Nikolova, "A study of ultrawideband antennas for near-field imaging," *IEEE Trans. on Antenna and Propag.*, vol. 55, pp. 1184–1188, 2007.

- [47] J. -Y. Jan, J. -C. Kao, Y. -T. Cheng, W. -S. Chen, H. -Ming Chen, "CPW-fed wideband printed planar monopole antenna for ultra-wideband operation," *IEEE Antennas and Propag. Society International Symposium*, pp. 1697–1700, 2006.
- [48] K. Jayaraj, T.E. Noll, D. Singh, "RF characterization of a low cost multichip packaging technology for monolithic and millimeter wave integrated circuits," in *Proc. Signals, Systems, and Electronics*, pp. 443–446, 1995.
- [49] S. Kashyap, S.R. Mishra, "Improvement in antenna factor measurements using time-domain gating," *IEEE International Symposium on Electromagnetic Compatibility*, pp.82–86, 1988.
- [50] D.F. Kelley, W.L. Stutzman, "Array antenna pattern modeling methods that include mutual coupling effects," *IEEE Transactions on Antennas and Propag.*, vol 41, pp. 1625–1632, 1993.
- [51] H. Kim, D. Park, Y. Joo, "All-digital low-power CMOS pulse generator for UWB system," *IEEE Electronics Letters*, vol.40, no.24, pp. 1534–1535, 2004.
- [52] D.D. King, R. F. Packard, R. K. Thomas, "Unequally-Spaced, Broad-Band Antenna Arrays," *IEEE Trans. on Antenna and Propag.*, vol.8 pp. 380–384, 1960.
- [53] M. Klemmn, G. Troster, "Characterization of small planar antennas for UWB mobile terminals," *Wireless. Commun. Mobile Comput.*, pp. 525–536, 2005.
- [54] K. Kota, L. Shafai, "Parametric study of Vivaldi antenna," *IEEE International Symposium on Antenna Technology and Applied Electromagnetics and the Canadian Radio Science Meeting*, pp. 1–4, 2009.
- [55] J. D. Kraus, *Antennas for All Application*, 2nd ed., New York: McGraw-Hill Companies, Inc., 2002.
- [56] G. Kumar, K.P. Ray, *Broadband Microstrip Antennas*, Norwood: Artech House, Inc., 2003.
- [57] R. J. Mailloux, *Phased Array Antenna Handbook*, Norwood, MA, Artech House, Inc., 2005.
- [58] I. E. Lager, M.Simeoni, "Cost-effective array antennas for narrow-beam, wide-angle scanning applications," 36th *European Microwave Conference*, pp. 1790–1793, 2006.

- [59] I. E. Lager, M. Simeoni, "Experimental investigation of the mutual coupling reduction through cavity enclosure of patch antennas," *Proc. of 1st European Conference on Antennas and Propag.*, pp. 1–5, 2006.
- [60] Y. -C. Lee, S. -C. Lin, J. -S. Sun, "CPW-Fed UWB Slot Antenna" *Proc. of Asia-Pacific Microw. Conference*, pp. 1636–1639, 2006.
- [61] P. Li, J. Liang, X. Chen, "Study of Printed Elliptical/Circular Slot Antennas for Ultrawideband Applications," *IEEE Trans. on Antenna and Propag.*, vol. 54, pp. 1670–1675, 2006.
- [62] J. Liang, C. C. Chiau, X. Chen, C. G. Parini, "Study of Printed Circular Disc Monopole Antennas for UWB Systems," *IEEE Trans. on Antenna and Propag.*, vol. 53, pp. 3500–3504, 2005.
- [63] J. Liang, C. C. Chiau, X. Chen, C. G. Parini, "Study of CPW-fed circular disc monopole antenna for ultra wideband applications," *IEE Proc.-Microw. Antennas Propag.*, vol. 152, pp. 520–526, 2005.
- [64] J. Liang, C. C. Chiau, X. Chen, C. G. Parini, "CPW-fed circular ring monopole antenna," *IEEE Antennas and Propag. Society International Symposium*, vol. 2A, pp. 500–503, 2005.
- [65] J. Liang, L. Guo, C. C. Chiau, X. Chen, "CPW-fed circular disc monopole antenna for UWB applications," *IEEE International Workshop on Antenna Tech.: Small Antennas and Novel Metamaterials*, pp. 505–508, 2005.
- [66] C. -C. Lin, Y. -C. Kan, L. -C. Kuo, "A planar triangular monopole antenna for UWB communication," *IEEE Microw. Wireless Compon. Lett.*, vol. 15, pp. 624–626, 2005.
- [67] R. M. Mateos, C. Craeye, "Wideband low-profile antennas," *final report- ESA/ESTEC Contract no. 17576/03/NL/LvH*, 2005.
- [68] R. M. Mateos, C. Craeye, G. Toso, "High-Gain Wideband Low-Profile Antenna," *Microwave and Optical Technology Letters*, pp. 2615–2619, 2006.
- [69] A. Mehdipour, A. Parsa, A. R. Sebak, C. W. Trueman, "Planar bell-shaped antenna fed by a CPW for UWB applications," *IEEE Antennas and Propag. Society International Symposium*, pp. 1–4, 2008.
- [70] Nasimuddin, K. P. Esselle, A. K. Verma, "Wideband circularly polarized stacked microstrip antennas," *IEEE Antennas Wireless Propag. Lett.*, vol. 6, pp. 21–24, 2007.

- [71] F. A. Nekoogar, *Ultra-Wideband Communications*, New York: Prentice Hall, 2005.
- [72] M. A. Peyrot-Solis, G. M. Galvan-Tejada, H. Jardon-Aguilar, "State of the Art in Ultra-Wideband Antennas," *2nd International Conference on Electrical and Electronics Engineering (ICEEE)*, Mexico, pp. 101–105, 2005.
- [73] D. M. Pozar, *Microwave Engineering*, third edition, John Wiley & Sons, Inc., Hoboken, NJ, 2005.
- [74] J. G. Proakis, *Digital Communications*, New York: John Wiley & Sons Inc., 2004.
- [75] X. Qing, Z. N. Chen "Transfer functions measurement for UWB antenna," *IEEE Antennas and Propag. Society International Symposium*, pp. 2532–2535, 2004.
- [76] A. K. Rastogi, N. J. McEwan, I. U. Khairuddin, A. Z. Jakal, "Effect of substrate thickness and metalization thickness on dispersion characteristics of CPW," *International Journal of Infrared and Millimeter Waves*, pp. 1393–1406, 1995.
- [77] W. V. T. Rusch , "The current state of the reflector antenna are-entering the 1990s," in *Proc. of IEEE*, vol.80, pp. 113–126, 1992.
- [78] W. Sandrin, C. Glatt, D. Hauge, "Design of arrays with unequal spacing and partially uniform amplitude taper," *IEEE Trans. on Antenna and Propag.*, vol.17 pp. 642–644, 1969.
- [79] H. G. Schantz, "UWB Magnetic Antennas," *IEEE Antennas and Propag. Society International Symposium*, vol. 3, pp. 604–607, 2003.
- [80] D. Sievenpiper, H. P. Hsu, J. Schaffner, G. Tangonan, R. Garcia, S. Oniveros, "Low-profile, four-sector diversity antenna on high-impedance ground plane," *IEEE Electron. Lett.*, vol.36, pp. 1343–1345, 2000.
- [81] D. Sievenpiper, L. Zhang, R. Broas, N. G. Alexopolous, E. Yablonovitch, "High-impedance electromagnetic surfaces with a forbidden frequency band," *IEEE Trans. Microwave Theory Tech.*, vol. 47, pp. 2059-2074, 1999.
- [82] D. Sievenpiper, L. Zhang, E. Yablonovitch, "High-impedance electromagnetic ground planes," *IEEE Trans. Microw. Theory Tech.*, vol.4, pp. 1529–1532, 1999.

- [83] M. Singh, S.K. Shiban, A. Basu, "Coplanar Waveguide Fed Ultra Wide Band Monopole Antenna," *IEEE RF and Microwave Conference*, pp. 44–47, 2006.
- [84] K. Siwiak, D. McKeown *Ultra-Wideband Radio Technology*, New York: John Wiley & Sons Inc., 2004.
- [85] J. W. Stewart, W. D. Wood, "A study of a bowtie antenna integrated into a high-impedance ground plane," *IEEE Antennas and Propag. Society International Symposium*, vol. 4, pp. 855–858, 2003.
- [86] S. -Y. Suh, *A Comprehensive Investigation of New Planar Wideband Antennas*, PhD Dissertation submitted to the Faculty of the Virginia Polytechnic Institute and State University, Blacksburg, Virginia, 2002.
- [87] I. -T. Tang, D. -B. Lin, G. -H. Liou, J. -H. Horng, C. -M Lin "A Compact Slot UWB Antenna with CPW-fed," *IEEE Antennas and Propag. Society International Symposium*, pp. 5143–5146, 2007.
- [88] F. M. Tanyer-Tigrek, A. Hizal, I. E. Lager, L. P. Ligthart, "On the Operating Principles of UWB, CPW-fed Printed Antennas," accepted for publication in *IEEE Antennas and Propagation Magazine* - due issue in June 2010.
- [89] F. M. Tanyer-Tigrek, I. E. Lager, L. P. Ligthart, "CPW-fed Printed Loop Antenna for Ultra Wide-band Applications and its Linear Array Performance," re-submitted to *Antennas and Propag. Magazine*, 2009; Also issued as Scientific Report IRCTR-S-004-09.
- [90] F. M. Tanyer-Tigrek, I. E. Lager, L. P. Ligthart, "Experimental Validation of a Linear Array Consisting of CPW fed, UWB, Printed, Loop Antennas," accepted for publication in *Transactions on Antennas and Propag.*, 2009.
- [91] F. M. Tanyer-Tigrek, R. M. Mateos, C. Craeye, I. E. Lager, "Design of an AMC plane for a unidirectional, low-profile tulip-loop antenna," *Proc. of 3rd European Conference on Antennas and Propag.*, pp. 3139–3142, 2009.
- [92] F. M. Tanyer-Tigrek, D. P. Tran, I. E. Lager, L. P. Ligthart, "CPW-fed, Quasi-magnetic, Printed Antenna for Ultra Wide-band Applications," *IEEE Antennas and Propag. Magazine*, vol. 2, pp 61–70, 2009.
- [93] F. M. Tanyer-Tigrek, D. P. Tran, I. E. Lager, L. P. Ligthart, "Over 150% Bandwidth, Quasi-Magnetic, Printed Antenna," *Proc. IEEE Antennas and Propag. Society International Symposium*, pp. 1–4, 2008.

- [94] L. Tianming, R. Yuping, N. Zhongxia “Analysis and Design of UWB Vivaldi Antenna,” *IEEE International Symposium on Microwave, Antenna, Propagation and EMC Technologies for Wireless Communications*, pp. 579–581, 2007.
- [95] W. Tong, Z.R. Hu, “A CWP fed circular monopole antenna for ultra wideband wireless communications,” *IEEE Antennas and Propag. Society International Symposium*, vol. 3A, pp. 528–531, 2005.
- [96] H. Unz, “Linear Arrays with arbitrarily distributed elements,” *IRE Trans. on Antenna and Propag.*, vol.8 pp. 222–223, 1960.
- [97] J.R. Verbiest, G.A.E. Vandenbosch, “Small-size planar triangular monopole antenna for UWB WBAN applications,” *Electronics Letters*, 2008, pp. 177–179.
- [98] J.J.H. Wang, “The Physical Foundation, Development History, and Ultra-wideband Performance of SMM (Spiral-Mode Microstrip) Antennas” *Proc. IEEE Antennas and Propag. Society International Symposium*, pp. 586–589, 2005.
- [99] S. Wang, X.D. Chen, C.G. Parini, “Analysis of Ultra Wideband Antipodal Vivaldi Antenna Design,” *IEEE Antennas and Propag. Conference in Loughborough*, pp. 129–132, 2007.
- [100] D.X. Wang, K.N. Yung, R.S. Chen, “Efficient analysis of wire antennas and scatterers with arbitrary shape,” *IEEE Antennas Wireless Propag. Lett.*, vol. 2, pp. 107–110, 2003.
- [101] C.P. Wen, “Coplanar waveguide: a surface strip transmission line suitable for nonreciprocal gyromagnetic device applications,” *IEEE Trans. Microw. Theory Tech.*, vol.17, pp. 1087–1090, 1969.
- [102] H.A. Wheeler, “Fundamental limitations of small antennas,” in *Proc. IRE (Institute of Radio Engineers)*, vol.69, pp. 1479–1484, 1947.
- [103] F. Yang, Y. Rahmat-Samii, “Reflection Phase Characterization of the EBG Ground Plane for Low Profile Wire Antenna Applications,” *IEEE Trans. on Antenna and Propag.*, vol. 51, pp. 2691–2703, 2003.
- [104] H.K. Yoon, W.S. Kang, Y.J. Yoon, C.-H. Lee, “A CPW-fed flexible monopole antenna for UWB systems,” *IEEE Antennas and Propag. Society International Symposium*, pp. 701–704, 2007.
- [105] Y. Zhang, J.v. Hagen, M. Younis, C. Fisher, W. Wiesbeck, “Planar Artificial Magnetic Conductors and Patch Antennas,” *IEEE Trans. on Antenna and Propag.*, vol. 51, pp. 2704–2712, 2003.

- [106] L. Zhao, C. -L. Ruan, S. W. Qu, "A Novel Broad-band Slot Antenna Fed by CPW," *IEEE Antennas and Propag. Society International Symposium*, pp. 2583–2586, 2006.

List of Abbreviations

AMC	Artificial Magnetic Conductor
CPW	Coplanar Waveguide
DS-UWB	Direct Sequence Ultra Wide Band
DUCAT	Delft Unechoic Chamber for Antenna Tests
EBG	Electronic Band Gap
FCC	Federal Communications Commission
GND	Ground
IEEE	Institute of Electrical and Electronics Engineers
IR	Impulse Radio
MB-OFDM	Multi-band Orthogonal Frequency Division Multiplexing
MTS	Multi-port test-set
PEC	Perfect Electric Conductor
PMC	Perfect Magnetic Conductor
SNR	Signal-to-Noise Ratio
TEM	Transverse Electromagnetic
UWB	Ultra Wide Band
VSWR	Voltage Standing Wave Ratio
WiSE	Wide Band Sparse Element Array Antennas

Summary

Ultra-wideband (UWB) is a radio technology that can be used at very low energy levels, for short-range high-bandwidth communications, by using a large radio spectrum. Due to its high speed rate, this technology is nowadays one of the most promising solutions for communications. Maximum data that can be transmitted per second over a communication channel can be high since the UWB signals have large bandwidth. Recently the printed antennas for UWB applications have also become a topic of sustained investigation in the fields of wireless communications and radar applications, due to such attractive features as transmitting and/or receiving electromagnetic energy in shorter duration and avoiding both frequency and space dispersion.

There are already some solutions for low profile UWB elements in the literature; however, they have some deficiencies such as they can not ensure the wide bandwidth and the small electrical size features at the same time and/or they have complex shapes so that the manufacturing process of these antennas can be difficult and costly. It is also important for the antenna elements to work well in array environments. Hereafter we can derive our prime research question: How can we design optimal UWB elements for array environments? The research question has been answered by introducing two (quasi-) magnetic types of antennas. Coplanar Waveguide (CPW) lines have been used for feeding the antennas allowing for wider impedance bandwidths. With these features the “Eared” antennas and the “Tulip” loop antennas have been investigated in detail. All calculated results were confirmed via measurements. To the author’s knowledge these antennas have the widest impedance bandwidth with the electrically smallest sizes compared to other similar types of printed and low-profile antennas described in literature. A feasibility study on adding a ground plane to be used with the elementary radiators has also been done in this dissertation. In this study the “Tulip” loop antenna has been used together with the properly designed Artificial Magnetic Conductor (AMC).

One of the goals of this research was designing UWB elements for

(linear) array environments. Thus, the linear array performances of “Eared” antenna and the “Tulip” loop antennas have been investigated. All computed results were confirmed via measurements. It has been proven that these antennas can be used in array environments. A method to predict the electrical performances of large arrays from the results of smaller arrays has been developed and the electrical performances can be well predicted without doing lengthy simulations and/or measurements. The validity of the method was confirmed via measurements.

Impulse Radio (IR) is a method of transmitting UWB signals without carrier. One goal in this research is to design antennas for IR applications. Thus, the suitability of antenna elements to Impulse Radio applications has been investigated and quite successful results have been obtained for the designed IR UWB band antennas.

With all studies conducted in this dissertation, electrically smaller, repeatable and wide bandwidth antenna elements with stable radiation patterns have been developed. This dissertation adds a successful contribution to further UWB antenna (array) developments.

Samenvatting

Ultra-wideband (UWB) is een radiotechnologie die gebruikt kan worden bij zeer lage energie niveau's voor korte afstand, hoge bandbreedte communicatie door gebruik te maken van een groot radio spectrum. Vanwege de mogelijkheid van een hoge datasnelheid is deze technologie vandaag de dag een van de meest veelbelovende oplossingen voor telecommunicatie. Het maximum aan data dat per seconde overgezonden kan worden via een communicatiekanaal kan hoog zijn omdat dergelijke UWB signalen een grote bandbreedte hebben. Onlangs zijn geprinte antennes voor UWB applicaties onderwerp geworden van aanhoudend onderzoek op het gebied van draadloze communicatie en radar applicaties, vanwege de aantrekkelijke kenmerken zoals het verzenden en/of ontvangen van electromagnetische energie in een korte periode terwijl zowel herhaling als verspreiding in de ruimte vermeden wordt.

Er bestaan al enkele oplossingen voor laag profiel (platte) UWB elementen in de literatuur; ze hebben echter enkele tekortkomingen zoals het niet kunnen waarborgen van de grote bandbreedte en tegelijkertijd de kleine elektrische afmetingen en/of ze hebben complexe vormen zodat het fabricageproces van deze antennes moeilijk is en kostbaar. Het is ook belangrijk voor de antenne elementen dat ze goed werken wanneer ze in een antenne stelsel (array) zijn opgesteld. Vervolgens ontlenen we hieraan onze eerste onderzoeksvraag. Hoe kunnen we optimale UWB elementen ontwerpen t.b.v. array configuraties. De onderzoeksvraag is beantwoord door twee (quasi-) magnetische types antennes te introduceren. Coplanar Waveguide (CPW) transmissie lijnen zijn gebruikt om de antennes te voeden en een grotere bandbreedte mogelijk te maken. Met deze kenmerken zijn de "Eared" antennes en de "Tulip" loop antennes tot in detail onderzocht. Alle berekende resultaten zijn bevestigd door metingen. Volgens de auteur hebben deze antennes de grootste bandbreedtes met de kleinste elektrische afmetingen in vergelijking tot andere vergelijkbare types geprinte en "low-profile" antennes die in de literatuur zijn beschreven.

Een haalbaarheidsstudie om een grondvlak toe te voegen aan de elementaire stralers is ook uitgevoerd in deze dissertatie. In deze studie is de “Tulip” loop antenne gebruikt tesamen met de correct ontworpen Artificial Magnetic Conductor (AMC).

Een van de doelen van dit onderzoek was het ontwerpen van UWB elementen ten behoeve van (lineaire) array configuraties. Zo zijn de lineaire array kenmerken van de “Eared” antenne en van de “Tulip” loop antennes onderzocht. Alle computer resultaten zijn bevestigd via metingen. Het bewijs is geleverd dat deze antennes gebruikt kunnen worden in array configuraties. Een methode om de elektrische resultaten van grote arrays t.o.v. de resultaten van kleinere arrays te voorspellen is ontwikkeld; de elektrische resultaten kunnen zo goed voorspeld worden zonder het doen van langdurige simulaties en/of metingen. De deugdelijkheid van de methode is door metingen bevestigd.

Impulse Radio (IR) is een methode van overdracht van UWB signalen zonder draaggolf. Een van de doelen van dit onderzoek is om antennes te ontwerpen voor IR applicaties. Er is de geschiktheid van antenne elementen voor Impulse Radio onderzocht en er zijn succesvolle resultaten verkregen voor het ontwerpen van de IR UWB antennes.

Dankzij alle studies, uitgevoerd in deze dissertatie zijn elektrisch kleinere, zich herhalende, antenne elementen met grote bandbreedte ontwikkeld en met stabiele stralingspatronen. Dit proefschrift voegt een succesvolle bijdrage toe aan verdere UWB antenne (array) ontwikkelingen.

Acknowledgments

First of all, I would like to express my gratitude to my promotor, Prof. Leonardus Ligthart for giving me the opportunity to pursue my PhD in IRCTR. He kept me on track for the entire time that I was in Delft.

Secondly, special thanks go to my daily supervisor Prof. Ioan E. Lager, who supported me during my research. He was always able to stimulate me to go one step further. He also introduced me to \LaTeX for which I am greatly indebted. Writing all the manuscripts and of course the thesis became much easier by using \LaTeX . I also thank him very much for his diligence in proof-reading this dissertation.

I also appreciate the technical and moral support of Prof. Altuncan Hızal. During my studies in Delft, I always felt that he was willing to help me even from far away. I am grateful to Prof. Hızal and Prof. Tuncay Birand for suggesting that Firat and I apply for PhD positions at TU Delft. Prof. Gönül Turhan-Sayan was also always there to share her experience with me for which I am greatly indebted.

I wish to thank Prof. Cristophe Craeye, who gave me the opportunity to perform a research on “Artificial Magnetic Conductors” in Universite Catholique de Louvain. This research resulted in Chapter 4 of this dissertation and was supported by COST (IC0603) “Antenna Systems & Sensors for Information Society Technologies”. This support is gratefully acknowledged. Apart from the productive research, I also made many good friends there.

I wish to express my gratitude to the secretariat of IRCTR, especially for the unforgettable help and caring that I received from Mia van der Voort during my most difficult times in Delft. She was also the one who helped me in the translations of “Summary” and “Propositions” to Dutch which made my life a lot easier during some of my busiest days, and for which I am grateful. I am also thankful to Marjon Verkaik for taking care of the final preparation of my PhD work.

The practical realization of this work would not have been possible

without Johan Zijderveld, Paul Hakkaart and Pascal Aubry, for their efforts I am grateful. I also thank to D. P. Tran for sharing his knowledge with me, especially in my second year.

I wish to thank Jennifer Ryan, Pedro Rivera Diaz del Castillo and Seamus for their friendship and proof-reading of some parts of my thesis. Special thanks to my friends in IRCTR, I have shared lots of things together with them and enjoyed their friendship very much. Galina Babur and Xiaohua Lian's help with the cover design of this thesis was greatly appreciated. I owe special thanks to my far-away but close friend, Özlem Eşkil, for her sincere friendship, constant support and making herself available whenever I need.

I am grateful to my family for their encouragement, endless love and understanding of the extended hours spent on this work. Especially the endless support of my brother, Dr. Ali Murat Tanyer during my PhD period was greatly appreciated. He was really a power that helped me tackle both personal and professional difficulties.

Finally, I want to thank to my husband, R. Fırat Tiğrek for being always there for me and for his constant love and support for everything in my life.

F. Müge Tanyer-Tiğrek

Delft, August 2009

About the author

F. Müge Tanyer-Tiğrek was born in Turkey, on 6 March, 1979. She received her B.Sc. and M.Sc. degrees from Middle East Technical University, Ankara in June 2002 and March 2005 respectively. From August 2002 to January 2006, she was with ASELSAN Inc., Ankara working on radar and electronic warfare systems as an RF engineer. In January 2006, she joined the International Research Centre for Telecommunications and Radar (IRCTR) at the Delft University of Technology, Delft, the Netherlands and she began working towards her Ph.D. degree there. Her current research interests include ultra wideband (UWB) low-profile radiators and their behaviors in array environments, miniaturization of antennas and antenna measurements.

Author's Publications

Refereed Journal Papers

1. F. M. Tanyer-Tigrek, I. E. Lager, L. P. Ligthart, "On the Array Performance of Printed, Ultra Wide-band "Eared" Antennas," to be submitted to *Antennas and Propag. Magazine*, 2009; Also issued as Scientific Report IRCTR-S-018-09.
2. F. M. Tanyer-Tigrek, I. E. Lager, L. P. Ligthart, "CPW-fed Printed Loop Antenna for Ultra Wide-band Applications and its Linear Array Performance," re-submitted to *Antennas and Propag. Magazine*, 2009; Also issued as Scientific Report IRCTR-S-004-09.
3. F. M. Tanyer-Tigrek, I. E. Lager, L. P. Ligthart, "Experimental Validation of a Linear Array Consisting of CPW fed, UWB, Printed, Loop Antennas," accepted for publication in *Transactions on Antennas and Propag.*, 2009.
4. F. M. Tanyer-Tigrek, A. Hizal, I. E. Lager, L. P. Ligthart, "On the Operating Principles of UWB, CPW-fed Printed Antennas," accepted for publication in *IEEE Antennas and Propagation Magazine* - due issue in June 2010.
5. F. M. Tanyer-Tigrek, D. P. Tran, I. E. Lager, L. P. Ligthart, "CPW-fed, Quasi-magnetic, Printed Antenna for Ultra Wide-band Applications," *IEEE Antennas and Propag. Magazine*, vol. 2, pp 61–70, 2009.

Refereed Conference Papers

1. F. M. Tanyer-Tigrek, I. E. Lager, L. P. Ligthart, "Experimental Validation of the Time-Domain Behavior of the UWB, "Eared" Antenna for Impulse Radio Applications," accepted for presentation during the 4th *European Conference on Antennas and Propag.*, 2009.

2. F. M. Tanyer-Tigrek, I. E. Lager, L. P. Ligthart, "Efficient and accurate investigation of linear arrays consisting of UWB radiators," 36th *European Microwave Conference*, pp. 645–648, 2009.
3. F. M. Tanyer-Tigrek, R. M. Mateos, C. Craeye, I. E. Lager, "Design of an AMC Plane for a Unidirectional, Low-profile Tulip-Loop Antenna," 3rd *European Conference on Antennas and Propag.*, pp. 3139–3142, 2009.
4. F. M. Tanyer-Tigrek, D. P. Tran, I. E. Lager, L. P. Ligthart, "Wide-band Tulip-Loop Antenna," 3rd *European Conference on Antennas and Propag.*, pp. 1446–1449, 2009.
5. D. P. Tran, F. M. Tanyer-Tigrek, I. E. Lager, L. P. Ligthart, "A Novel Unidirectional Radiator with Superb UWB Characteristics for X-band Phased Array Applications," 3rd *European Conference on Antennas and Propag.*, pp. 1617–1621, 2009.
6. F. M. Tanyer-Tigrek, D. P. Tran, I. E. Lager, L. P. Ligthart, "Over 150% Bandwidth, Quasi-magnetic, printed antenna," *Antennas and Prop. Society International Symposium (AP-S)*, 2008.
7. D. P. Tran, F. M. Tanyer-Tigrek, I. E. Lager, L. P. Ligthart, "A Novel Uni-Directional, off-Axis CPW-Fed, Matched by Unbalanced Fork-Stub, UWB Ring Slot Antenna Printed on Single Layer PCB with Back Plane," *Antennas and Prop. Society International Symposium (AP-S)*, 2008.
8. D. P. Tran, F. M. Tanyer-Tigrek, A. Vorobyov, I. E. Lager, L. P. Ligthart, "A Novel CPW-fed Optimized UWB Printed Antenna," 10th *European Conference on Wireless Technology - ECWT*, pp. 40–43, 2007.

M.Sc. Thesis

F. M. Tanyer-Tigrek, "Design of Log-Periodic Dipole array feed and wide band reflector antenna system," *Masters Thesis*, Middle East Technical University, Ankara, March, 2005.

